THE UNIVERSITY *of* EDINBURGH

Granular Changes in Brain Networks: Multiplex Nodal Modularity for Alzheimer's Disease Characterization and Simulation

Avalon Campbell-Cousins

Doctor of Engineering

THE UNIVERSITY OF EDINBURGH

2025

Abstract

Neurodegenerative diseases, most prevalently Alzheimer's disease (AD), cause progressive cognitive and intellectual decline, placing immense emotional and financial strain on families and government services. Primary methods in the diagnosis of AD typically focus on cognitive questionnaires, screening tests, medical history, and neuropsychological examinations. However, early detection of AD remains difficult, with gaps in our understanding of how early stages contribute to the disease's progression. To this end, a range of neuroimaging methods both structural, such as structural magnetic resonance imaging (sMRI) and diffusion tensor imaging (DTI), and functional, including functional magnetic resonance imaging (fMRI) and electroencephalography (EEG), have been used to study changes in the brain across the AD continuum and uncover biomarkers of disease progression.

These advancements in brain imaging have facilitated a network-based model of the brain where brain regions are linked according to anatomical connections or functional associations. This model captures the inter-dependencies and interactions between brain regions that drive complex cognitive processes. These brain regional interactions can be modelled as single-layer networks or as a collection of brain networks (multiplex networks) which evolve across time or other indexed data. Brain networks organize and reorganize themselves in a multitude of ways such as in response to task stimuli or as a result of damage due to disease. Organizational topological structures, captured as modules (groups) composed of a collection of brain regions, can be dynamically explored and are of particular interest for diseases such as AD where progression causes abnormal altering of these modular structures. However, modularity in its current state is limited in its use as a metric describing the total extent to which the brain is segregated into distinct modules. It does not currently describe the individual contributions of individual brain regions to overall brain modularity.

To tackle this, we introduce nodal modularity (nQ) as a novel graph measure that extends classical modularity to individual nodes for both single-layer and multiplex networks. We assess the novelty of nQ against other common single-layer and multiplex measures of node influence. Additionally, we explore the hypothesis that nQ would yield novel insights into the progression of amnestic Mild Cognitive Impairment (aMCI, a prodromal stage of AD) given that global changes in modularity have been previously observed along this continuum. This is investigated in single and multiplex networks of a visual short-term memory binding task (VSTMBT – a cognitive biomarker of AD) constructed from DTI and task-fMRI data. The results indicated that nQ could effectively characterize the transition point from MCI to AD

(MCI converters, or MCIc). Additionally, results corroborated previously understood progression pathways of AD including the identification of key subnetworks affected by the disease (visual, limbic and paralimbic), along with agreement with amyloid-β and tau deposition for subjects with poor visual short-term memory binding.

Following the introduction of nQ, we expand the study to larger multiplex networks with a focus on covering typical constructions in neuroimaging research. We verify that nQ is distinct from other multiplex measures of node influence across a number of multiplex surrogate networks. We find that, as network size and the number of network layers increase, that nQ captures unique information distinct from other multiplex network metrics, reflecting nQ's ability to capture more wide-reaching changes in network topology than the typical local measures used (multiplex clustering coefficient, multiplex PageRank, and degree). Additionally, we explore specific cases where nQ does not provide a significant advantage as a network measure over the state of the art, largely driven by cases of highly modular networks with high within module connectivity and low between module connectivity. Furthermore, we propose collapsibility as a novel method of simplifying analyses of nQ in larger networks, explored in tandem with multiplex flexibility. We apply these to multiplex frequency-based networks of source-space EEG data during the VSTMBT, and analyse changes along the healthy to MCI progression of AD. We found changes in nQ and collapsibility which agree with known changes in grey matter and with abnormal functional connectivity around the thalamus as a result of MCI and AD.

Lastly, we explore how nQ can facilitate the simulation of AD progression by developing novel targeted attack models. Specifically, we investigate the current state of the art in targeted attacks in our task-fMRI data in the modelling of healthy to MCIc progression. We find that prior research in targeted attacks that focus on node degree were not sufficient in describing this progression from healthy to MCIc for task-fMRI. To tackle this, we propose a brain lobe-based targeting system informed by prior findings on nQ progression and established hypotheses on network damage in AD. Additionally, we confirm that improvements in simulated progression using the lobe-based method are not explainable solely by preferential attacks on long distance connections, achieved through the introduction of a targeted attack model based on Euclidean distance. We then leverage nQ to improve the lobe-based model and show that both lobe-based and nQ-based targeted attack models improve on the state of the art.

In sum, this thesis highlights the importance of considering granular changes in network topology to capture complexities in brain structure and function. Specifically, through the establishment of a novel metric of granular community structure, nQ, providing methodological considerations for the use of this measure in larger networks, and in exploring the simulation of granular changes due to AD through novel targeted attack models. Given modularity's

widespread use as a global measure, nQ represents a significant advancement, providing a granular measure of network organization applicable across disciplines. In regard to AD, this thesis motivates additional study of nQ in characterizing the stages of MCI and particularly in disentangling MCI from MCI converters during the VSTMBT.

Lay Summary

Alzheimer's disease (AD) is often preceded by amnestic (memory-related) mild cognitive impairment (aMCI) where one's memory is worse than it would be due to natural ageing. Of those with aMCI, some go on to progress to Alzheimer's disease (MCI converters) while others do not. It is important to understand the biomarkers (measurable patterns that indicate disease) of AD so that early detection becomes possible. Early detection of Alzheimer's disease is crucial, as treatments are more effective in the initial stages where less damage to the brain has been done. One proposed biomarker of AD is the visual short-term memory binding task (VSTMBT) which involves remembering coloured shapes. This task is particularly difficult for people with aMCI and AD. The VSTMBT is often completed while the brain is being recorded, such as with electroencephalography (EEG) which records the electrical signals produced by the brain, or with functional magnetic resonance imaging (fMRI) which records the blood movement in the brain (both EEG and fMRI are ways of measuring brain activity). The brain activity recorded during the VSTMBT can help us to understand which regions of the brain are involved in remembering the coloured shapes. Some of these regions affected by AD show changes in brain activity, which allows us to understand why our memory declines as a result of the disease.

The structure of brain activity can often be thought of as a network. Each individual brain region plays a role in functions like memory, emotion, and movement, and the connections between them reflect the interactions that create our thinking and behaviour. In this way, the brain can be modelled as a network where nodes (brain regions) are connected by edges (often representing how strongly they are working together). The brain is composed of sub-networks (groups of brain regions that are working together) that help to support complex abilities like decision-making. Modularity is a method of measuring how much the network can be broken up into these separate groups. This is important to AD because, as the disease progresses, the brain network becomes more divided. This means that brain regions mostly communicate within their own groups and less across the whole brain, which can lead to worse memory and overall brain function. Traditional measures of modularity look at how separated the brain is as a whole. However, it was previously not known how individual regions of the brain contribute to this change in modularity seen in AD.

This thesis introduces a novel extension of modularity, called nodal modularity, to individual brain regions to explore MCI and AD along with other measures and models derived from it. These were explored in brain networks constructed from fMRI, EEG, and diffusion tensor imaging (DTI) which measures the white-matter networks in the brain which assist in the communication between brain regions. Nodal modularity was also explored in two types of

multiplex brain networks (multiple brain networks, also called layers, explored as one network). The first combined network layers representing different stages of the VSTMBT, with one layer representing the memorisation of the coloured shapes and the other representing the recall of that memory, allowing us to study how brain organisation changes across the different demands of the memory task. The second combined network layers representing different frequency bands from EEG, capturing how brain organisation varies across different rhythms of brain activity. Additionally, nodal modularity was tested in artificially created networks where it was confirmed that it behaved as expected and captured novel information in comparison to other network metrics. Additionally, we found evidence that suggests that nodal modularity, and the other measures and models derived from it, are helpful in modelling the different stages of AD. These advancements provide further evidence that the VSTMBT is a biomarker of AD, and provides novel methods and models to facilitate the early-detection of AD.

Acknowledgements

At times it felt like the PhD was the circus and I the monkey. Looking back at it, I think I was both.

While the PhD challenged me to grow, the people made the biggest difference. I hold such gratitude in my heart to all those that I crossed paths with in this chapter of my life. To my friends and family who supported me through the ups and downs, to my research group past and present, and to my supervisor, Javier, who not only taught me so much, but who did so with incredible kindness and patience. Without this support the PhD would not have been possible.

In addition, many of you carry unseen burdens. Despite this, you made such an impact on my life and that of many others. Thank you for being a shining light in an intense world even on the days where the weight you carry was most heavy. It meant the world to me.

Contents

Figures and Tables

Figures

Tables

Nomenclature

Acronyms

AD	Alzheimer's disease
aMCI	Amnestic mild cognitive impairment
AUC	Area under the ROC curve
DTI	Diffusion tensor imaging
EEG	Electroencephalography
eMCI	Early mild cognitive impairment
FA	Fractional anisotropy
FDR	False discovery rate
fMRI	Functional magnetic resonance imaging
MCI	Mild cognitive impairment
MEG	Magnetoencephalography
MRI	Magnetic resonance imaging
OF	Occipital-frontal – lobes of the brain
PET	Positron emission tomography
ROC	Receiver operating characteristic
ROI	Region of interest
SBM	Stochastic block model
SBTM	Stochastic block transition model
VSTMBT	Visual short-term memory binding task

Definitions

encmaint	Combined encoding + maintenance phase of the VSTMBT
MCI converters	Subjects who converted from mild cognitive impairment to Alzheimer's disease after a follow-up period
rs-	Rest, i.e., rs-fMRI stands for fMRI performed while subjects are at rest
task-	Task, i.e., task-fMRI stands for fMRI performed while subjects are performing a task like the VSTMBT

Symbols

ε	Collapsibility threshold
c	Collapsibility index measuring nQ variability in a multiplex network
nQ	Nodal modularity
Q	Modularity
TR	Repetition time

Chapter 1

Introduction

1.1 Motivation

Alzheimer's disease (AD) is the leading cause of dementia, with the global prevalence of individuals with cognitive impairment caused by Alzheimer's disease estimated at 101 million people [1]. The incidence of Alzheimer's in people 85 years and older is consistently tripling or quadrupling every 10 years, making it one of the most lethal diseases and causing an immense emotional and financial burden for patients and their families, with an increasing cost and strain on health services [1, 2]. This is of particular concern to many ageing populations across the world, given that the strongest risk factor for AD is age [3].

Understanding the complex underlying biological processes that drive the longitudinal development of AD is crucial to inform research on diagnostic methods and treatments of AD. Of particular interest is Mild Cognitive Impairment (MCI) [4, 5]. While those with MCI are at a greater risk, not all go on to convert to AD or other types of dementia. As such, there is particular interest in understanding this crucial turning point of the disease to assess the risk of AD in patients and provide treatment at this earlier stage before significant damage has been done to brain structure and function.

To this end, biological biomarkers have been discovered that assist in understanding the longitudinal progression of MCI and AD. Some examples include biomarkers for several types of proteins and their accumulation in the brain (most notably amyloid-β and tau), neurodegeneration markers from volumetric magnetic resonance imaging (MRI) or more recently neurofilament light (Nfl), measurements of synaptic dysfunction using fluorodeoxyglucose positron emission tomography (FDG PET) and the presence of neurogranin in cerebrospinal fluid (CSF)[6, 7, 8]. These, among other biomarkers, have been tracked along the AD continuum from preclinical changes in amyloid-β deposition, to clear changes in CSF, PET, and neuroinflamation markers in MCI, to large changes in hippocampal volume toward the later stages of disease [6].

Additionally, other markers of AD have been developed such as neuropsychological tests which are commonly included in the diagnostic criteria for AD [5], and genetic risk markers such as APOE $\varepsilon 4$ allele which results in a 3-4 fold increased risk of AD [2]. While the combination of biological biomarkers, neuropsychological tests, and genetic risk markers can allow us to pinpoint the progression of MCI to AD with high accuracy [9, 10], methods with greater spatial localisation that explore the individual regions of the brain that drive this change are needed.

The brain is known to be a connection of systems and subsystems that are not random, but organized and efficient on both local and global scales [11, 12, 13]. As such, the brain has been modelled as a network, where anatomical and functional connections are modelled between brain regions. Methods from graph theory applied to these networks have uncovered not only the structural and functional organization of human brain networks [14, 15, 16], but also distinct topological changes in these networks as a result of stimuli and disease [17, 18, 19]. For MCI this is no different. For example, various network metrics have been tracked through the AD disease continuum with modularity being one of the most sensitive [20]. However, modularity has exclusively been explored at a global level. The extent to which individual regions of the brain contribute to modular community organization in the brain and how this changes due to stimuli or disease is not fully understood. This is despite clear evidence that modularity is fundamental to brain structure and function [15, 21, 22, 11, 23, 20, 24, 25, 26, 27]. This motivates the development of novel network metrics for AD and especially those sensitive to the early-stages, where less damage has been done.

Furthermore, the impact of AD on functional networks (based on correlations in brain activity) and structural networks (based on anatomical white-matter connections) is not fully understood. This is particularly the case in recent extensions of classical brain networks to multiplex models, which are composed of multiple networks (called layers), where each layer of the network captures different types of connectivity such as functional and structural connectivity, or brain dynamics across time or frequency [28]. In addition, research of human brain networks for task-based data have seen significantly less study than research where subjects are at rest. This is especially the case in the exploration of AD and multiplex networks, despite the existence of tasks sensitive to the early-stages of AD [29] and where multiplex networks of task-based data can yield novel insights beyond those of classical networks [17].

This thesis explores multiplex models of human brain networks for a visual short-term memory binding task (VSTMBT) [29], a task sensitive to early-stage AD, and along the stages of MCI (with emphasis on the turning point of MCI to AD conversion). Furthermore, it expands on classical modularity, utilizing it for the development of novel network metrics to categorize the stages of AD at a granular level. Modularity was selected for its known progression in AD [20], along with its interpretability, since modular organization is a hallmark of human

brain networks and its disruption reflects changes in network segregation due to disease [15]. Additionally, these novel network metrics which capture the stages of AD pave the way for the simulation of damage to functional and structural brain networks over time and allow for the potential to fingerprint subjects based on disease trajectory.

1.2 Aims and Objectives

This thesis aims to advance current methods of analysing and modelling human brain networks to improve our understanding of AD and how it progresses. This will be done specifically through the development of novel network measures and models for single and multiplex networks, providing a granular analysis of networks in fMRI, DTI, and EEG in early-AD, and thus helping to categorize disease stages.

To this end, we introduce the following objectives.

1. To develop a novel measure of capturing localized modularity (overcoming its global limitations) for a finer grain analysis of meso-scale network architecture in single and multiplex networks.
2. To ensure that this novel measure is applicable to large multiplex networks for use in neuroimaging and provide novel aggregate measures to improve interpretability.
3. To explore fine grain changes in neuroimaging data of AD.
4. Introduce novel targeted attack models which explore alternative methods of attacking meso-scale network architecture for use in task-fMRI.

1.3 Contributions

Thus, the contributions of this thesis are the following:

Multiplex Nodal Modularity for the characterization of MCI for a working memory binding task. We introduce a novel measure of nodal community structure in single and multiplex networks - Nodal Modularity. This extension of classical modularity enables a more granular characterization of network organization, providing novel insights into nodal group structure compared to the state of the art, and was made publicly available here: `https://github.com/AvalonC-C/Nodal_Modularity`. We demonstrated its effectiveness in differentiating a key turning point of amnestic MCI to AD conversion by exploring networks constructed from single layer task-fMRI, DTI, and multiplex task-fMRI networks. Additionally, we carried out the first network based exploration of the VSTMBT in fMRI. This contribution was published in PLOS One [30] and it addresses the research objectives 1 and 3 in Section 1.2.

Exploration of nQ and its variability in multiplex networks of EEG for a short-term memory binding task in MCI. We quantified the utility of nQ in large multiplex surrogate networks by exploring it and other multiplex network measures and showed that nQ maintains novel behaviour as network size increased. Additionally, we introduced a novel aggregate measure of nQ, collapsibility (made publicly available here `https://github.com/AvalonC-C/Collapsibility`), and assessed the ability for nQ and collapsibility to detect granular changes in MCI for larger networks constructed from VSTMBT-EEG in source space. We found that changes in both nQ and collapsibility agreed with disease markers of MCI and behaviour of the VSTMBT. This chapter addresses research objectives 2 and 3 in Section 1.2.

Simulation of disease progression via novel targetted attack methods. We develop three novel targetted attack methods using nQ and brain-lobe based segregation for the simulation of AD progression for VSTMBT-fMRI data. We explored how network disruptions due to AD affect functional connectivity in task-fMRI networks and found that a prior state-of-the-art model did not extend to task-fMRI of early-AD. However, lobe-based segmentation followed by attacks on node hubs or nQ performed best in modelling the organizational changes in functional connectivity that occurs in early-AD. This chapter addresses research objectives 3 and 4 in Section 1.2.

1.4 Structure of this thesis

Chapter 1 – Introduction. This chapter included the motivations, objectives, contributions, and the structure of the thesis. It establishes the context for the remaining chapters.

Chapter 2 – Background. This chapter provides a detailed overview of the background required for the thesis that includes Alzheimer's disease, neuroimaging, and network neuroscience.

Chapter 3 – Multiplex Nodal Modularity: A novel network metric for the regional analysis of amnestic mild cognitive impairment during a working memory binding task. This chapter introduces a novel measure of nodal community structure in single and multiplex networks - Nodal Modularity (nQ). This extension of classical modularity allows for a more granular characterization of network organization and is applied to brain networks during the VSTMBT. The chapter first provides a brief introduction on AD and the use of modularity in network neuroscience. Then, it formally defines nQ, the VSTMBT, and describes the real-world neuroimaging data and benchmark networks used to evaluate nQ. Further sections describe the experimental validation of these methods and discuss how nQ can be used to characterize the stages of MCI and the implications of this advancement.

Chapter 4 – Exploration of nQ and its variability in multiplex networks of EEG for a short-term memory binding task in MCI. In this chapter we quantify the utility of nQ and a novel aggregate measure of nQ (collapsibility) in large multiplex surrogate networks and real-world neuroimaging data. This chapter begins by providing background on the use of multiplex networks in network neuroscience and the interpretation of nodal network measures in this context. The following section describes the methodology around surrogate network construction, novel aggregate network measures derived from nQ (collapsibility), statistical methodology, and description of real-world neuroimaging data. Later sections present the results of the research on surrogate networks, what this means for nQ and collapsibility, and discussion on the application of these measures to VSTMBT-EEG in MCI.

Chapter 5 – Targeted attacks on occipital-frontal functional connections simulates AD progression for a visual short-term memory binding task. This chapter presents the development of three novel targeted attack methods using nQ and brain lobe-based segregation for the simulation of AD progression for VSTMBT-fMRI data. The chapter begins by introducing the use of targeted attacks in AD research. The following section describes the neuroimaging data, benchmark attack models, novel attack models, and network analyses used in the research. Subsequent sections present the comparisons of the different targeted attack models and discuss the application of targeted attack models to task-fMRI and the implications from technical and clinical perspectives.

Chapter 6 – Thesis overview. This chapter covers the discussion, limitations, future work, and conclusions of the thesis.

Chapter 2

Background

2.1 Characterization of AD through network science

This chapter covers the fundamentals for analysing and understanding biophysiological systems such as the brain with a focus on the neurodegenerative processes that govern Alzheimer's disease (AD). More specifically, by exploring AD and its current challenges, discussing neuroimaging methods as biomarkers, and finally, by using network science as a methodology to extract meaningful insights from biomedical signals.

2.1.1 Alzheimer's Disease

AD, the most common form of dementia, places immense emotional and financial strain on families and public services. In the UK, there are approximately 850000 people with dementia, aged 65 or older, projected to rise to 1.6 million by 2040. Furthermore, the total cost, composed of health care, social care, and unpaid care, is expected to increase from 34.7 billion to 94.1 billion pounds [31]. AD causes progressive cognitive and intellectual decline, affecting memory and reasoning and can lead to difficulties in communication, disorientation, and loss of independence [2]. While AD primarily affects older adults, genetic risk factors along with cardiovascular and general health can contribute to its progression. AD develops gradually, where changes in the brain can begin up to 20 years before clinical symptoms become apparent [32]. This leads to diagnostic challenges, especially given that AD is varied among individuals and the exact cause of disease is still under investigation [2].

At a biological level, AD disrupts the complex cognitive processes of normal brain function. Specifically, AD results in a gradual loss of neurons, synaptic dysfunction, and grey and white matter shrinkage in key brain regions integral to memory such as the hippocampus, with further brain wide atrophy in the later stages [2, 33, 34]. This results in abnormal brain structure and function that interferes with the brain's ability to process information efficiently, leading to clinical symptoms that can be assessed for diagnosis.

Diagnostic criteria for AD commonly includes clinical evaluations and cognitive testing through neuropyschological tests. Patients can first present with mild cognitive impairment (MCI), of which the memory-related subtype (amnestic mild cognitive impairment, aMCI) is considered a prodromal stage of AD [5]. MCI is defined as a cognitive decline which is greater than that caused by normal aging. It can be viewed along a spectrum, ranging from normal cognition to dementia [4]. MCI diagnosis is typically achieved through a collection of cognitive questionnaires, screening tests, and neuropyschological examinations [7]. These are used to benchmark and assess changes in memory, visuo-spatial ability, language, and behaviour. While not everyone with MCI goes on to develop dementia, those with MCI are at much greater risk. Furthermore, progression happens quickly. Those who have a diagnosis of aMCI and who convert to AD (MCI converters, or MCIc) typically do so at a conversion rate of 12% per year [35]. Thus, disease detection in the early stages is crucial before significant damage has been done. Additionally, early detection allows families and individuals to plan for the future, initiate lifestyle changes and access support services [36]. In addition to improved disease staging, understanding the early stages allows researchers to validate predictive models and test disease-modifying treatments at crucial stages of the disease to determine the most effective windows for intervention [37].

To understand these complexities, AD research has been explored across a vast array of domains. For instance, genomics research has discovered both risk increasing and protective genes (*APOE* $\varepsilon 4$ allele and *APOE* $\varepsilon 2$ respectively [2]). Pathophysiologically, abnormalities observed in astroglia, microgila, and neurons [34] drive the progression of preclinical AD along with increased neuroinflamation [38], and vessel [39] and glymphatic dysfunction [40].

In recent years, biomarkers have been a main focus of research for AD staging and understanding. This is due to AD having unique neuropathology, whereby current biomarkers are sufficient for diagnosis even where clinical symptoms are not present [41]. However, it should be noted that a large panel of biomarkers are needed to accurately diagnose AD. Clinical, organizational, and budgetary constraints can limit biomarker access, meaning that clinical diagnosis often focuses on obtaining the largest amount of information from the lowest number of examinations [42]. So while biomarkers of AD can illuminate the underlying disease pathology, clinical diagnosis of AD can be limited in its specificity and not entirely reflective of the underlying pathological progression. Emphasis has been placed on optimizing clinical workflows that promote consistent diagnosis of the disease [42], and especially in early detection, where disease-modifying treatments are more effective and where the evaluation of future disease modifying drugs can be supported.

2.1.2 Biomarkers of Alzheimer's Disease

The identification of biomarkers for AD represents a breakthrough in the understanding of underlying disease pathology and has helped to determine the AD continuum. These include biomarkers for several types of proteins and their accumulation in the brain (most notably amyloid-β and tau), neurodegeneration markers from volumetric MRI or more recently blood-based markers, neurofilament light (Nfl), and measurements of synaptic dysfunction using fluorodeoxyglucose (FDG) Photon Emission Tomography (PET) and the presence of neurogranin in CSF [41, 6, 7, 8]. These, among other biomarkers, have been tracked along the AD continuum from preclinical changes in amyloid-β deposition, to clear changes in CSF, PET, and neuroinflamation markers in MCI, to large changes in hippocampal volume toward the later stages of disease [6]. See Fig. 2.1 for an illustration of how biomarkers for AD progress along the AD continuum.

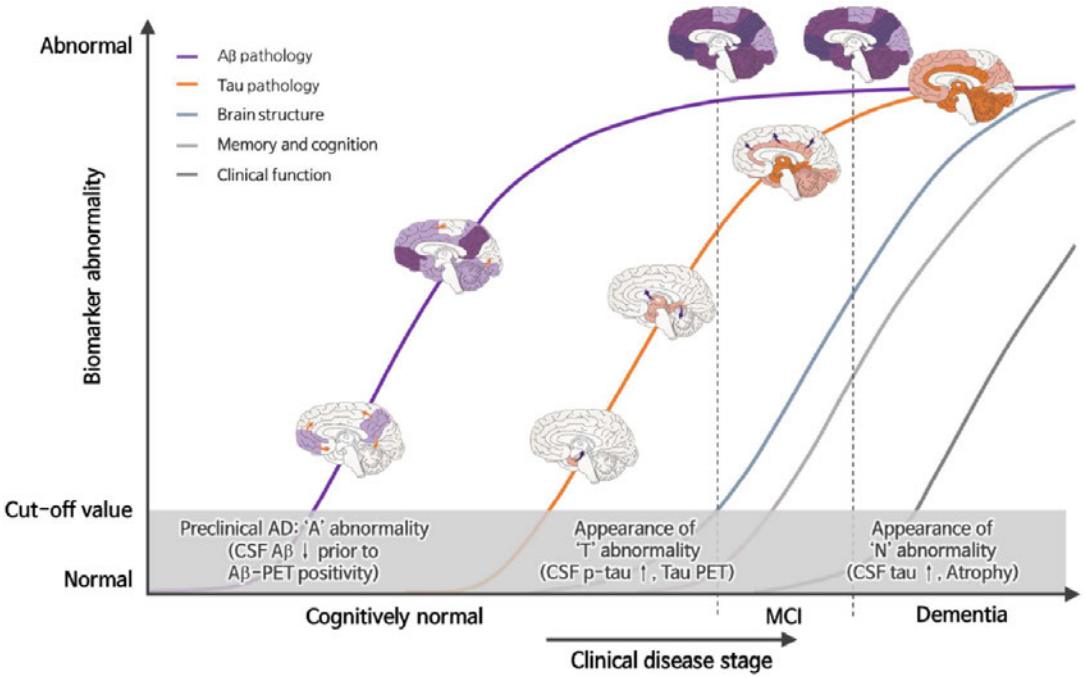

Figure 2.1: Biomarker progression in AD. The pre-clinical stages of AD are described by abnormalities in CSF measured amyloid-β. This is followed by abnormalities in CSF measured phosphorylated-tau or PET measured tau and then increased CSF total tau and atrophy of the hippocampus in the later stages. These changes in amyloid-β (A), tau (T), and neurodegeneration or neuronal injury (N) comprise the ATN criteria used for the disease staging of AD [43]. This figure was reproduced from Mankhong *et al.* [43].

Furthermore, several biomarkers, such as amyloid-β deposition and regional hypometabolism indicating synaptic loss, can be assessed at a brain regional level allowing for improved staging of disease severity. Research suggests that, for amyloid-positive subject groups, amyloid deposition is most strongly found in the hetermodal association areas of the frontal, parietal, and lateral temporal lobes [44]. Beginning in preclinical stages (for amyloid positive

subjects), increasing through the pre-dementia stages (early to late MCI, or eMCI and lMCI) and presenting most strongly in AD. Evidence also points to the medial temporal lobe (MTL) as a key region in early-stage AD both in grey matter atrophy [44], and in functional activity [45]. Studies suggest that the AD continuum begins with damage to the MTL followed by broader damage to other networks such as those part of the frontal lobe [46, 47, 48].

While the combination of biological biomarkers, neuropsychological tests, and genetic risk markers can allow us to pinpoint the progression of MCI to AD with high accuracy [9, 10], methods with higher specificity (for instance neuroimaging methods with high spatial resolution such as function magnetic resonance imaging, fMRI, and diffusion tensor imaging, DTI) that explore the individual regions of the brain that drive this change are needed. This motivates the development of novel biomarkers for AD. Especially those sensitive to the early-stages of disease, where less damage has been done.

In addition, current biomarkers face challenges in accessibility, geographical research bias, and invasiveness [49]. Neuroimaging methods such as PET and MRI are costly, while CSF is invasive, deterring clinical use. These factors contribute to a concentration of research in high-income countries, causing geographical research bias in AD diagnosis and understanding [49]. In contrast, blood-based markers present an exciting development due to their low-cost and non-invasive nature [41]. However, blood-based markers often require complimentary methods (i.e., neuroimaging) to increase diagnostic specificity or understand functional disease progression [41].

A complimentary method of measuring functional brain activity which is both a cheap and non-invasive technology is electroencephalography (EEG). EEG measures the electrical neural activity in the brain as a result of normal brain function and how this changes due to disease [50]. However, EEG is challenging to apply effectively to early-stage AD due to high inter-subject variability in the disease and EEG noise [2, 50]. To address this, task-based EEG research aims to overcome this by targetting specific deficiencies in cognitive brain function known to be affected in AD, and isolate these neural markers of progression [51]. One such neurocognitive biomarker is the visual short-term memory binding task (VSTMBT) [29].

2.1.3 Working Memory and Cognitive Biomarkers

The VSTMBT, introduced by Parra *et al.* [29], is a task sensitive to early changes in AD, and is composed of eight non-nameable shapes and colours with three phases named encoding, maintenance, and probe. Participants are presented these shapes and colours on a screen (encoding), must memorize this information (maintenance), and are then presented the same or a different set of shapes and/or colours (probe) and must click a button in their left or right hand indicating whether they are different or the same. It is important to note the distinction between shapes and coloured shapes in the above as two separate tasks. From here on, the *binding* task refers to coloured shapes, while the *shape* task refers to shapes only.

The three stages (encoding, maintenance, and probe) of the VSTMBT aim to target a process called feature binding in the brain. Feature binding refers to the formation and consolidation of distinct features (i.e., visual features - colour, shape, orientation, etc.) for temporary storage and retrieval [52]. During encoding, the brain must first break down the object into individual features, hold these features in memory (maintenance), and then retrieve them (probe). It is important to note that evidence suggests that the processes behind short-term memory binding, such as those targeted in the VSTMBT, are distinct from the processes that govern long-term memory [53, 54, 55], and which are subsequently affected differently by age and brain damage [56, 57, 58]. This is an important distinction, given that long-term memory is affected by normal aging.

For healthy individuals, aging typically results in a natural decrease in memory performance [59]. This can include losing track of the location of objects or forgetting names and dates. This decrease in the ability to bind features in long-term episodic memory along with associative deficits in working memory [60, 61] is suggested to be dependent on hippocampal dysfunction [62, 63] as a natural result of functional and structural decline in the hippocampus with healthy aging [64, 65]. However, conjunctions between certain features (such as between colours and shapes) are not affected by natural aging.

This makes tasks which target short-term memory binding especially important for AD given that they remain relatively unchanged with age while being highly sensitive to the disease [29]. This sensitivity is specific to AD where conjunctive short-term memory binding (i.e., between colour and shape) is impaired as opposed to other, non-AD, dementias where this effect is not observed [66]. Additionally, these performance impairments on the VSTMBT were observed for both the preclinical stages of familial and early-stage sporadic AD [29, 56], where VSTMBT performance was also seen to correlate with amyloid-β deposition [67, 68]. This evidence suggests that deficits in short-term memory binding is a pre-clinical marker of AD.

As a consequence, it becomes natural to question whether the underlying neural activity reflects these changes in short-term memory binding, which we explore in the next section. By understanding underlying neural processes, cognitive biomarkers can be used to enhance the understanding of AD neuropathology and improve disease staging and detection. This is especially exciting in applications of the VSTMBT with EEG given that it is a low-cost technology, non-invasive, and that the VSTMBT has been validated across multiple regions [69, 70, 51, 48, 71] avoiding some of the previously mentioned geographical bias [72]. This presents an exciting way forward as researchers explore the neural markers of AD through neoroimaging methods in conjunction with the VSTMBT, leading to potential improvements in clinical diagnosis and understanding of AD.

2.2 Neuroimaging

The field of neuroimaging has been integral in the understanding of functional, structural, and connective aspects of the central nervous system with a focus on the brain. In a clinical setting, neuroimaging methods, such as MRI, provide invaluable diagnostic capabilities to detect a plethora of abnormalities in the brain such as tumors, inflammation, and bleeding. Other neuroimaging methods such as PET and magnetoencephalography (MEG, which measures the electrophysiological activity of the brain) also show clinical use in the measurement of amyloid-β and tau in AD [41] and screening for some types of epilepsy [73, 74], respectively. To explore early-stage AD, this section provides an overview of three neuroimaging modalities used in Chapters 3, 4 and 5 – functional magnetic resonance imaging (fMRI), Diffusion Tensor Imaging (DTI), and electroencephalography (EEG). While these methods are not established biomarkers of AD, they offer insight into how VSTMBT function changes with disease progression (in the case of fMRI and EEG) and explore the associated structural changes in the brain (DTI).

2.2.1 fMRI

MRI is a method of acquiring structural images of soft tissue in the body through the use of strong magnetic fields and radio waves. MRI has widely been used for its medical diagnostic capabilities, but it was the emergence of fMRI that largely influenced neuroscience research [75]. fMRI measures the haemodynamic activity in the brain, an action occurring in response to neural activity. These changes in blood flow and oxygenation provide a blood oxygen level-dependent (BOLD) signal which can yield insights into the neural function of the brain, allowing us to study and understand aspects of the brain such as cognition, memory, and sensory processing [75]. BOLD signal can be explored at rest (resting state fMRI or rs-fMRI), or during a cognitive task (task-fMRI).

Locating changes in brain blood flow is made possible due to the precise spatial accuracy of fMRI and whole brain imaging. However, fMRI has several drawbacks. For instance, fMRI suffers from poor time resolution due to the time it takes for the haemodynamic response to occur and reset [50]. That is, analysis methods must take into account the temporal delays in blood movement in the brain. Additionally, fMRI typically has a repetition time (TR - the amount of time to take a whole-brain image) of a few seconds [75]. This can limit the temporal accuracy of BOLD signals, especially when some tasks illicit fast responses in brain activity. Lastly, fMRI is costly and not widely available. This combined with uncomfortable conditions within the scanner (claustrophobia and hard surfaces leading to movement and thus noise), and potentially long scan times, means that data for patients with AD can be hard to find with large sample sizes.

fMRI can be combined with tools such as statistical parametric mapping (SPM), which uses statistical maps to determine the probability of activity occurring in different locations in the brain, allowing for the identification of abnormalities in BOLD signal as a result of AD. For instance, for a verbal short-term memory binding task-based fMRI study, they identified reductions in neural activity in key brain regions involved in encoding and retrieving stored short-term memories [76]. Similar methods of SPM were also used to explore the activation maps of the VSTMBT for healthy subjects to understand whether holding objects within working memory whose features need to be bound together would required dedicated neural resources separate to those required for the individual features separately [77]. However, fMRI-based studies of the VSTMBT are scarce, including in relation to AD. This is aside from recent work in multi-modal DTI and fMRI network-based models co-authored and published in tangent to this thesis [78, 79].

2.2.2 DTI

DTI stems from diffusion-weighted imaging (DWI), another MRI-based imaging modality, which measures the displacement of water molecules in the brain. Due to the movement of these molecules around white matter, consisting of neuronal fibers (axons), DWI can separate grey and white matter in the brain, effectively mapping the structural connectivity between each region [80]. From these images, DTI is formed through methods of tractography used to trace and reconstruct white-matter fibres from the diffusion weighted images that carry information on the direction and amount of water diffusion, given that water diffuses more easily along the direction of the white-matter fibers. Using the reconstructed fibers of our DTI, we can measure aspects of regional white-matter such as structural density (SD, white-matter density), fractional anisotropy (FA, white-matter microstructure), and mean diffusivity (MD) [80]. It should be noted that while DTI has high spatial resolution, it comes with some similar drawbacks to other MRI-based imaging methods. Specifically, and like fMRI, DTI is costly, not widely available, and can have long scan times (resulting in potential movement leading to noise) [81].

By analysing regional measures of white-matter microstructure and density, DTI can be used to understand changes in brain architecture due to brain related injury or disease [82]. For instance, AD directly impacts these white-matter structures which facilitate information transfer in the brain. Specifically, abnormalities in FA and MD are seen throughout the AD continuum from early to late AD [83, 84, 85]. For instance, increased MD were consistently found in areas with neurofibrillary tangles caused by AD pathology such as the hippocampus [86, 87, 88, 89]. Furthermore, studies have consistently shown that white-matter is altered in AD such as in the degeneration of axons, and changes in myelin (the insulating sheath around axons) and oligodendrocytes (the cells that produce and maintain myelin) [90, 91, 92]. Given the clear

changes in white matter in AD, DTI shows potential for early-detection and understanding of disease progression. Furthermore, and since DTI measures the white matter connectivity between brain regions, research on DTI often focuses on network-based approaches which will be described in Sections 2.3 and 2.3.4.

2.2.3 EEG

EEG is a measurement of the currents that form when there is an excitatory response from the neurons and synapses in the brain. These are measured through sensors placed on the scalp [50]. The most common sensor layout is the international 10-20 system, typically consisting of 21 electrodes, although higher density versions with 64 or 128 electrodes exist as well [93]. While EEG has the ability to capture electrophysiological recordings at a high temporal resolution (greater than other neuroimaging techniques such as MRI-based methods), allowing for the study of fast dynamical changes in brain activity, it suffers in spatial resolution as opposed to other methods such as MRI. Specifically, EEG is measured through conductive electrodes placed on the scalp. Even with a large number of electrodes, there are inherent limitations in measuring internal electrical sources at scalp-level, given the effects of volume conduction [94]. However, these internal electrical sources can be estimated with source localization techniques to obtain approximations of where scalp-level activity originates, yielding higher spatial resolution (source-space EEG) [94].

EEG signals are typically broken up into specific frequencies, typically beta (>13Hz), alpha (8-13Hz), gamma (4-8Hz), and delta (0.5-4Hz) [95]. These different frequency bands carry unique information on brain-related activity such as beta wave dominance during wakefulness, and delta during deep sleep. These changes are also seen in rs-EEG and task-EEG, where stimuli can evoke complex changes in brain electrophysiology [50].

EEG has been extensively investigated as a tool for the understanding and diagnosis of AD. The hallmark changes in EEG as a result of AD are a shift in electrophysiological activity from the faster beta and alpha rhythms to slower theta and delta [96]. As the disease becomes more severe, so too do these abnormalities [97]. Additionally, a reduction in the complexity of electrical activity [98, 96, 99], decreased synchronization as a result of reduced connectivity between cortical regions [100, 101], reduced frontal delta/theta and posterior alpha rhythms [99], among others, have been observed as a result of AD. These results are posited to reflect the neuronal and synaptic losses and general brain atrophy observed in AD, and which lead to abnormal electrophysiology. Thus, there is potential for EEG to become a pre-screening tool for AD [7].

The volume conduction and poor spatial resolution mentioned previously, combined with noise already present due to eye blinks, movements, heartbeat and other environmental factors leads to limitations. Despite these factors, EEG has found success in clinical research, in part due to its relatively high availability and low cost [7]. Application of methods that work for EEG data have the potential to be more widely available both locally and geographically, leading to improvements in geographical biases and clinical accessibility.

While fMRI, DTI and EEG have been key to the understanding and diagnosis of AD, it is still unknown how individual brain regions are engaged during the VSTMBT and how this changes along the AD continuum. This is especially the case in how these interconnected brain processes interact and dynamically change over time and with disease. Network-based approaches to study these interactions within the VSTMBT have not yet been explored despite the advent and growth of the field of network neuroscience in recent years [16].

2.3 Network Neuroscience

2.3.1 The brain as a network

The brain is a highly connected organ. Its network is composed of nerve cells as part of the central nervous system (CNS – consisting of axons, synapses, and dendritic membranes), located between individual neurons, and which propagate the electrical signals that neurons generate [50]. While there are many individual systems in the brain that are highly connected, such as the vascular and metabolic systems, CNS-based networks reflect brain activity (excitatory electrical responses to stimuli which propagate between neurons and synapses, and the blood movement which supports this) and structural connectivity (neuronal fibres consisting of axons) which can be captured in the fMRI, DTI, and EEG data used in Chapters 3, 4 and 5 [50, 16].

Modelling complex systems such as the brain can be challenging as they are composed of multiple subsystems, layers of connectivity, evolving components, and many more [102]. To represent this data, many domains use methods in network science and graph theory to both model and explore the underlying mechanics in the interactions between objects such as regions of the brain (defined anatomical structures such as the amygdala). To do this, we can separate the data into their constituents (nodes) and relationships or interactions (edges) between them, forming a network. Furthermore, edges can be directed (one-way relationships) or undirected (two-way relationships), given a value (weighted), and nodes can be part of different groups (based on shared properties such as similar patterns in connectivity) [16]. Many other methods of construction exist, some of which will be discussed below, to model complex systems effectively and in accordance to their function. Once modelled in this way, graph analysis techniques can be used to uncover underlying patterns in the data or network-based changes due to disease [16]. The application of network science and graph theoretical

methods to neuroscience has recently been coined *network neuroscience*. It represents a direction in neurobiological research, pushed by the advent of big data in neuroscience, and the need for advanced analytical techniques to understand the structural and functional dynamics in the brain [16].

2.3.2 Graph theory

To model and measure the qualities of neurobiological networks requires us to explore formally what is a graph. Graph theory is the study of graphs which capture the relationships between objects. Here, we focus on formally defining undirected graphs which assumes a symmetric relationship between regions. This reflects practical constraints in modelling connectivity in the brain, given that many neuroimaging methods are unable to directly detect anatomical or causal directionality [103]. As a consequence, while graphs constructed from the brain are useful for characterizing network structure, they should not be interpreted as providing evidence of causal interactions without additional assumptions or modelling considerations.

Formally, we define $G = (V,E)$, as a *weighted undirected graph* composed of a finite set of *vertices* (also known as *nodes*), $V = \{v_1, v_2, ..., v_n\}$, and a two-element subset of V called *edges* ($\{E \subseteq \{v_i, v_j\} | v_i, v_j \in V\}, i \neq j\}$) and where $w : E \to \mathbb{R}$ is a function that assigns weights to each edge (also defined as $w(\{v_i, v_j\})$ or w_{ij} denoting the weight between two vertices $v_i, v_j \in V$) [104]. When a pair of vertices share a single edge $\{v_i, v_j\} \in E$, we say that the two vertices are *adjacent* to each other and that the edge is *incident* to each of our vertices. In addition, we define the *adjacency matrix*, $A \in \mathbb{R}^{n \times n}$ of G, as the symmetric matrix whose entries are given by

$$A_{ij} = \begin{cases} w_{ij}, & \text{if } \{v_i, v_j\} \in E, \\ 0, & \text{otherwise.} \end{cases}$$

It is the application of graph theoretical approaches to real-world data that often differentiates the study of network science from the study of graphs. Unless specifically discussing graph theoretical methods and algorithms, from here on we describe the above formal definition of a graph, in relation to neuroimaging, as a network. Similarly, we limit our use of "vertex" only when describing formal graph-theoretical definitions, while "node" is used more generally for discussions of networks.

2.3.3 Applications to neuroimaging

Viewing the brain as a network allows for the exploration of how connectivity changes over time, at rest, for a task, or with disease. In network neuroscience, networks typically model brain regions as nodes, while the connections (edges) between them encode information on the relationship between those regions' function (functional connectivity) or structure (structural connectivity) [16]. In the case of fMRI, edges are often a measure of functional co-activation between blood oxygen level dependent (BOLD) time-series between a pair of brain regions [18]. Meanwhile, in DTI, an edge typically represents the fractional anisotropy (FA) between regions (measuring white matter micro-structure), or streamline density (SD - representing white matter density) [21]. For EEG, edges often measure the functional co-activation between time-series of electophysiological activity at the level of EEG sensors, or brain regions (estimated from source localization) [105]. These models capture the topology of the brain, revealing fundamental insights into how the brain is functionally and structurally organized, and how this changes due to disease.

In the case of functional network construction in fMRI, co-activations are often determined by statistical measures of correlation, such as Pearson's correlation, between functional time-series of activity between brain regions [106]. In this way, connections between brain regions are established based on the extent at which they are correlated (i.e., co-activating). This is typically done between all pairs of brain regions, leading to the construction of a functional network. Strong correlations in BOLD signal between brain regions have been observed in a wide number of studies leading these co-activations to become a hallmark of human brain networks [18]. For EEG functional networks, measures of phase such as the weighted phase lag index (wPLI) are often used to avoid the issues with volume conduction mentioned in Section 2.2.3 [107]. Once the functional network is constructed, some studies take the weighted network as is, while others binarize the network edge weights above a threshold or prune edges to avoid spurious connectivity [103]. This can help to reduce noise and enhance interpretability. However, it also risks removing subtle patterns of brain connectivity. The effects of these pre-processing choices depend on the specific network measures used, as some metrics (such as modularity) may be more sensitive to edge density or topology and where weighted networks provide complimentary aspects of network organization [108, 103].

Functional brain networks reveal important features of how the brain communicates. For example, at rest, the human brain forms distinct sub-networks of functionally connected regions [18]. These sub-networks are composed of a collection of brain regions that consistently co-activate, and where each sub-network contributes to specific aspects of brain function. Of particular note is the frequently reported on *default mode network* consisting of precuneus, medial frontal, and inferior parietal and temporal regions [109, 110]. This sub-network has

been linked to core processes in human cognition and emotional processing, and as such, is of interest in exploring neurologic and psychiatric disorders [111]. In fact, it has been shown that AD not only affects DMN connectivity, but also large-scale brain networks that extend well past the DMN [112].

While research has focused on the study of resting-state fMRI to focus on describing an intrinsic functional connectivity profile for subjects at rest, evidence suggests that task-based fMRI shares some underlying intrinsic architecture with rs-fMRI, functional connectivity evoked by specific tasks and some general changes shared among different tasks [113]. Understanding these task-specific and task-general changes in functional connectivity can allow for the targeting of specific functional networks and how these are damaged by diseases such as AD. For example, there has been focus on targeting attentional networks in AD using three specific task paradigms (animacy, memory, and Stroop tasks) [114], given that attentional networks are among the earliest disrupted systems in AD and are closely linked to memory processes. Disruptions in these networks may impair the allocation of attentional resources necessary for effective encoding and retrieval, contributing to the memory deficits often observed in AD. Similarly, it is natural to question how other cognitive biomarkers of AD, such as the VSTMBT, present in networks.

Networks derived from EEG source-space analyses also display similar sub-network characteristics at rest. For example, source-space networks constructed from high-density EEG show connectivity resembling the DMN, visual, auditory, and attention networks, comparable to those seen in fMRI [115]. However, source-space EEG networks have their own characteristics due to a greater sensitivity to fast temporal dynamics and lower sensitivity to deep brain signals (when compared to fMRI). For AD, these changes are observed as progressive disruptions in functional connectivity, particularly in the alpha band, with notable reductions in long-range connections such as those between frontal-parietal and frontal-temporal regions [116]. These disruptions are present across disease stages and worsen with AD progression. Since attentional processes depend heavily on fronto-parietal networks, these changes may contribute to early and persistent deficits in attention, memory and executive function in AD [117].

For structural brain networks of DTI, tractography naturally lends itself to their construction. Specifically, tractography estimates the structural connectivity by quantifying the SD and FA between regions, which form the edges of the network. From this point, the network is often thresholded or filtered for spurious or biologically implausible connections [118]. Networks constructed from DTI show consistent organizational patterns, such as small-world topology and modular sub-networks, which are thought to support efficient information integration and segregation in the brain (described in Section 2.3.10) [119, 120]. In the context of AD, these structural networks undergo notable alterations, including overall decreases in white-matter

connectivity strength, reduced global efficiency, and abnormal topological organization [119, 121]. These changes reflect a progressive decline in the brain's ability to effectively communicate, potentially leading to some of the cognitive and functional impairments observed in AD.

2.3.4 Network Metrics and Applications

Previously, we discussed how network-based methods of modelling are natural in capturing the connected nature of brain function and structure. To understand how these networks are topologically organized, this section will first describe some of the key network measures used to understand brain topology – degree centrality, clustering coefficient, PageRank, path length, node eccentricity and modularity – before exploring how insights derived from these measures inform our understanding of the brain and how it changes due to disease.

2.3.5 Degree centrality

Degree centrality, often shortened to degree, is a measure of node importance defined as the number of edges adjacent to a node [122]. For a weighted graph, this is analogous to the sum of the weights adjacent to a node, also known as node strength. That is, for a weighted and undirected graph $G = (V, E)$, and for a vertex $i \in V$ with $\{j \in V \mid (j,i) \in E\}$, the degree, k_i, of i is:

$$k_i = \sum_{j \in V} w_{ij}. \tag{2.1}$$

Nodes with high values of degree are often considered of higher importance, or more central within their networks, due to the multitude of connections the node has.

2.3.6 Clustering coefficient

Clustering coefficient is a measure of local connectivity, measuring the number of triangles for a node in a graph divided by the number of possible triangles that could exist for that node [122]. In essence, it is a measure of how likely a node's neighbours are to also be connected. For a weighted network, one of the most commonly used extensions is that based on the average "intensity" (geometric mean) of all triangles associated with each node [123]. Formally, for a vertex i, let $\hat{w}_{ij}$ be the normalized edge weight such that $0 \leq \hat{w}_{ij} \leq 1$. The weighted clustering coefficient C_i is defined as:

$$C_i = \frac{1}{k_i(k_i - 1)} \sum_{\substack{j,m \in N(i) \\ j \neq m}} (\hat{w}_{ij} \hat{w}_{im} \hat{w}_{jm})^{1/3} \tag{2.2}$$

where $N(i)$ is the neighbourhood of i (vertices that share an edge with i).

2.3.7 PageRank

PageRank captures the behaviour of a random walker traversing nodes in a network [124]. To calculate the PageRank centrality of a node i we follow two strategies: 1) to jump to a node selected uniformly at random and, 2) to jump to a neighbouring node with probability $\alpha \in [0,1]$ (called the dampening factor). The PageRank centrality for node i is then defined as the frequency of repeat visits to itself along this random walk. Formally, the weighted PageRank (x_i) of a node i is defined as:

$$x_i = \alpha \sum_j A_{ij} \frac{x_j}{g_j} + (1-\alpha)\frac{1}{N} \tag{2.3}$$

where $g_j = \max(1, k_j)$ and N is the total number of nodes. PageRank is another measure which captures the centrality of a node based on the frequency a random walker would visit it.

2.3.8 Path length and eccentricity

The weighted characteristic path length quantifies the efficiency of information transfer in a weighted network. Following the definition introduced by Stam et al. [125], we define the weighted characteristic path length of a vertex i (PL_i), as the harmonic mean of the shortest path lengths from vertex i to all other vertices:

$$PL_i = \frac{1}{\frac{1}{N-1}\sum_{\substack{j \in V \\ j \neq i}} \frac{1}{L_{ij}}} \tag{2.4}$$

where L_{ij} is the shortest path length between vertex i and j, calculated from the weighted adjacency matrix using the inverse of connection strengths as edge lengths. This definition ensures that vertices with more efficient access to the rest of the network (via shorter paths) will have a lower path length.

In addition, we define the node eccentricity of a vertex i, $e(i)$, as the largest shortest path between i and all other vertices in the graph ($\max L_{ij}$) [126].

2.3.9 Modularity

Previously, in Section 2.3.3, we have discussed the importance of sub-networks in the understanding of functional and structural brain networks. To determine sub-networks, community detection algorithms are employed to partition the graph into *communities*, also called *groups* and *modules*, of vertices. These communities are groups of vertices which can share common properties and/or play similar roles within the graph [122].

Here, we focus on modularity maximization as one of the most common methods of community detection. The modularity quality function (Q) measures the number of edges that fall within the groups (g_i denotes the group assignment of v_i), minus the expected number of edges that would exist if placed at random [127, 128]:

$$\mathrm{Q} = \frac{1}{2m} \sum_{ij} \left[A_{ij} - \frac{k_i k_j}{2m} \right] \delta(g_i, g_j). \tag{2.5}$$

More specifically, for our graph G, we have the sum over all edge weights (A_{ij}) that exist within the same group ($\delta(g_i, g_j) = 1$ when $c_i = c_j$, and 0 otherwise), minus the expected edge weight if edges were placed at random ($\frac{k_i k_j}{2m}$). Here, k_i denotes the degree of v_i, and m is the number of edges (sum of edge weights) in G. Q can take on values strictly less than 1, where positive values denote a larger number of edges within groups than by chance, and negative when there are less.

To find the optimal group assignment of nodes such that Q is maximized, we use a Louvain-like greedy method based on [129], the most common method of modularity maximization, due to its extension to multiplex networks [130] (described in Section 3.2.7) and its common use in network neuroscience [17, 131, 132, 133, 134, 135]. This is done by applying two steps iteratively.

1. We first aim to maximise local modularity. To do this, we assign each node in the network its own community. Then, for each node, it considers how removing that node from its own community, and adding it to one of the communities it is adjacent to, would result in the maximum positive change in Q. This is repeated iteratively until no individual movement of nodes results in an increase in Q.
2. A new network is built from the communities in step 1, where each community becomes a node, and connections between these newly constructed nodes are defined by the sum of weights between node communities.

Then, step 1 is applied to the network generated in step 2 and iterated until modularity is maximized (and Q is returned along with the group assignment of the nodes). It is important to note that this method of modularity maximization (for single and multiplex Louvain), among many others, results in some variation in Q for individual runs [136, 137]. This is due to a variety of factors such as those due to randomized seeding (the initial node community assignment). However, this can be combated by running the maximization process multiple times as is standard in prior literature [138, 139, 140]. Furthermore, the algorithm is only "Louvain-like" in the sense that it applies the same two steps iteratively as in the Louvain method, but operates on a generalized modularity matrix (as in Section 2.3.16) and so sacrifices some of the computational efficiency of the standard Louvain method for applicability to multiplex networks [130].

2.3.10 Network characteristics of the brain and AD

The healthy brain is commonly referred to as a small-world network, composed of integrated clusters, allowing for a balance of efficient local and global processing [141]. More formally, small-world networks are defined as networks with significantly more clustering than random networks while maintaining approximately the same characteristic path length as them [103]. In network neuroscience, studies consistently find small-worldness, high efficiency (low path length), modularity (segregated communities of densely interconnected regions), and network hubs (high-degree) as conserved features of brain networks [142]. In addition, these network hubs have a tendency to be more densely connected amongst themselves than to nodes of lower degree – forming a *rich-club* organization [120]. This rich-club organization suggests that hubs in the human connectome act as a strongly interlinked collective, perhaps improving information transfer and allowing for greater robustness to hub failure. It should be noted that small-world and rich-club organization is present in structural and functional networks of the human brain [143, 120, 144].

The organization of the human brain is often described at three scales – local (nodes), meso (communities), and global (whole network) scale [13]. In the context of network neuroscience, the local scale is that of individual brain regions, mesoscale are that of sub-networks, and global scale is whole brain network topology. Previously, we discussed how mesoscale sub-networks, such as the DMN, provide key insights into fundamental processes of the human brain such as cognition and emotion. In healthy humans, measures of brain network topology also yield insights at local and global scales. For instance, higher global efficiency (shorter path length) strongly predicted higher IQ in rs-fMRI [145], while local hubs (with higher node degree) correlate with complex task performance [146, 120].

When the brain is damaged due to disease or otherwise, network measures can capture the local, meso, and global scale changes in function and structure. In fact, AD is often characterized as a disconnection syndrome primarily due to its effect on brain networks [147]. As AD progresses, changes in functional brain activity and structural networks have been associated with lower brain efficiency and reduced connectivity between brain sub-networks [148, 149, 150, 151, 152]. In addition, modularity has been shown to increase along the disease spectrum of AD [20]. This resting-state fMRI (rs-fMRI) study found that changes in key network metrics, and prominently modularity, indicate a reduced ability to integrate information distributed across brain regions and in-between module communication as a result of AD. In addition, modularity was highlighted as a more sensitive network measure to MCI and AD than other more frequently used measures like clustering coefficient and path length [20]. It is important to note that while modularity is sensitive to AD progression, it is limited as a global measure representing how segregated the network is. Quantifying to what extent individual ROIs play a role in modular network organization is not fully understood.

It should also be noted that while brain networks often exhibit small-world structure, this can coexist with other diverse organizational structures (such as hierarchical modular networks) and possess dynamic features [153]. Furthermore, brain networks are not static, but dynamically change in time [17]. Additionally, interactions between structure and function, or frequency bands in brain networks add additional complexity in understanding brain organization [28]. This motivates the development of novel models to capture the dynamic nature of brain networks.

2.3.11 Multi-layer networks

With the advent of multi-scale, multi-modal, and spatio-temporal datasets of the human brain, multi-layer networks have gained popularity [154]. While many methods of multi-layer construction exist, such as temporal networks, a typical multi-layer network is achieved through the linking of many individual networks (layers) to measure the interactions between them [102]. For example, in a social network, each layer could be used to separate types of relationships such as friendship, colleagues, kinship, etc. with inter-layer (between layer) edges denoting a person who falls under multiple relationship types such as a colleague and a friend. In neuroimaging, layers can encode individual aspects of the data such as time or frequency band, and/or each layer representing an imaging modality [28]. The benefit of such a network construction is the ability to apply generalized graph theoretical algorithms, such as multi-layer modularity, to explore interactions between layers or how the brain dynamically organizes itself in time [28]. These models have been used in a variety of studies, providing insight and improved performance in the classification of AD subjects, of biomarkers for epilepsy, and many other results in areas ranging from economics to ecology [28, 155, 102].

2.3.12 Formal definition of multi-layer networks

We formally define a *multi-layer network* as a pair $\mathscr{M} = (\mathscr{G}, \mathscr{C})$ where $\mathscr{G} = \{G_s; s \in \{1, ..., M\}\}$ is a family of graphs $G_s = (V_s, E_s)$ (in our case weighted and undirected and also called the layers of $\mathscr{M}$) and $\mathscr{C} = \{E_{sr} \subseteq V_s \times V_r; s, r \in \{1, ..., M\}, s \neq r\}$ is the set of edges between nodes of different layers (called *inter-layer edges*) G_s and G_r with $s \neq r$. The edges in each layer of $\mathscr{M}$, E_s, are called the *intra-layer edges* of our multi-layer network. [102]. A *multiplex network* is a type of multi-layer network in which $V_1 = V_2 = ... = V_M = V$ (all layers have an equal number of nodes) and the only inter-layer connections occur among node replicas, i.e., $E_{sr} = \{\{v, v\}; v \in V\}$ for every $s, r \in \{1, ..., M\}, s \neq r$.

Multiplex networks lend themselves especially well to brain network modelling as we can consider the same set of nodes (areas of the brain), and choose each layer depending on other aspects such as time or frequency band [28]. In the case of time, a temporal network $(G(t))_{t=1}^{T}$ can be represented as a multiplex network with a set of layers $\{G_1, ..., G_T\}$ where

$G_t = G(t), E_{sr} = \emptyset$ if $r \neq s+1$, while $E_{s,s+1} = \{\{v,v\}; v \in V_s \cap V_{s+1}\}$. In other words, inter-layer connections exist sequentially in time and only when a node replica exists [28]. Note that this model is not limited to integer time as in the above definition. For example, multiplex frequency networks where layers are typically ordered from lowest frequency band to highest.

Next, we explore the extensions of the previously mentioned network measures to multiplex networks.

2.3.13 Multiplex degree

To maintain degree as a local measure, multiplex degree is often calculated on each layer separately so that nodal hubs can be tracked in time or otherwise. While some studies choose to define multiplex degree as an aggregated measure across network layers with various methods sacrificing layer specific understanding for simplicity or improving layer wise impact on the measure of degree [156], we keep the nodal definition of multiplex degree to stay aligned with the granular theme of this thesis. Thus, we maintain Eq. 2.1 and apply it to each individual layer to track degree in a multiplex network over indexed data such as time.

2.3.14 Multiplex clustering coefficient

For multiplex networks, clustering coefficient is defined differently. In this case, multiplex triangles are described across two layers, with two edges of the triangle existing in one layer and the remaining edge existing in the other (defined as a two-triangle). More formally, it is a measure of the ratio of the number of two-triangles and the number of one-triads (three connected nodes on one layer with two edges) for a node [156]. That is, for a multiplex graph G_s with $M \geq 2$ layers, the multiplex clustering coefficient for a node i ($C_{multiplex}(i)$) is defined as:

$$C_{multiplex}(i) = \frac{\sum_s \sum_{r \neq s} \sum_{j \neq i, m \neq i} A_{s_{ij}} A_{r_{jm}} A_{s_{mi}}}{(M-1) \sum_s k_{s_i}(k_{s_i}-1)} \tag{2.6}$$

2.3.15 Multiplex PageRank

In multiplex networks, the PageRank centrality of a node on one layer influences the centrality on another [124]. For instance, consider a dual-layer multiplex network. For network A, we evaluate PageRank $x = \{x_1, \ldots, x_N\}$ using Eq. 2.3 with dampening factor $\alpha_A > 0$. We then express the *multiplex PageRank centrality*, $X = \{X_1, \ldots, X_N\}$, of the vertices in network B with respect to the PageRank of network A (x), and vice versa.

Formally, we define the multiplex PageRank centrality X_i of node i as:

$$X_i = \alpha_B \sum_j x_j^{[\beta]} B_{ij} \frac{X_j}{G_j} + (1-\alpha_B) \frac{x_i^{[\beta]}}{N \langle x^{[\beta]} \rangle} \tag{2.7}$$

where $G_j = \sum_r B_{r_j} x_r^{\beta} + \delta\left(0, \sum_r B_{r_j} x_r^{\beta}\right)$, $\delta(a,b)$ is the Kronecker delta, $\alpha_B > 0$ is small enough to guarantee that the relation can be satisfied, and the exponents $\alpha, \gamma \geq 0$. α and γ control the influence of the layers on one another and lead to four important cases to consider in calculating multiplex PageRank [124]:

- Additive multiplex PageRank: $\beta = 0,\ \gamma = 1$ where the effect of network A on network B is the addition of centrality in B in proportion to how central they are in A.
- Multiplicative multiplex PageRank $\beta = 1,\ \gamma = 0$ where the effect of network A on network B is the multiplication of centrality in B in proportion to how central they are in A.
- Combined multiplex PageRank $\beta = 1,\ \gamma = 1$ where the effect of network A on network B is both additive and multiplicative.
- Neutral PageRank $\beta = 0,\ \gamma = 0$ where there is no effect of network A on network B and multiplex PageRank collapses into classical PageRank (Eq. 2.3).

This equation can be expanded to multiplex networks with more than two layers by calculating the first and last layers as in Eq. 2.7 and calculating middle layers with the average influence of the preceding and following layers.

2.3.16 Multiplex modularity

Typical community detection considers static single layer networks. However, it is also possible to consider these communities over indexed data, such as time, to see how these communities dynamically change and evolve. First, we formally define the extension of modularity to multiplex networks introduced by Mucha *et al.* [157], before discussing how it is maximized. Formally, the multislice, or multiplex modularity quality function ($Q_{multislice}$), is defined as:

$$Q_{multislice} = \frac{1}{2\mu} \sum_{ijsr} \left[(A_{s_{ij}} - \gamma_s \frac{k_{s_i} k_{s_j}}{2m_s} \delta_{sr}) + \delta_{ij} C_{sr_j} \right] \delta(g_{s_i}, g_{r_j}). \tag{2.8}$$

Like standard modularity in Eq. 2.5, multiplex modularity describes the observed number of edges existing within groups compared to if they were placed at random. Our random null model is now described for each layer s, $\frac{k_{s_i} k_{s_j}}{2m_s}$, but is now modified by the intra-layer resolution parameter, γ_s, which can modify the size of communities within each layer. Specifically, values of $\gamma_s > 1$ favour the detection of smaller, more fine-grained communities, while values of $\gamma_s < 1$ favour larger, coarser communities [158]. γ_s can also be adjusted independently per layer, allowing communities to be tuned to individual layer characteristics, which can be especially valuable when layers differ substantially in their density or connectivity structure. In most cases, γ_s is set to the default value of 1 for simplicity [157]. δ_{sr} and δ_{ij} facilitate the calculation of intra-layer and inter-layer edges separately. In this case, $(A_{s_{ij}} - \gamma_s \frac{k_{s_i} k_{s_j}}{2m_s} \delta_{sr})$ describes the multiplex version of the observed number of edges minus the expected number for intra-layer edges on each layer. In the case of inter-layer edges, these are handled by C_{sr_j} (inter-layer

coupling parameter) which is the weight of a node connected to itself across layers s and r. Typically, all inter-layer edges are equal and set to a default value of 1. The inter and intra-layer weights are included in the sum when nodes share group assignment (groups can exist both within and across layers), $\delta(g_{s_i}, g_{r_j})$, and multiplied by $\frac{1}{2\mu}$ where

$$\mu = \frac{1}{2}\sum_{jr} k_{jr} \tag{2.9}$$

which comes from the steady-state probability distribution used to obtain the multislice null model, detailed here [157].

The aim is to maximize our multiplex modularity quality function which partitions our network into sets of disjoint nodes. In the following, multiplex maximum modularity will be defined under three conditions [137]:

- Nodes are inter-layer coupled only when they are the same entity (composing a multiplex network).
- The network layers are ordinal (inter-layer edges exist only for consecutive layers).
- Inter-layer connections are uniform (they have the same weight).

Further definitions that are needed are the following: we denote $\mathscr{T} = \{A_1, ..., A_{|\mathscr{T}|}\}$ as a sequence of adjacency matrices (layers). In this case, the multiplex network is defined on the set of nodes $\{1_1, ..., N_1; 1_2, ..., N_2; ...; 1_{|\mathscr{T}|}, ..., N_{|\mathscr{T}|}\}$. Furthermore, we refer to the inter-layer edge weight by $w \in \mathbb{R}$ with $w \geq 0$. We define a partition $C \in \mathscr{C}$ of the network into K sets of nodes $\{C_1, ..., C_K\}$ where $\mathscr{C}$ is the set of all possible N-node network partitions. We define the partition matrix $S \in \{0,1\}^{N \times K}$ as $S_{ij} = \delta(c_i, j)$ where δ is the Kronecker delta function with $j \in \{1, ..., K\}$ and $c_i = j$ means that node i lies in C_j. Lastly, we define the multi-layer modularity matrix:

$$\mathscr{B} = \begin{bmatrix} B_1 & wI & 0 & \cdots & 0 \\ wI & \ddots & \ddots & \ddots & \vdots \\ 0 & \ddots & \ddots & \ddots & 0 \\ \vdots & \ddots & \ddots & \ddots & wI \\ 0 & \cdots & 0 & wI & B_{|\mathscr{T}|} \end{bmatrix}$$

where B_s is a single-layer modularity matrix computed on layer s, $B_{s_{ij}}$ denotes the (i, j)th entry of B_s, and I is the identity matrix. We now define the multiplex modularity maximization method as follows [137]:

$$\max_{C \in \mathscr{C}} \left[\sum_{s=1}^{|\mathscr{T}|} \sum_{i,j=1}^{N} B_{s_{ij}} \delta(c_{s_i}, c_{s_j}) + 2w \sum_{s=1}^{|\mathscr{T}|} \sum_{i=1}^{N} \delta(c_{s_i}, c_{s+1_j}) \right]. \tag{2.10}$$

It then follows that the Louvain method described in section 2.3.9 can be adapted to multiplex models by using the multiplex modularity matrix $\mathscr{B}$ as input instead of the single-layer counterpart. This general Louvain method of modularity maximization has been made publicly available at [130]. It should be noted that current measures of classical and multiplex modularity are limited as a global measure of network segregation and group assignment. It is currently unknown to what extent individual nodes contribute to these measures.

2.3.17 Multiplex networks and their applications

Recent work has shown that multiplex models of the brain can reveal distinct relationships inaccessible in single-layer analyses. For instance, [159, 155] use dual layer DTI and fMRI networks to analyse multi-layer motifs in healthy individuals at rest, epilepsy disease progression, or in one case a tri-layer set up with DWI, MEG, and fMRI in the analysis of AD [160]. Multi-modal applications of multiplex, frequency-based, network constructions show that each low-frequency band carries unique topological information and that multiplex-derived hubs differ from those in conventional single-band networks [161]. These multiplex hubs have been shown to be impacted by AD. For example, in studies of multiplex frequency networks of MEG, AD networks showed a selective breakdown of multiplex inter-frequency hubs in key ROIs and sub-networks even when single-band networks did not indicate such losses [162, 163]. Lastly, temporal networks are an important approach in the analysis of imaging data. They allow us to explore the temporal evolution of our data, such as the role of each brain region in relation to the overall functional system.

While various network analyses techniques, such as measures of modularity, centrality, and influence, can be determined in a single-layer model, a temporal multilayer model insures the continuity of these measures over time [28]. For example, using aspects of modularity for a multiplex temporal model with fMRI, it has been shown that the functional connectivity of the brain during learning is inhomogeneous [17]. The brain is instead organized into communities which perform unique functions. In time, nodes in these communities show varying allegiance, showing high flexibility (frequency of group changes) in some areas and low in others. In the study, the amount of flexibility could be used to predict the participants ability to learn, an indication of the utility of using multiplex measures to explore brain function [17]. In a single-layer analysis of the functional connectivity of AD, changes in community structure of the brain show disturbances in brain functional systems from healthy to MCI to AD [27]. Their research focused on the interaction between the frontalparietal (FP) and DMN networks, where functional connectivity differences within and between them become less segregated and more intertwined as AD progressed [27]. This is important, as the interactions between these two networks are highly correlated with complex cognitive tasks. Furthermore, disruptions in the dynamic interactions between regional networks in the brain are linked to lapses in attention and lowered performance in otherwise healthy individuals [164, 165, 166]. As such,

it is natural to question how modelling the dynamic temporal changes in brain organization for AD, elicited by complex tasks such as the VSTMBT, improve our understanding of the disease. The VSTMBT has been explored in networks constructed from EEG data [51, 69], but has yet to be explored in fMRI-based networks.

It is important to note here the natural construction of multiplex networks for task-based data. Brain networks can be broken up into equal intervals of time, such as in [131], or where each network represents a task phase. Furthermore, the weighting of edges in a multiplex network requires careful consideration as they are a determining factor in the formation of communities. While the weighting of intralayer connections typically follow from the data used (correlation strength of the BOLD-signal for fMRI, FA for DTI), weighted inter-layer connections in time pose a different challenge. Typically, the inter-layer weight is a free parameter, chosen as constant, and adjusted in accordance to the data [161, 131].

2.3.18 Network-based Simulations of Alzheimer's Disease

Previously, we have shown that many key network measures change as AD progresses. Thus, it becomes natural to question how these topological changes can be predicted. In functional brain networks, simulations of AD progression typically follow through the manipulation of healthy brain networks to mimic disease. These network manipulations can be focused on damaging connectivity involving key brain regions (targeted attack methods) and then compared to random attack models as a benchmark. For example, in [125], targeted attacks and random failure models are explored to describe the progression of the disease over time in MEG. These targeted and random attack models selectively or randomly reduced the edge weights between nodes in the network to simulate damage. They found that targeted attacks, specifically around highly connected nodes, provided the best results in simulating the progression of AD when comparing the approaches. Not only this, but they observed a shift from small-world topology to more closely resemble a random network suggesting a vulnerability of healthy brains to hub attacks, and lowered brain network resilience in AD. This effect was similarly seen in an attack model of AD in rs-fMRI [167]. This model used a similar method of targeting hub nodes, but where random edges were added to the network to increase the loss of small-worldness. Attacks on hubs in rs-fMRI data also describe the loss of global connectivity that occurs in the stages of autosomal dominant AD (a genetic variant of the disease) [168].

Reduced small-world topology and lowered resilience is also observed in structural brain networks. [169] tested the robustness of structural networks against targeted and random attacks through the removal of nodes and edges. Rather than simulating AD networks from healthy subjects, as in the previous studies of functional networks, they tested the robustness of both the healthy and AD networks separately and explored their topological changes in response to these attacks. They found that while AD networks were about as robust to random

failures as the healthy networks, that they were considerably more vulnerable to targeted attacks. Additionally, simulations of targeted and random attacks in healthy DTI networks targeting rich-club connections resulted in a significant reduction in network efficiency as opposed to random or random attacks against non rich-club hubs [120]. While only healthy networks were explored in this study, reduction in rich-club organization and global efficiency have been observed in AD as previously discussed in Section 2.3.10.

In sum, these simulation-based approaches are valuable for understanding the high-level mechanisms of AD. Simulation models of AD may be used to test how network decline may be slowed by identifying critical nodes and connections whose preservation could maintain cognitive function, guiding hypotheses for clinical intervention and early diagnosis. Additionally, as AD phenotyping improves [41], simulation models may be able to assist in understanding topological fingerprints in the disease continuum. However, research is needed to refine simulation models of AD as better methods of targeting (such as more accurate measures of centrality) become available, and our understanding of topological changes due to AD improves.

2.4 Conclusions

As populations around the globe live longer, AD presents a significant threat due to its progressive impact on brain function. These changes in brain structure and function can be captured by neuroimaging methods, allowing for the development of disease biomarkers. In this chapter, we explored how single and multiplex networks can be used to model changes in neuroimaging data, where network metrics quantified topological changes due to disease or could be used to simulate its progression. However, a key metric sensitive to AD progression, modularity, lacks granularity, fMRI network-based modelling has not been applied to a cognitive biomarker of AD (VSTMBT), and simulation models of AD progression require refinement to more closely match the topological changes occurring due to AD. The following chapters aim to address these gaps to improve our understanding and predict AD progression, and contribute network metrics and models which are broadly applicable across disciplines.

Chapter 3

Multiplex Nodal Modularity: A novel network metric for the regional analysis of amnestic mild cognitive impairment during a working memory binding task

This chapter's contributions have been published in PLOS One [30].

3.1 Introduction

Alzheimer's disease (AD) often progresses from mild cognitive impairment (MCI), where the amnestic (memory-related) subtype (aMCI) is often considered a prodromal stage [4, 5]. While the combination of biological biomarkers, neuropsychological tests, and genetic risk markers can describe the progression from MCI to AD with high accuracy [9, 10], methods with higher specificity which describe how individual regions of the brain drive this change are needed. This motivates the development of novel biomarkers for the early-stages of AD, where less damage has been done.

One such neurocognitive biomarker is the Visual Short-Term Memory Binding Task (VSTMBT), introduced by Parra *et al.* [29]. The VSTMBT targets visual memory binding deficits that occur in MCI and AD, and specific to AD opposed to non-AD dementias [66]. Using neuroimaging methods such as functional magnetic resonance imaging (fMRI) or electroencephalography (EEG), the dynamics in brain activity during a cognitive task, such as the VSTMBT, can be measured. As AD progresses, changes in functional brain activity have been associated with lower brain efficiency and reduced functional connectivity between brain subnetworks, leading to the naming of AD as a disconnection syndrome [148, 149, 150]. This

has been further explored in measures of white-matter density and microstructure, measured using Diffusion Tensor Imaging (DTI) [170]. For instance, in [149], white matter structures in the frontal and temporal lobes were found to be vulnerable in early-stage damage caused by familial AD with associated impairments in memory-binding.

More recently, brain networks have been extended to multiplex networks in order to capture additional complexity. Multiplex brain networks can be modelled with each layer representing windows of time in an fMRI scan or individual frequency bands in EEG [28]. In this way, multiplex networks have revealed insights into how the brain reorganizes itself in time during a learning task [17], modelled the cross-frequency dynamics of brain networks [171], and explored its structure-function relationship [159].

Methods which model functional and structural connectivity are important as brain networks are not random but organized and efficient at both local and global scales [11, 12, 13]. To capture the complex interactions between brain regions, their topology, and how these networks dynamically change and reorganize in time, community detection algorithms are employed [156]. The aim of such approaches (such as modularity maximization) is to segregate the network into communities or modules (groups of nodes), where connections within modules are more dense, to describe the underlying organization of the system. Modularity has been explored extensively for many single-layer biological networks, and in how these evolve and adapt due to age or disease [15]. However, the extension of modularity from single to multiplex networks was only achieved recently, and thus has seen less study [157]. For single-layer networks, modularity has been shown to increase along the disease spectrum of AD [20]. This resting-state fMRI (rs-fMRI) study found that changes in key network metrics (prominently modularity) indicated a reduced ability to integrate information distributed across brain regions as a result of AD. In addition, modularity was highlighted as a more sensitive network measure to MCI and AD than other more frequently used measures such as clustering coefficient and path length [20].

A limitation of modularity in single and multiplex networks is that it has been exclusively studied at a *global* scale. It is not fully understood how individual regions of a network, such as the brain, change in modularity due to disease, cognitive task phase, or dynamically change in time. Parra *et al.* showed that not only did the VSTMBT require specific memory binding regions, but also interacting and/or overlapped brain Regions of Interest (ROIs) for object recognition [77]. While global measures of modularity could allow us insight into the overarching structure of the VSTMBT, it is the extent that these individual ROIs interact and work together that is not well understood. As such, we hypothesized that a novel extension of modularity to individual ROIs, and applied to a multiplex framework, would yield novel insights into the regional modularity of the VSTMBT and how an ROI's contribution to modularity changes as a result of AD. Please see A.1 for the code and data availability for this study.

The contributions of this chapter are:

- Introduction of a novel measure of nodal group structure for both single-layer and multiplex networks called nodal modularity (nQ).
- Verification of nQ against other single-layer and multiplex measures of node influence.
- Application of nQ to multiplex networks of the VSTMBT-fMRI and single-layer DTI revealing that nQ characterizes a key transition stage of MCI to AD conversion.

3.2 Materials and methods

3.2.1 Participants

Participants were recruited from the Psychology Volunteer Panel at the University of Edinburgh, volunteers from the Scottish Dementia Clinical Research Network interest register, and referrals by old age psychiatrists based at the NHS Lothian and NHS Forth Valley. Eligibility followed from a variety of criteria such as an age over 55, no neurological or psychiatric diseases effecting cognitive function, and normal or corrected to normal vision [48].

MCI patients had to demonstrate the capacity to consent, were provided with an information sheet informing participants to the longitudinal nature and assessments involved, and signed a consent form prior to involvement in the study. Approval was obtained from the NHS Multi-Site Research Ethics Committee (reference number 06/MRE07/40) and was given approval by local NHS R&D offices (Lothian R&D: 2006/P/PSY/22 and Forth Valley: FV682). Please see additional details in [48]. Furthermore, access to this dataset for the research described in this paper was obtained from NHS Lothian under study number 2006/P/PSY/22 on 17/11/2021.

This longitudinal study assessed participants with a battery of neuropsychological tests commonly used to asses dementia, such as the Addenbrooke's Cognitive Examination Revised (ACE-R) and the Hopkins Verbal Learning Test Immediate Total and Delayed Recall, and a novel VSTMBT, grouping subjects into early Mild Cognitive Impairment (early MCI), MCI, and those who converted to Alzheimer's disease after a 2-year follow up (MCI converters). Further information on this dataset is available here [48].

From these subjects, a subset underwent fMRI (during which they performed the VSTMBT) and diffusion MRI (dMRI) scanning. Refer to Table 3.1 for those who met this criteria and passed pre-processing requirements detailed in the following fMRI and DTI sections. For insight into the neuropsychological tests completed and a statistical analysis of these variables between disease groups see A.9.

Table 3.1: Demographic variables of MCI patients and healthy controls at initial screening. After a 2-year follow up, 6 MCI subjects had converted to AD.

	MCI	**early MCI**	**Healthy Controls**
	$(N = 16)$	$(N = 7)$	$(N = 8)$
	$M \pm SD$	$M \pm SD$	$M \pm SD$
Age	74.81 ± 6.09	79.71 ± 5.82	79.5 ± 5.15
Years of Education	12.81 ± 3.54	16.57 ± 3.91	15.0 ± 3.54
Sex	9 men; 7 women	5 men; 2 women	2 men; 6 women

Note: N = number of subjects; M = mean; SD = standard deviation.
Anova results on Age: F(2,28) $= 2.62$, $p = .09$, $\eta^2 p = .15$
Anova results on YoE: F(2,28) $= 2.86$, $p = .07$, $\eta^2 p = .17$

3.2.2 Visual Short-Term Memory Binding Task

Two tasks were explored in our study using non-nameable shapes and non-nameable colours derived by Parra *et al*. [29]. We refer to the first task as *shape*, where only the shapes are presented to the subject. The second we call *binding*, where coloured shapes are presented to the subject. In both cases, the experimental procedure follows as in Fig. 3.1.

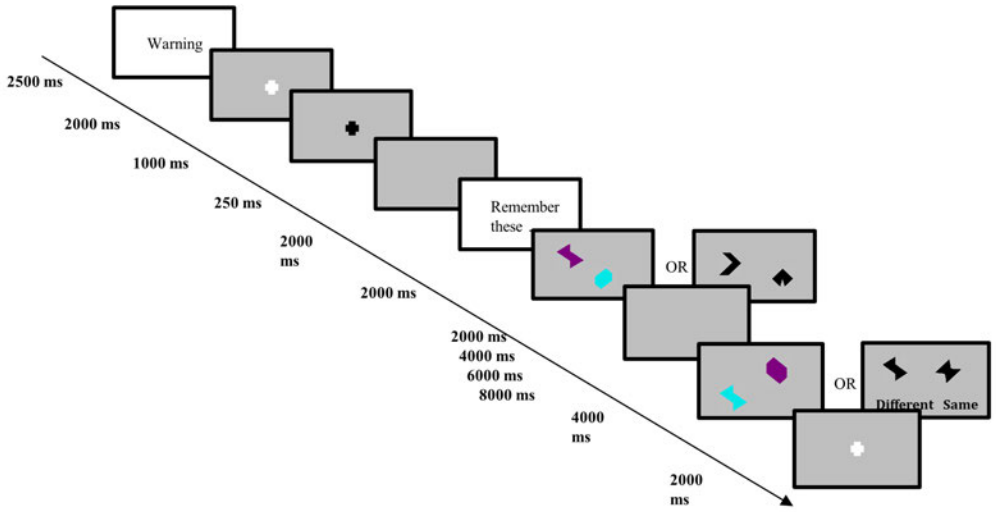

Figure 3.1: Task procedure. Trials were conducted as follows. A warning screen for 2500ms, a fixation period of 3000ms where a white cross turns from white to black, a blank grey screen for 250ms, a reminder of the instructions for 2000ms, the shapes or shapes with colours (depending on shape or binding task) are displayed for 2000ms (encoding phase), a blank grey screen is displayed for a variable time of (2000, 4000, 6000, or 8000ms) due to the fMRI design optimisation [77] (maintenance phase), a second set of shapes or shapes with colours are displayed for 4000ms (probe phase), and lastly an inter-trial interval of 2000ms. Repeat.

During the probe phase of the procedure, subjects would click a button in either their left or right hand indicating whether or not they believed that the new set of shapes/coloured shapes were different or the same (in 50% of the trials the new set of shapes/coloured shapes would be different). Trials in which the subjects made an incorrect choice were omitted from our analysis as they could stem from lack of engagement or attention. Correct trials were more consistent in capturing the underlying cognitive processes of the VSTMBT due to greater participation with the task itself.

3.2.3 DTI

dMRI data were collected at the University of Edinburgh Brain Research Imaging Centre through a GE Signa Horizon HDxt 1.5T clinical scanner: 3 T_2-weighted ($b = 0$s mm^{-2}) and sets of diffusion-weighted ($b = 1000$s mm^{-2}) single-shot spin echo-planar (EP) volumes acquired with diffusion gradients applied in 32 non-collinear directions. Subsequent volumes were acquired in the axial plane (field of view, fov $= 240 \times 240$mm; matrix $= 128 \times 128$; thickness $= 2.5$mm), giving voxel dimensions of $1.875 \times 1.875 \times 2.5$mm. The repetition and echo times were 13.75s and 78.4ms, respectively. In the same session, T_1-weighted inversion-recovery prepared, fast spoiled gradient-echo (FSPGR) volumes were acquired in the coronal plane with 160 contiguous slices and 1.3 mm^3 voxel dimensions.

To obtain a set of network nodes across the subjects, each T_1-weighted brain was parcellated into 85 ROIs with the Desikan-Killiany atlas' 34 cortical structures per hemisphere [172, 173] with additional regions added per hemisphere via sub-cortical segmentation: accumbens area, amygdala, caudate, hippocampus, pallidum, putamen, thalamus, ventral diencephalon, and the brainstem [118]. This volumetric segmentation and cortical reconstruction was performed with FreeSurfer v5.3.0 using default parameters. For further pre-processing detail please refer to Buchanan *et al*. [118].

Briefly, pre-processing was conducted with the FSL v6.0.1 toolkit. dMRI data underwent eddy current correction, diffusion tensors were fitted at each voxel and FA was estimated, skull stripping and brain extraction were performed, cross-modal nonlinear registration was used to align neuroanatomical ROIs to diffusion space, and the tractography was based on the probablistic method and white matter seeding approach as in [118].

Of note, the DTI weighted networks were constructed using the streamlines connecting each pair of the 85 grey matter ROIs. The weights of these edges were determined using the mean FA along the interconnecting streamlines [118].

3.2.4 Task-fMRI

fMRI data was collected during the same appointment, acquisition protocol and with the scanner outlined in the prior DTI section. Once localisation scanning was completed, a structural T1 weighted sequence was acquired (5 contiguous 5mm coronal slices; matrix $= 256 \times 160$; fov $= 240$mm; flip angle $8°$). During the VSTMBT, contiguous interleaved axial gradient EPI were collected alongside the intercommissural plane throughout two continuous runs (TR/TE $= 2000/40$ms; matrix $= 64 \times 64$; fov $= 240$mm; 27 slices per volume; thickness $= 3.5$mm; gap $= 1.5$mm). This yielded 9-minutes of scan in total, comprising 534 volumes (the first three volumes were discarded at the start of shape and binding trials). For clarity, this resulted in 267 volumes for each of the shape and binding tasks per subject.

Using SPM12, fMRI pre-processing follows as in [77]. Outlier detection was used to detect slices with a variance greater than 5 standard deviations [174]. Outlier slices were replaced by an averaged image of the previous and consecutive scans. These images were removed when constructing the network (0.75% of total scans). To account for movement, realignment of each fMRI image to the mean volume of the scan session through B-spline interpolation was done. Slice-timing correction was completed to account for differences in time when acquiring each voxel signal (temporal sync interpolation). Images were then coregistered to their structural T_1 images. Lastly, normalization to the MNI space was conducted using segmentation parameters and Diffeomorphic Anatomical Registration Through Exponentiated Lie Algebra (DARTEL) mapping functions [175, 176]. fMRI images were also visually inspected for noise and artefacts and subjects who did not pass inspection were removed from the study.

3.2.5 Functional network construction

We use the modified Desikan atlas obtained for each subject (as in the DTI section) to define ROIs and resampled to fit the voxel dimensions of the fMRI data. This was done with SPM12 using nearest-neighbour interpolation to ensure that voxel resizing maintained correct ROI mapping. These atlases were also visually inspected to check for proper fitting. For each ROI, the mean signal time-series was extracted from the fMRI images by taking the average signal across voxels defined by the ROI. This was repeated for each image and ROI across the 9-minute scan resulting in time-series of average brain activity at each of our 85 ROIs.

Next, we apply a 0.06Hz high-pass filter to the signals with a sampling rate of 0.5Hz to match our TR of 2s. This was done to account for fMRI signal drift in the very low frequency range [177], and the choice of 0.06Hz relates to the lowest frequency occurring for our longest task trial of 16s. We chose not to low-pass our signal given that, in some cases, our encoding/maintenance task phase is very fast, and thereby in close proximity to the signal's Nyquist frequency.

We define two task stages for our network construction – 'encmaint' and probe. We define encmaint as a combination of the encoding and maintenance phases of the task described earlier in Fig. 3.1. Due to an encoding phase and TR of 2s, this combination of the two phases improves our construction in two ways. It improves our measure of correlation between brain regions for network construction (higher number of samples) and additionally allows us to capture the peak of the haemodynamic response function (HRF) that occurs approximately 5s after stimuli onset (further details in A.2 and A.3). The probe phase, described in Fig. 3.1, is shifted forward 2s to decrease the overlap between encmaint and probe phases, improve the capture of peak HRF, while introducing minimal noise from the following inter trial interval.

After defining the task phase windows for each task (binding and shape), we reconstruct our time-series from the repetitions of task phases across the 31 trials. More specifically, the time-series for the probe phase is assembled from the windows corresponding to each probe phase within a trial, in sequential order. The same is done for the encmaint phase. From these time-series, we construct an 85×85 connectivity matrix for each task phase by calculating the Spearman correlation between each ROI pair.

Typically, studies of fMRI brain networks use Pearson correlation in the construction of connectivity matrices. However, it is expected that some noise and outliers may remain in fMRI data. These factors, along with additional pre-processing, task windows which could not be constructed perfectly due to inherent limitations of fMRI or the task itself, and other confounding factors such as those present due to the calculation of the mean time-series of regional data, made us select the more conservative Spearman's correlation for our analysis due to its robustness to outliers [178], and suitability for non-normally distributed data [179, 178]. We also acknowledge a recent study which discovered brain wide increases in functional connectivity with fMRI scan duration [180]. However, we expect this effect to be minor given that our analysis focuses on comparisons between subject groups (where this effect is ubiquitous) and reduced by randomized presentations of shape and binding tasks over the course of the scan.

To model the dynamics between the two task windows, we construct a dual-layer matrix from each of the two encmaint and probe matrices as in Fig. 3.2a. This is done by connecting each node in one layer to its spatial replica in the other via an edge. These edges are weighted equally and set to 1 as is standard in prior studies on multiplex brain networks [17, 159, 25]. The choice to use weighted graphs, rather than binary, was due to the preservation of the strength of functional association which is complementary to network organization [103].

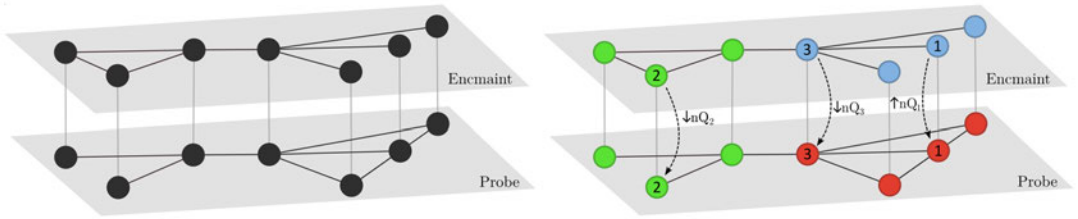

(a) Multiplex Network (b) Nodal Modularity

Figure 3.2: Multiplex network of the VSTMBT and nQ example. a) Networks for the two task phases of the VSTMBT, encmaint and probe, are constructed from the functional co-activations (correlation in time-series) between all pairs of ROIs. Spatial replicas are connected via an inter-layer edge, as seen in the above figure (light grey edges between the two layers), allowing for continuity of network topology in time. b) Here, multiplex nodal modularity (nQ) has been calculated for each node in our network as in Eq. (3.1) (refer to the following section). Each colour represents a separate module (obtained from standard multiplex modularity [157], where modules can exist within a layer (blue and red nodes) or across layers (green nodes). We note that values of nQ are influenced by, but not entirely dependent on, layer and module assignment. For instance, node 2 undergoes a decrease in nQ from the encmaint to probe layer due to a change in connectivity despite no change in module (green). On the other hand, node 1 undergoes an increase in nQ from the encmaint to probe layer due to increased connectivity within its module while also undergoing a change in module assignment (blue to green). While both node 1 and 2's changes in modularity are largely driven by changes in connectivity tied to that node, to illustrate how changes in module assignment influence nQ consider node 3. Node 3 undergoes no change in connectivity. However, it observes a decrease in nQ due to an increase in connectivity of node 1. While modularity in general has increased ($nQ_{1(blue)} + nQ_{3(blue)} < nQ_{1(red)} + nQ_{3(red)}$), the role of node 3 within its module has decreased. It is this interplay between connectivity, modules, and how these change across the layers of the network that influence each node's nodal contribution to classical multiplex modularity.

3.2.6 Nodal Modularity

Formally, we define $G = (V, E)$, as a *weighted undirected graph* composed of a finite set of *vertices*, $V = \{v_1, v_2, ..., v_n\}$, and a two element subset of V called *edges* $\{E \subseteq \{v_i, v_j\} | v_i, v_j \in V\}$ [104]. When a pair of vertices share a single edge $\{v_i, v_j\} \in E$, we say that the two vertices are *adjacent* to each other and that the edge is *incident* to each of our vertices. In addition, we define the *adjacency matrix*, A of our graph G, as the symmetric $(n \times n)$ matrix of all vertex pairs where entries $A_{ij} \neq 0$ if $\{v_i, v_j\} \in E$ and $A_{ij} = 0$ otherwise. Furthermore, we define a *multi-layer network* as a family of graphs $G_s = (X_s, E_s)$ (in our case weighted and undirected), also called layers, with $E = \{E_{sr} \subseteq X_s \times X_r; s, r \in \{1, ..., M\}, s \neq r\}$ as the set of connections between nodes of different layers G_s and G_r with $s \neq r$. The elements of each E_s are called the *intra-layer* (within layer) connections and the elements of each E_{sr} $(s \neq r)$ are called the *inter-layer* (between layer) connections [102]. A *multiplex network* is a type of multi-layer network in which $X_1 = X_2 = ... = X_M = X$ (all layers have an equal number of nodes) and the only inter-layer connections occur among node replicas, i.e., $E_{sr} = \{\{x, x\}; x \in X\}$ for

every $s,r \in \{1,...,M\}, s \neq r$. As a reminder, for this study, the entries of A_{ij} are defined by the correlation in fMRI signal time-series between all pairs of brain regions in the case of our functional networks. For our structural networks, entries of A_{ij} are defined by the mean FA of white matter between all pairs of brain regions.

In network neuroscience, community detection algorithms are often used to obtain a global measure of how modular the network is, how many modules there are, and in multiplex cases, the flexibility of each node (how often a node switches community through the layers of a network) [13]. However, aside from flexibility, the measure of modularity lacks granularity. The use of modularity as a global measure, while useful as a marker of whole brain changes due to disease, fails to capture to what extent these modular subsystems change in time, due to disease, or otherwise.

To tackle this, we extend the standard multislice (multiplex) modularity quality function, $\mathrm{Q}_{\mathrm{multislice}}$ [157], to individual nodes as in [181]:

$$Q_i = \frac{1}{2\mu}\sum_{jsr}[(A_{s_{ij}} - \gamma_s \frac{k_{s_i}k_{s_j}}{2m_s}\delta_{sr}) + \delta_{ij}C_{sr_j}]\delta(g_{s_i}, g_{r_j}). \tag{3.1}$$

More specifically, we use the multiplex version of modularity (refer to [157]) to calculate the optimized group assignment, g, a priori. It follows that, for a node v_i on our graph G, its nodal contribution to modularity (Q_i) is defined as follows. For all edges of node v_i that exist within the same group ($\delta(g_{s_i}, g_{r_j}) = 1$ when $g_{s_i} = g_{r_j}$) on layers s and r, we have the sum over all edge weights ($A_{s_{ij}}$) minus the expected edge weight if edges were placed at random ($\frac{k_{s_i}k_{s_j}}{2m_s}$). Here, k_{s_i} denotes the degree of v_i (the sum of edge weights incident to v_i) and m_s is the sum of all edge weights on layer s. γ_s is the standard intra-layer resolution parameter, which can modify the size of communities within each layer. In this paper, we set this to the default value of 1 [157] for simplicity. δ_{sr} and δ_{ij} facilitate the calculation of intra-layer and inter-layer edges separately. Thus, $(A_{s_{ij}} - \gamma_s \frac{k_{s_i}k_{s_j}}{2m_s}\delta_{sr})$ describes the multiplex version of the observed number of edges minus the expected number for intra-layer edges on each layer. In the case of inter-layer edges, these are handled by C_{sr_j} (inter-layer coupling parameter) which is the weight of a node connected to itself across layers s and r. Typically, all inter-layer edges are equal and set to a default value of 1. The inter and intra-layer weights are included in the sum when the nodes share the same group assignment (groups can exist both within and across layers), $\delta(g_{s_i}, g_{r_j})$, and multiplied by $\frac{1}{2\mu}$ which is defined in Eq. (2.9).

The modularity at each node, Q_i, can then be calculated using Eq. (3.1) with g as an optimized group assignment, defined a priori and discussed in the following section. In this way, we calculate each node's contribution to global multiplex modularity as

$$\mathrm{Q}_{\mathrm{multislice}} = \sum_i Q_i. \tag{3.2}$$

From now on, we refer to nodal modularity as $nQ_i = Q_i$, and note that nQ can just as easily be defined for single-layer networks. In this case, the expression for multiplex Q_i in Eq. (3.1) reduces to

$$Q_i = \frac{1}{2m}\sum_j [A_{ij} - \frac{k_i k_j}{2m}]\delta(g_i, g_j). \tag{3.3}$$

3.2.7 Modularity maximization

In this study, we determine the optimal group assignment g using the iterated version of the multiplex general Louvain algorithm [130] with default settings aside from 'moverandw', where a node moves to a new community when the probability of choosing that move is proportional to the increase in modularity that it results in. This setting helps to mitigate some of the undesirable behavior in ordinal multiplex networks discussed in [137]. The iterated version of the general Louvain algorithm was used to reduce some of the inherent variability in individual runs present in modularity maximization [136, 137], and is similar to consensus clustering [182]. Specifically, it uses the group assignment from the general Louvain method as the initial partition of each subsequent iteration of the algorithm. Convergence is reached once the general Louvain method's output group assignment has not changed between two successive iterations. Additionally, we further improve the stability of Q by performing multiple runs as is standard in the literature [138, 139, 140]. Furthermore, the networks in this study are both small and weighted, where issues in Q variability are much less severe [136]. It is of note that, while the Louvain method has been defined for both positive and signed networks [15], we choose to consider negative weights as equal to positive weights for modularity maximization. Negative weights have been argued to be neurobiologically relevant [15], but interpreting the differences between modules constructed from negative and positive weights separately is not well understood. We worried that per subject differences in the proportion of positive to negative weights could lead to large changes in modularity that would be difficult to interpret, especially for individual nodes. It is of note that, in all following mentions of maximised modularity, that we use the aforementioned iterated version of the algorithm with 100 repetitions, choosing the community assignment that corresponds with the highest modularity from those runs. For our data, we found modularity to be tightly distributed over each run.

3.2.8 Experimental setup

In this section, we outline the methodology used for studying nodal modularity, and how this measure interacts with the stages of disease in our functional and structural networks.

Modular behaviour of the VSTMBT

Initially, we verify the behaviour of modularity for the shape and binding tasks of the VSTMBT. To accomplish this, we compare the modularity (Q) of our shape and binding networks to random and Stochastic Block Model (SBM) surrogate networks. The aim of this experiment is to verify that the VSTMBT exhibits community structure better than random and that Q is similar or higher than a structured surrogate network (the SBM).

For this, we first construct our random networks by taking an edge in our network and randomly rewiring the edge using the Brain Connectivity Toolbox (BCT) [103]. Single-layer Q is then maximized on the randomized shape and binding networks. We also considered the SBM, a variation of the random graph above but with defined community structure. In essence, it takes a defined set of community labels, and a symmetric matrix defining the probability of connections existing between nodes and randomly constructs a network under these conditions [183]. Here, we construct the SBM with freely available code [184] from our shape and binding networks using the group assignment acquired from maximising Q on the non-surrogate networks. In this way we obtain structured, binary, surrogate networks from our shape and binding tasks. We then compare the modularity of our shape and binding networks against their surrogate counterparts to explore their modular behaviour.

Comparison of nQ with other nodal graph measures

To explore nQ as a measure, we compare it to several graph measures within three datasets. Specifically, we compare nQ against other measures of nodal community structure: single and multiplex versions of degree, clustering coefficient, and PageRank algorithms. Single-layer versions of these measures were calculated with the BCT. Multiplex versions of these measures are defined as follows. We calculate multiplex degree as standard, but with the addition of inter-layer edges. For the multiplex clustering coefficient, multiplex triangles are described across two layers, with 2 edges of the triangle existing in one layer and the remaining edge existing on the other (defined as a two-triangle). More formally, it is a measure of the ratio of the number of two-triangles and the number of one-triads (3 connected nodes on one layer with 2 edges) for a node. Refer to Eq. (22) in [156] for further information. For multiplex PageRank, the Pagerank centrality of a node on one layer influences the centrality on another. In brief, we choose to use the combined multiplex PageRank algorithm defined in [124], where centrality in one layer adds bias to both strategies 1 and 2 in calculating the PageRank centrality of a node in a separate layer.

For each of our tasks, binding and shape (for our controls), we construct a dual-layer network from the encmaint and probe phases. We maximize multiplex modularity using the previously mentioned iterated method and, using this community assignment, we calculate multiplex nQ at each node using Eq. (3.1). We then compare nQ to the other multiplex nodal measures of community structure, discussed above, and plot the per node scatter plots.

Next, we explore these comparisons for the two other publicly available datasets – the NKI-Rockland cohort and Zachary's Karate Club. See A.4 for more detail. For the neuroimaging data (NKI-RS), we construct multiplex, dual-layer, fMRI-DTI networks for each subject by connecting nodes in the fMRI network to their spatial replicas in the DTI network. We maximize $Q_{multiplex}$ and calculate nQ in the same way as discussed in the prior paragraph for our dataset, and compare nQ to the same graph measures.

For Zachary's Karate Club, we maximize the single-layer version of Q using the iterated version in [130]. We then calculate single-layer nQ (Eq. (3.3)) from the community assignment corresponding to the maximized Q in the previous step. Lastly, we compare the single-layer versions of degree, clustering coefficient, and PageRank to nQ.

Application of nQ to investigate local-scale changes in MCI

Here, we detail how comparisons are made between control and disease groups, single and multiplex network constructions, and binding and shape tasks to validate the utility of nQ in the characterisation of MCI.

For each of our subject groups (control, early MCI, MCI, and MCI converters), and for each of our shape (shape only) and binding tasks (coloured shapes), we explore single-layer encmaint and probe networks and their corresponding dual-layer network. Furthermore, we construct single-layer DTI networks for each subject.

For all of the above networks, we calculate nQ with the appropriate single or multiplex methods as described previously. We then compare the differences in nQ between control and disease for each network and task using two statistical tests: permutation test and receiver operating characteristic (ROC).

The permutation test is a method of hypothesis testing widely applicable to a variety of use cases [185]. In brief, given two sets of labelled data (such as control and disease), the permutation test computes the test statistic (in our case a two-sided test of the difference of means between the two samples) across many permutations of the labels of the two groups. For each permutation of the labels, we calculate the difference of means between the newly permuted groups and the difference of means for our original group. In total, our p-value is the proportion of sampled permutations where the absolute difference is different from the absolute value of our original observed difference in means. In our study, we calculate p-

values with 10000 permutations using code from [186]. The code also computes the effect size using Hedges' g, a bias-corrected version of Cohen's d measuring the standardized difference in means between two groups, which provides a less biased estimate of the effect size, particularly for small sample sizes [187].

The receiver operating characteristic (ROC) is a diagnostic measure of accuracy [188]. ROC plots are a measure of sensitivity vs. specificity, and typically, values of the area under the curve (AUC) generated this way is a measure between 0.5 (no apparent distributional difference between the two groups of test values) and 1 (perfect separation of the test values of the two groups).

We use the permutation test and ROC, for each of the models, to explore the effectiveness of nQ at categorizing the stages of disease in single vs. multiplex constructions and binding vs. shape tasks. We do this for each node in our network, comparing the values of nQ for healthy controls to each of our groups (early MCI, MCI, and MCI converters). That is, for each of the previously mentioned networks, we calculate permutation tests in the following way. For each node (brain region), we take the nQ calculated for each subject in the control group, compare the difference in means with the permutation test and the accuracy of the ROC in classifying disease and control groups to obtain the p-value, effect size, and area under the curve (AUC) of the ROC. Due to our small sample size, we take a conservative approach, reporting the regions where $p \leq 0.05$ and where p-values passed Benjamini-Hochberg false discovery rate (FDR) correction as regions exhibiting significant difference in nQ when comparing control and disease groups. FDR was conducted with the Multiple Testing Toolbox in Matlab [189] and visualizations of ROIs which passed this test and their statistical results are given as tables or visualized on a brain mesh using the BrainNet viewer [190].

FDR was used to control for the existence of potential false positives given our large number of statistical comparisons (85 in single-layer and 170 in dual-layer) [191], and plots of this correction for our results are given in A.5. This was applied to our p-values at a threshold of $\alpha = 0.2$, indicating that we accept up to 20% of our statistically significant results to be false positives. We note that a requirement for FDR to properly control false positives is independent or positively dependent comparisons. Given that nQ is a nodal measures of group structure (within module comparisons are expected to be positively correlated) and Q increases across the stages of AD, we expect this requirement to be met in the majority of cases. However, due to the complexity of biological networks and AD's effect on brain network reorganization, we cannot rule out the possibility of some negative dependencies between p-values and acknowledge this as a limitation of this study. Alternative methods to control false positives for multiple comparisons under arbitrary dependency are either inappropriate for this study [192],

or are known to be too conservative [193]. This is especially the case given that our small sample size limits the size of our p-values, limiting the effectiveness of applying conservative FDR approaches. However, [194] argues that discriminative power is more linked to effect size and variability than group size, motivating us to report the ROC AUC for completeness.

We perform a similar, per node analysis of our DTI data. Specifically, we explore nQ calculated on our single-layer FA-weighted DTI networks. We do the same group comparisons of control vs. disease with permutation test and ROC as in the previous section, reporting regions where $p \leq 0.05$ and where p-values survived FDR correction at $\alpha = 0.2$.

Lastly, we explore ROI changes in nQ for early MCI vs. MCI and MCI vs. MCI converters for our fMRI multiplex and DTI single-layer networks. This is done in the same manner as above by calculating the nQ for each of the ROIs in our networks, then comparing the differences in this measure with our statistical tests.

3.3 Results

In this Section, and following the methodologies described previously, we verify the behaviour of Q for our task-fMRI, perform nQ benchmarking, and apply this measure to our shape and binding task-fMRI and DTI to explore changes in nQ along the AD continuum.

3.3.1 Modular behaviour of the VSTMBT

Initially, we verify that Q behaves as expected for our shape and binding tasks. We compare Q in our shape and binding networks separately, and in random and SBM surrogate networks in Fig. 3.3. Each of the shape and binding networks exhibited a better modular structure than random and similar modularity to our SBM surrogate networks, as expected. This verifies that both the shape and binding tasks of the VSTMBT exhibit a modular structure. Of note is the slightly increased modularity in the SBM surrogate networks. This is likely due to the binary weighting of the surrogate networks leading to a more defined group structure. Regardless, the modularity of the fMRI and SBM surrogate networks, along with the significantly improved performance over the random networks, suggests that the functional networks constructed from the shape and binding tasks exhibited modular group structure as expected.

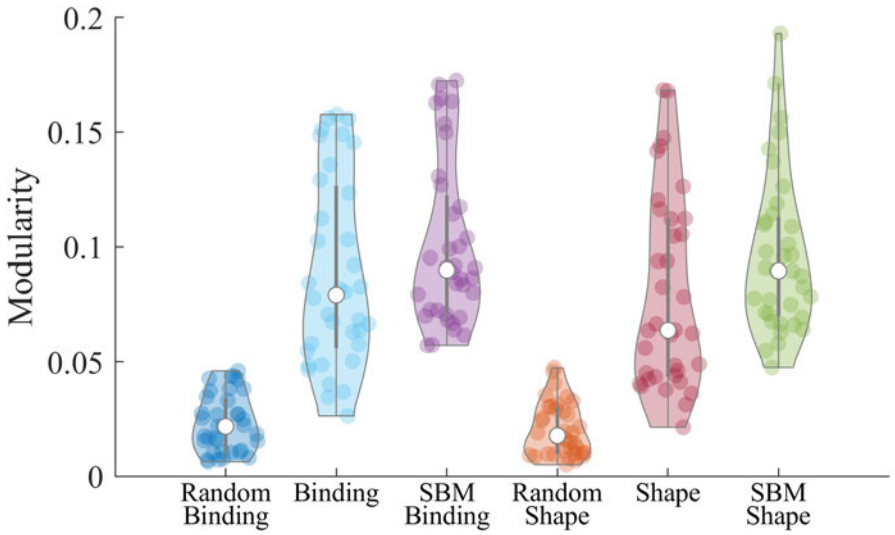

Figure 3.3: Random and SBM null models for comparisons of modularity in shape and binding tasks. Above are the violin plots of the modularity distribution for the shape and binding tasks. This is also explored for our random and SBM surrogate networks. Violin plots were generated with publicly available code [195].

3.3.2 Independence of nQ with other nodal graph measures

Next, we explore whether nQ captures distinct information compared to other nodal graph measures for our dual-layer fMRI data, for each of our tasks, and in two additional datasets, NKI-RS and Zachary's Karate Club.

For our dual-layer fMRI networks and our cognitively normal subjects, we find that, for the binding task, there are moderate negative correlations between nQ and degree and clustering coefficient (-0.54 and -0.6, respectively), and a slight negative correlation (-0.23) with PageRank as seen in Fig. 3.4. Interestingly, we observe clear boundaries in the degree and multiplex clustering coefficient comparisons. In the case of degree, we see a sloped lower bound, reflecting that modular importance is directly constrained by decreased connectivity leading to a lower number of within-module connections. For high-degree nodes, while they initially permit higher values of nQ through increases in within-group connectivity, highly connected nodes are more likely to span multiple modules, diluting their within-module connectivity which results in a reduction in nQ and leads to the upper left to lower right boundary observed. For the multiplex clustering coefficient, a higher value indicates stronger multiplex triangles between the encmaint and probes phases of the task. Similarly to degree, this initially permits higher nQ through an increase in within-module connectivity and limited by an increased degree which can yield a larger number of multiplex triangles but with diluted within-module connectivity. However, it is possible for a node to have both high nQ and multiplex clustering coefficient when two high nQ node replicas (across the two layers) have strong

within-module connectivity and similar connectivity patterns. As such, the result in Fig. 3.4 also reflects a differing modular organization driven by a difference in the functional demands of the encmaint and probe phases of the task. In the multiplex PageRank comparison, we no longer observe the sloped upper bounded behaviour of the previous two comparisons, but see a similar sloped lower bound. This is consistent with PageRank, where a higher nQ means increased within-module connectivity to nodes that are likely to be well-connected themselves, and thus lead to an increased PageRank. This lower bounded slope may be influenced by the additive and multiplicative nature of the multiplex PageRank algorithm, where the random walker's movements are biased in favour of nodes with high PageRank in the other layer.

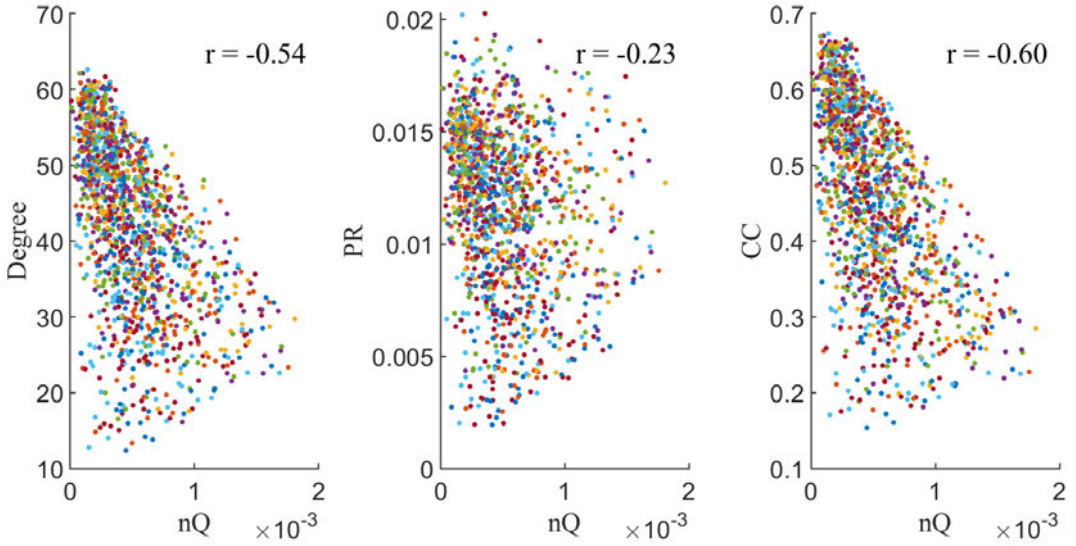

Figure 3.4: nQ vs. other graph measures. Scatter plots of Degree, PageRank (PR), and Clustering Coefficient (CC) vs. nQ. These measures were calculated in our dual-layer binding task-fMRI networks for cognitively normal subjects. The Pearson correlation between these comparisons is given by r.

In Zachary's Karate club, we find that single-layer nQ is strongly correlated with Degree and PageRank ($r = 0.77$ and $r = 0.78$ respectively), but not with Clustering Coefficient ($r = -0.27$) as seen in Fig. 3.5a. Since community structure in this network largely centres on the leaders of the two clubs, this could explain the similarity between the degree of a node and its nQ (contribution to group structure), while PageRank behaving similar to degree in this case could be a result of the network being fairly regular (each node in the network having a similar degree).

In NKI-RS, for the rs-fMRI and DTI dual-layer networks, we find a fairly strong correlation ($r = 0.69$) between nQ and degree, while close to no correlation ($r = 0.07$) in PageRank and a moderate negative correlation ($r = -0.53$) in Clustering Coefficient as seen in Fig. 3.5b. Here we see a similar triangular bounding as in the dual-layer fMRI networks. Specifically, where increases in degree can yield higher within-module connectivity, leading to an increase

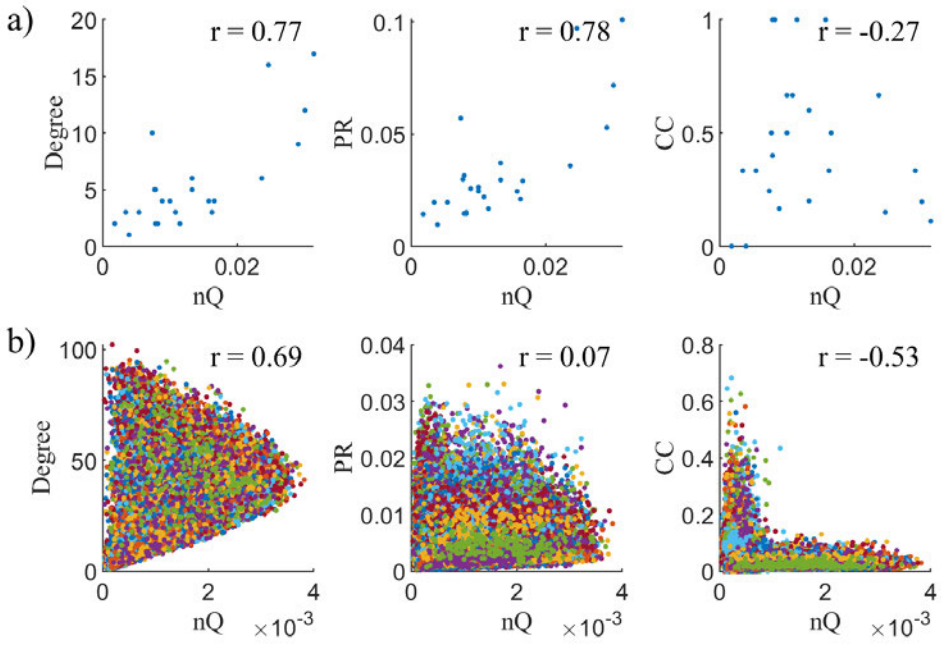

Figure 3.5: Behaviour of nQ in ZKC and NKI. Scatter plots of Degree, PageRank (PR), and Clustering Coefficient (CC) vs. nQ for Zachary's Karate club (a) and NKI-RS (b). r is the Pearson correlation coefficient.

in nQ, but only to a point where increases in degree would necessitate between-module connections and thus a decrease in nQ. In the case of multiplex clustering coefficient, we observe an L-shaped behaviour where high nQ nodes have low clustering coefficient and vice versa, reflecting the differences in modularity between rs-fMRI and DTI in this dataset. Specifically, the modularity of the DTI layer is much higher than the fMRI layer. Therefore, we would expect that the nodes that interact most with the DTI layer rather than the fMRI layer would result in the highest nQ. Since multiplex triangles require integration between both layers, a high multiplex clustering requires strong integration with the fMRI layer which could result in a decreased nQ. This is in contrast to a strongly connected node in the DTI layer with a weak connection to the fMRI layer resulting in high nQ and low multiplex clustering. This could explain the behaviour seen in CC vs. nQ in Fig. 3.5b. In the comparison to multiplex PageRank, we observe a decreasing upper bound, with no appreciable lower bound. This behaviour can be explained by the additive and multiplicative nature of the algorithm, as mentioned previously. Here, nodes with high nQ are strongly connected within communities which substantially differ across the two layers. This results in a reduced PageRank given that the biased jumps, influenced by the modular structure of the network, are poor locations for calculating PageRank on the other layer's substantially different topology. As nQ increases, this effect strengthens, leading to the observed upper bound on PageRank.

In sum, all three datasets (with single and dual-layer constructions), exhibited different relationships between nQ and the various graph measures. While not an exhaustive list, these tests, along with the formulation of nQ such that $\sum_i nQ_i = Q$, add reassurance to the independent and novel behaviour of nQ as a measure for exploring granular group structure in networks. Additionally, studies which calculate nQ either in binary single-layer networks or multiplex networks where layers contain a high difference in structure and/or network density should consider the potential overlap between the measures of node influence explored here. In these instances, computationally more efficient measures may be beneficial to prioritize while remaining similarly informative.

3.3.3 Application of nQ to explore local-scale changes in MCI

Here, we explore the changes in nQ across the stages of AD using the previously described permutation test and the area under the curve of the ROC, reporting regions that pass the thresholds of $p \leq 0.05$ and where p is FDR controlled at $\alpha = 0.2$.

fMRI

First we explore comparisons between controls and eMCI, MCI and MCI converters. We find that in single and multiplex constructions, for only the binding task and not shape, that the number of regions that exhibit statistically significant changes in nQ occur only for our comparisons between control vs. MCI converters (25 ROIs across encmaint and probe task phases exhibited abnormal nQ for multiplex, 20 ROIs for single-layer). See Fig. 3.6c for a visualization of these ROIs for the multiplex model and see A.6 for a comparison between single and multiplex models. For our multiplex binding model, we find moderately low p-values (range: [0.001 - 0.029]) and high effect sizes (range: [1.149 - 2.363]) and ROC AUC (range: [0.792 - 0.979]), see Table 3.2 for these results and A.7 for a visualization of select ROC plots. Note that since we are applying FDR at $\alpha = 0.2$ that up to 20% of our ROIs may be false positives (equating to 5 ROIs in the multiplex model and 4 ROIs in the single-layer case). Furthermore, given that no ROIs survived FDR correction for the shape task (for both single and multiplex models) and multiplex modelling resulted in improved performance, we focus on reporting fMRI results for the binding task as a multiplex network. Additionally, in our comparisons of eMCI vs. MCI and MCI vs. MCI converters for fMRI shape and binding, no p-values survived FDR correction.

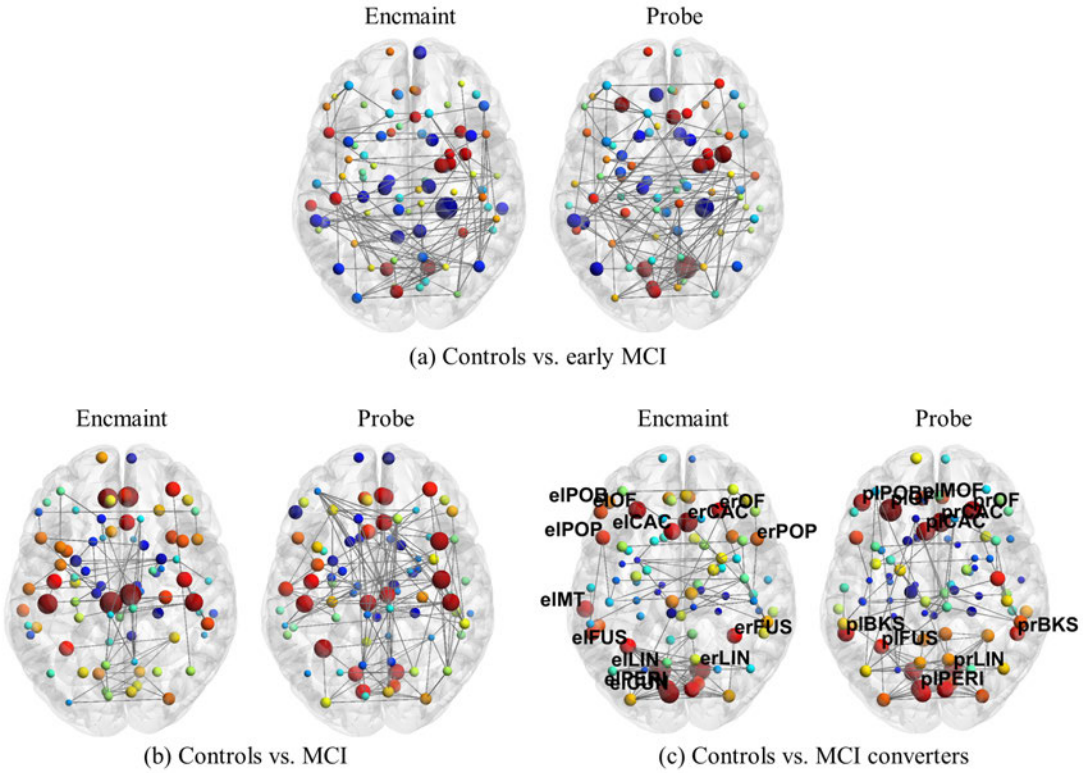

(a) Controls vs. early MCI

(b) Controls vs. MCI

(c) Controls vs. MCI converters

Figure 3.6: Changes in nQ for multiplex fMRI binding. Using BrainNet Viewer, we visualize encmaint and probe (left and right brain respectively) layers of our network. Here, nodes in blue represent loss of nQ while those in red represent gains in nQ. The size of the nodes represent the magnitude of this change, while labeled nodes are those that passed $p \leq 0.05$ and FDR controlled at $\alpha = 0.2$. Labels follow the form task phase (e or p), followed by brain hemisphere (l or r), then a shortened version of the ROI (i.e. LIN refers to the lingual). Refer to Table 3.2 for a more detailed breakdown of the ROIs present in this figure. Furthermore, only 1.5% of edges are visualized for clarity. Note the magnitude of the gains in nQ for the later stage disease comparisons.

Table 3.2: fMRI multiplex binding for controls vs. MCI converters. This table displays the ROIs which passed $p \leq 0.05$ and where p-values are controlled by FDR at $\alpha = 0.2$. These ROIs reside in either the encmaint (EM) or probe (P) layers of our multiplex network and in left (L) or right (R) hemispheres of the brain. Standard p-value and effect size is displayed following permutation test and the area under the curve (AUC) of the Receiver Operating Characteristic (ROC).

ROIs	p	effect size	ROC AUC
EM R-caudalanteriorcingulate	0.002	2.362	0.938
EM L-caudalanteriorcingulate	0.006	1.924	0.875
EM L-lingual	0.007	1.883	0.896
EM R-lingual	0.010	1.774	0.896
EM L-middletemporal	0.008	1.708	0.896
EM L-pericalcarine	0.012	1.659	0.854
EM R-parsopercularis	0.007	1.634	0.813
EM R-lateralorbitofrontal	0.006	1.624	0.875
EM L-parsorbitalis	0.010	1.614	0.875
EM L-cuneus	0.014	1.556	0.896
EM L-parsopercularis	0.016	1.483	0.833
EM L-fusiform	0.020	1.453	0.792
EM R-fusiform	0.029	1.394	0.813
EM L-lateralorbitofrontal	0.026	1.149	0.792
P R-caudalanteriorcingulate	0.001	2.363	0.979
P L-caudalanteriorcingulate	0.003	2.039	0.917
P L-bankssts	0.001	1.722	0.958
P L-lateralorbitofrontal	0.003	1.702	0.917
P R-lateralorbitofrontal	0.006	1.663	0.896
P L-parsorbitalis	0.002	1.64	0.938
P L-pericalcarine	0.012	1.626	0.833
P R-lingual	0.015	1.531	0.854
P L-fusiform	0.014	1.453	0.854
P L-medialorbitofrontal	0.026	1.444	0.813
P R-bankssts	0.027	1.382	0.833

DTI

Next we look at changes in white matter microstructure in our DTI networks for comparisons between controls and our disease groups. We find, like in our fMRI networks, that the largest number of ROIs that exhibit statistically significant changes in nQ occurs in our comparison of controls and MCI converters as expected (4 ROIs for controls vs. MCI converters and 2 ROIs for controls vs. MCI), shown visually in Fig. 3.7. These ROIs also exhibited moderately low p-values (range: [0.001 - 0.007]) and high effect sizes (range: [1.504 - 2.390]) and ROC AUC (range: [0.863 - 0.958]), as seen in Table 3.3.

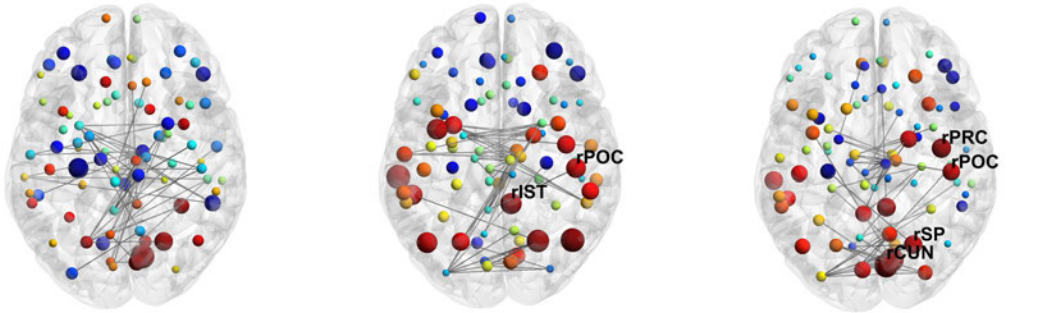

(a) Controls vs. early MCI (b) Controls vs. MCI (c) Controls vs. MCI converters

Figure 3.7: Changes in nQ for single-layer DTI. As before, blue indicates a loss of nQ while red represents a gain. Here we also see an increase (node size) in nQ for later stage disease comparisons. Furthermore, 1.5% of the network edges are displayed for clarity. Additionally, to reiterate, the DTI networks are constructed based on white matter microstructure. As such, we have a static (no temporal element like in the fMRI networks) single-layer network in this case where the single layer of the network is represented visually by one brain.

Table 3.3: DTI for control vs. disease. This table displays the ROIs which passed the thresholds of $p \leq 0.05$ and where the p-values were FDR controlled at $\alpha = 0.2$. L and R indicate the left or right hemispheres of the brain respectively. Standard p-value and effect size is displayed following permutation test and the area under the curve (AUC) of the Receiver Operating Characteristic (ROC).

Controls vs.	ROIs	p	effect size	ROC AUC
MCI	R-postcentral	0.004	1.637	0.863
	R-isthmuscingulate	0.003	1.539	0.888
MCI converters	R-cuneus	0.001	2.390	0.958
	R-precentral	0.001	2.046	0.958
	R-superiorparietal	0.002	1.730	0.938
	R-postcentral	0.007	1.504	0.875

Unlike our comparisons between early MCI vs. MCI for our fMRI models, we find that two ROIs pass our statistical thresholds for our DTI networks. Specifically, the right postcentral and precentral which were also observed in our prior comparisons of control vs. disease, see Fig. 3.8a. As before, these ROIs exhibited moderately low p-values and high effect sizes and ROC AUC, see A.8.

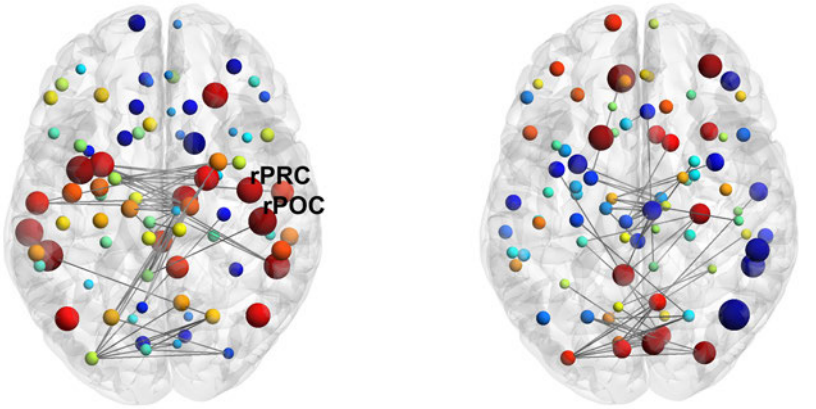

(a) early MCI vs. MCI (b) MCI vs. MCI converters

Figure 3.8: Comparisons of nQ for early MCI vs. MCI and MCI vs. MCI converters for single-layer DTI. Figure generation and details follow from Fig. 3.7. a) Here note the large (node size) increase (red nodes) in nQ in the parietal lobe.

3.4 Discussion

The following sections explore how nQ reflects aspects of neuropsychology, multiplexity, and neuroanatomy in AD.

3.4.1 Binding and Shape tasks

Parra *et al*. [29] found that when the demands of the tasks are adjusted to the capacity of the patients, the binding condition was highly sensitive to the disease, while the performance on the shape-only task did not change significantly between controls and familial AD. Our results strongly confirm this behaviour. We were unable to detect any statistically significant results for our shape task across all control and disease comparisons, while observing a high number of ROIs exhibiting abnormal nQ in the binding task for both the single-layer and multiplex models when comparing controls vs. MCI converters. These results indicate that nQ may be detecting binding task-specific changes in our brain networks at a crucial turning point of AD.

3.4.2 Single-layer vs. multiplex networks

We explored whether modelling the two task phases (encmaint and probe) as a multiplex temporal network yields a greater sensitivity to AD. We found that multiplex modelling resulted in a higher number of ROIs which pass our statistical thresholds (25 vs. 20 for single-layer), and showed generally improved p-values, effect sizes, and ROC AUC. This is in agreement with other multiplex temporal network studies which show that multiplex constructions yield insights beyond the analysis of each layer individually [17, 28, 25]. We expect that network

models of AD using nQ that were constructed with additional layers would see even more drastic differences when comparing single-layer and multiplex network constructions. However, the benefits of this approach and its connection to diseases such as AD require further study.

3.4.3 Neuroanatomical exploration of fMRI

Before exploring the neuroanatomical implications of our results, we first explore the interpretation of nQ in this setting. When considering nQ in the context of graph theory, an increase in nQ can indicate an increased involvement or specialization of a node within its own group and/or a reduction in between group connectivity. For the brain, this can be interpreted as a combination of reduced communication between brain subnetworks, and/or increased activity within key brain regions. Similarly, an increase in nQ in our DTI networks would reflect structural reorganization. Either an increase in white-matter microstructure between a specific ROI and those within its structural group, or a reduction in between group connectivity. When comparing healthy and impaired brain networks, these changes in nQ convey nodal aspects of functional and structural reorganization due to damage or disease. Such compensatory functional reorganization has been reported in the early stages of AD for both MRI [196] and EEG [69]. Additionally, many key sub-networks, like the default mode network, have shown to be key in understanding the brain at rest [110]. nQ could prove to be invaluable in understanding the role of individual ROIs both within and between their sub-networks.

Previously, we hypothesized that since Q has been shown to increase over the stages of AD in fMRI [20], that a more granular analysis of AD with nQ would uncover key insights into the individual stages of AD. Additionally, the binding task targets visual memory binding and the temporary retention of complex objects (coloured shapes in this case) and we hypothesized that key ROIs integral to these processes would be impacted, given that the VSTMBT is a cognitive biomarker of AD. Our results reflect this (see Fig. 3.6 and Table 3.2).

We observe extensive changes when comparing controls to MCI converters and explore the fine grain changes in nQ. Specifically, we find dysfunction centred in the limbic, paralimbic, and visual systems - lingual, caudal anterior cingulate, lateral orbitofrontal, fusiform, cuneus, pericalcarine, and medial orbitofrontal. These functional changes in nQ in the visual, limbic, and paralimbic systems comprise 18/25 (72%) of the ROIs identified. This suggests a potential increased activity in visual, limbic, and paralimbic systems and/or reduced communication between these subnetworks and others within the brain. These increases in nQ may be driven by impairments in brain wide communication between or within functional groups as compensation for performance deficits due to AD. Notably, these increases in the visual-memory system could reflect the diversion of functional resources away from hippocampal or entorhinal structures, regions critical to memory formation and impaired in AD [197, 198], as neighbouring ROIs within the system compensate for the resulting deficits in perform-

ance. Furthermore, the increases in nQ in the visual, limbic, and paralimbic systems are also common locations for the accumulation of tau and neurofibrillary tangles associated with Braak stages III-IV. Braak stages describe the sequential progression of Alzheimer's disease based on the regional spread of tau pathology in the brain, and it is at stages III-IV where MCI typically becomes observable [199]. Additionally, recent research in the VSTMBT suggests that the lingual, fusiform, middle temporal, and pericalcarine are areas of increased amyloid-β deposition in cognitively unimpaired adults with poor memory binding [71], creating a compelling connection between the VSTMBT and a common biomarker of AD. This is especially interesting given that these regions were all seen in the encmaint phase (where binding occurs), but not all in probe (missing the middle temporal, and cuneus) as expected. This connection between amyloid-β deposition and poor memory binding performance may explain some of the increased compensatory functional reorganization (reflected by increases in nQ) in these regions.

It should be noted that, while Braak staging is well described at a population level [200, 201], recent research suggests that there is variation at the individual level and that this trajectory appears to vary along at least four archetypes of tau spread in the brain [200]. We acknowledge this as a limitation and encourage the use of nQ in exploring AD sub-typing and connection to tau deposition in larger, multi-modal, datasets. Despite this, the connection between observed ROIs with classical tau deposition and amyloid-β remains encouraging. Additionally, it is important to highlight the stark difference when comparing the results from our comparisons of controls vs. MCI and controls vs. MCI converters (0 vs. 25 ROIs). The differentiation between subjects with MCI and those who will convert to AD (in this case after 2 years) is important both for understanding the disease and in its early detection before damage has been done. While limited by sample size, this stark contrast in our comparisons between controls vs. MCI and MCI converters warrant further exploration of nQ in larger datasets.

3.4.4 Neuroanatomic exploration of DTI

Similar to our fMRI results, we find that the number of ROIs that exhibited changes in nQ increased with disease severity (2 in control vs. MCI and 4 in control vs. MCI converters), including increases in effect sizes and decreases in p-values. DTI results were fairly distinct from fMRI aside from the cuneus which was identified when comparing controls vs. MCI converters in both modalities (however note the difference in laterality - left cuneus in fMRI and right cuneus in DTI). Interestingly, it is specifically the right cuneus that has been observed to have increased amyloid-β deposition among adults with poor memory binding, complimenting our fMRI results [71]. Additionally, [202] found that Braak staging was associated with reduced FA in many of the regions, and specifically in limbic pathways connecting the medial temporal lobe to subcortical grey matter and medial parietal lobes. Reduction in FA in pathways connecting

the medial temporal lobe to the parietal lobe could directly result in increased nQ in these regions, which we observed in the parietal lobe (post central and superior parietal). Such changes have been found in the brains of patients with MCI who are at the highest risk to progress to dementia. For example, Parra *et al*. [149], observed that white matter integrity of the frontal lobe in carriers of the mutation E280A of the PSEN-1 gene [203] correlated with performance when they were assessed with either an associative memory task (i.e., a form of relational binding in long-term memory, see [29] for details) or the VSTMBT. While we observed an increase in nQ in one frontal region (precentral gyrus), perhaps the most interesting finding is the laterality across our comparisons (all identified ROIs were in the right hemisphere). Parra *et al*. [149] observed that the genu of the corpus callosum accounted for VSTMB impairments and the hippocampal part of the cingulum bundle accounted for long-term memory binding deficits. The corpus callosum is often cited as an interface for cross-hemispheric communication in the brain, and damage to this structure could result in right dominant structural reorganization and reflected in our nQ results.

3.4.5 Conclusions

In neuroimaging, modularity has been largely limited by its use as a global metric. This is despite its utility in describing biological networks such as the brain, for which modularity is a core characteristic. Changes in modularity can be observed as the brain responds to task stimuli by dynamically reorganizing itself over time and when compensating for diseases such as AD [15, 20]. However, this reorganization is not yet fully understood.

To tackle this, we introduced nQ as a method to measure the specific contribution of an ROI to modularity. We explored this measure in the VSTMBT, which is known to require functional activity in specialized and distinct brain regions, along with communication between these regions, to drive cognitive functions such as encoding and retrieval in short-term memory binding [77]. We found that nQ captured the fine grain changes in visual, limbic, and paralimbic functional networks, and were in agreement with tau and amyloid-β deposition for poor memory binders. This trajectory was further supported in our DTI networks where results complimented previously understood changes in white matter integrity in poor memory binders in frontal and parietal lobes. Furthermore, nQ was able to distinctly differentiate two key stages of AD (MCI from MCI converters), encouraging further study of nQ as a potential diagnostic measure of AD. While limited by a small sample size, the results were consistent across hypotheses relating to single and multiplex constructions, DTI and fMRI, AD biomarker locations, and shape and binding tasks.

As changes in modularity are also observed in EEG and MEG [24, 22], future analyses of these granular changes using nQ could not only lead to a greater understanding of how functional reorganization occurs in AD, but have the potential in characterizing disease stages in a more widely available imaging modality (EEG). Additionally, given the wide spread use

of classical modularity in the research of real world networks, we expect nQ to improve these analyses by providing insight into local-scale group structure. For instance, in the exploration of granular group structure in protein-protein interaction, ecosystems, and many other biological networks [204], in understanding how individuals in static and dynamic interaction networks influence disease spread [205], or in improving the resilience of power grids by identifying vulnerable nodes to mitigate the impact of cascade failures [206].

In sum, the results of this research motivate further study of nQ in AD, network-based analyses of the VSTMBT, and the application of nQ to other diseases and networks beyond those biological to understand changes in modularity at local and mesoscales.

Chapter 4

Exploration of nQ and its variability in multiplex networks of EEG for a short-term memory binding task in MCI

4.1 Introduction

Previously, we introduced *nodal modularity* (nQ) as a method of quantifying granular contributions to community structure in networks. This was motivated by the understanding that biological networks, most notably the brain, display altered topological structure when injured. It was shown that modularity, when applied at a global brain level, is sensitive to the stages of Alzheimer's disease (AD) [20] and we hypothesized that an extension of modularity to individual nodes would provide novel insights into the progression of the disease. We found that nQ was sensitive to a key turning point of the disease (in differentiating mild cognitive impairment, MCI, from MCI converters). However, in this study we explored single and dual-layer networks only, due to the temporal resolution restrictions in functional magnetic resonance imaging (fMRI) and diffusion tensor imaging (DTI).

In network neuroscience, multiplex networks can range in size based on the number of nodes (typically determined by the choice of brain atlas) or number of layers (limited by the temporal or frequency resolution of the data). Atlases that parcellate on the scale of brain regions are popular choices for ROI-based analyses of the human brain [207]. Commonly used atlases include the 68 ROI Desikan-Killiany atlas [172], the 112 ROI Harvard-Oxford atlas (part of the FSL toolbox) [208, 209], and the 90 or 116 ROI versions of the Automated Anatomical Labelling atlas (AAL) [210]. While higher-resolution parcellations for the human brain exist [211, 207, 212], network-based studies of them remain rare with a systematic review finding that 25% of the studies used an atlas with 90 nodes (most commonly the AAL) with other parcellation sizes having less than 5% frequency [212]. For the number of network layers, studies which construct multiplex networks from neuroimaging data typically range

from multi-modal studies of two layers (i.e., exploring structure-function relationships) [159], 2-7 layers based on frequency band subdivisions (i.e., delta, theta, alpha1, alpha2, beta1, beta2, and gamma) [171, 162, 163, 213], or 2+ layers for temporal multiplex networks (where the upper limit is often determined by the temporal resolution) [17, 214, 215, 216]. For instance, Bassett *et al.* [17] explored the temporal dynamics of brain activity in fMRI during a learning task using multiplex networks with 112 ROIs and 25 layers. It should be noted that there are often limitations in temporal resolution in network neuroscience due to the modality (i.e., fMRI acquisition time) [75], disease of study (long scan times may present ethical concerns due to patient comfort) [217], and/or task of interest (task duration limits the number of temporal subdivisions). This leads to a reduced number of potential network layers in multiplex network studies with neuroimaging data.

One difficulty in exploring nodal values such as nQ in networks with a large number of nodes and layers is the number of values with which comparisons can be made. The complexity of these nodal relationships, along with the statistical risk of inflated false positives in the face of multiple comparisons, can lead to difficulties in deriving meaningful observations from the data. Typical approaches focus on the aggregation of network measures or edge weights across layers, but this can discard meaningful relationships between the constituents of the network [156]. However, careful methods of aggregation that capture variability of these relationships across layers, such as node flexibility which measures the rate at which a node changes group assignment across layers, can provide meaningful insights into the dynamics of brain topology [17]. In this chapter, we propose a novel metric, *collapsibility*, which quantifies the variability of nQ across the layers of a network and simplifies the study of nQ in large networks.

Thus far, nQ has only been explored in VSTMBT-fMRI and DTI data as in Chapter 3. However, MRI based datasets are both costly and have low temporal resolution. EEG is more affordable, widely available and has higher temporal resolution [50], allowing for the capture of faster dynamical changes in brain activity and facilitating the construction of multiplex networks with a greater number of layers.

In this chapter, we explored nQ and collapsibility in multiplex networks of the visual short term memory binding task (VSTMBT) in EEG data. This was done to determine whether changes in nQ in MCI were still expressed in EEG, thus facilitating larger studies of nQ in AD. We determine whether nQ remains robust and distinct (in comparison to other common measures of node influence) in multiplex networks with a greater number of nodes and layers. For these larger networks, we provide methodological considerations and definitions to improve interpretability. Furthermore, we explore nQ in VSTMBT-EEG data of MCI patients. Lastly, code used to compute collapsibility has been made publicly available at `https://github.com/AvalonC-C/Collapsibility`.

The contributions of this chapter are:

- Validation of nQ in a range of synthetic networks covering typical network constructions in neuroimaging and confirming that nQ maintains novel behaviour.
- Aggregation methods for nQ to simplify granular analyses of community structure in large multiplex networks.
- Application of these methods in VSTMBT-EEG data, revealing that nQ and a novel aggregate measure, *collapsibility*, are abnormal in MCI and reflect changes in grey matter and frequency markers of MCI and AD observed in other studies.

4.2 Materials and Methods

4.2.1 Exploration of nodal graph measures in larger surrogate networks

In this section, we describe the methodology used to explore the stability of nQ in large networks and introduce novel definitions of *collapsibility* as a method of quantifying nQ variability in multiplex networks.

Surrogate network construction

Surrogate networks to explore large multiplex networks typical of neuroimaging studies were achieved with a Stochastic Block Transition Model (SBTM) using freely available code [218, 184]. The SBTM is a method of constructing dynamic networks (i.e., for multiplex network construction) that is inspired by classical stochastic block models (SBM). In short, the SBTM is a method of exploring how group structure in networks evolves over time by modelling dynamical changes in edges and node group assignment over time. While other methods of constructing dynamic SBMs exists, such as the dynamic extension of the infinite relation model [219], they typically rely on hidden Markov-type approaches where it is assumed that network edges at different time points are independent. However, in many real-world examples such as social networks, edge probabilities at later time points are influenced by those at prior time points [218]. This can also be the case for brain networks constructed from EEG or fMRI data given that both modalities experience temporal autocorrelation [220, 221], and that some studies elect to use sliding windows in the construction of their multiplex networks [222].

To generate our SBTM surrogate networks, we construct networks across a wide range of network parameters:

1. Nodes: number of network nodes.
2. Layers: number of network layers.
3. Communities: number of communities.
4. p_{in}: percentage of edges existing between nodes within the same community in the first layer of the network.

5. p_{out}: percentage of edges existing between nodes of different communities in the first layer of the network.
6. $probNew$: probability of new edges forming within communities in the next layer.
7. $probExist$: probability of edges being retained within communities in the next layer.
8. $ClassChangeRate$: probability of a node switching group assignment across layers.

See Table 4.1 for details of the values explored for each parameter.

Table 4.1: Parameter Ranges for Surrogate Network Construction. All combinations of the following parameters were used to construct surrogate networks using the SBTM. Note that p_{in} and p_{out} are explored in tandem given that they together describe the proportion of edges that exist within communities vs. between communities.

Parameters	Range of Values
Nodes	60, 80, 100, 120, 140
Layers	2, 4, 8, 12, 20, 30
Communities	2, 4, 6, 8, 10
[p_{in}, p_{out}]	[0.9, 0.1], [0.1, 0.9], [0.75, 0.25], [0.25, 0.75]
$probNew$	0.1, 0.3, 0.7, 0.9
$probExist$	0.1, 0.3, 0.7, 0.9
$ClassChangeRate$	0.1, 0.3, 0.7, 0.9

Using these parameters, we generate SBTMs with the generateSbtm function in [184] where the inputs are the following:

1. Class: initial class assignment for layer 1 follows a standard block construction of equal group size, and the following layers have each node maintain that community assignment or change to a random community with probability $ClassChangeRate$ (iteratively for the number of layers).
2. $probInit$: this matrix of edge probabilities (communities X communities) was determined by p_{in} and p_{out} where p_{in} exists along the main diagonal (representing the probability of edges being within a community).
3. $probNew$ and $probExist$: these follow from the prior list of parameters and we maintain these probabilities uniformly for each generated layer. However, note that we explore some specific network constructions which change $probExist$ for different layer transitions to explore a simulated example of task-based network dynamics in Section 4.2.1.
4. Directed: this input is set to the default value of "false" to explore undirected SBTM networks.

We construct SBTM networks with the above inputs across all combinations of the parameters, and repeat this twice to reduce variability, yielding 153600 surrogate networks. These networks are used in the following sections to explore the behaviour of various nodal graph measures.

It should be noted that the inter-layer edges are uniformly set to 1 in the SBTM networks. Given that these networks are binary (edge weights are all 0 or 1), this means that the between and within layer edges carry the same influence on the calculation of our network measures. However, inter-layer edges have substantially less influence because they are far fewer in number than the intra-layer edges. While the number of inter-layer edges is fixed at $N(L-1)$ where N is the number of nodes and L are the number of layers, intra-layer edges depend on the initialized parameters of the network and fluctuate from layer to layer based on the combination of $probNew$, $probExist$ and $ClassChangeRate$. For the initial layer, the expected number of intra-layer edges is

$$E[\text{edges}] = c\frac{\frac{N}{c}(\frac{N}{c}-1)}{2}p_{in} + \left(\frac{N}{c}\right)^2\frac{c(c-1)}{2}p_{out} = \frac{N(\frac{N}{c}-1)}{2}p_{in} + \frac{N^2-\frac{N^2}{c}}{2}p_{out}$$

where c is the number of communities, and the coefficients of p_{in} and p_{out} represent the maximum possible within-community and between-community edges, respectively. Although substantial restructuring can occur in subsequent layers of the network that may reduce the number of intra-layer edges in individual layers, the expected number of intra-layer edges remains dominant, scaling as $O(LN^2)$ compared to the $O(LN)$ scaling of the inter-layer edges.

Network measures and methods of granular aggregation

In this section we explore several established network measures and provide novel definitions to assist in exploring aggregated values of nQ in large networks.

Specifically, we explore several known multiplex versions of node influence – degree, clustering coefficient, and PageRank. See Sections 2.3.13 - 2.3.16 for details. In addition, we use nQ (introduced in Section 3.2.6) and information on methods for maximizing modularity (Section 3.2.7). These measures are explored consistently and in a similar manner to methods used in Chapter 2.

Additionally, we introduce several novel definitions of *collapsibility* as an aggregation method to explore the variability of nQ in multiplex networks.

Definition 4.2.1 (Collapsibility)**.** For a multiplex network $G_s = (V_s, E_s)$ with layers $s, r \in \{1, ..., M\}$, we say that nQ is *collapsible* for the node replicas $\{(i,s),(i,r)\}$, with $s < r$ and $i \in V$, if

$$|nQ_{s_i} - nQ_{r_i}| < \varepsilon\overline{nQ_i},\ s \neq r,$$

where ε is defined as the *collapsibility threshold* and

$$\overline{nQ_i} = \frac{1}{M}\sum_{s=1}^{M} nQ_{s_i}.$$

We also define the *collapsibility index*, c_i, as the fraction of layer pairs that are collapsible for node i:

$$c_i = \frac{1}{\binom{M}{2}} \sum_{s<r} \delta_i, \quad \delta_i = \begin{cases} 1, & \text{if } |nQ_{s_i} - nQ_{r_i}| < \varepsilon \overline{nQ_i}, \\ 0, & \text{otherwise.} \end{cases}$$

Furthermore, the collapsibility of the entire network is defined as the mean across all nodes $C = \frac{1}{N}\sum_{i=1}^{N} c_i$. An example of collapsibility is given in Fig. 4.2.

Definition 4.2.2 (Totally collapsible)**.** When all layer pairs are collapsible for a node i, we say that nQ is *totally collapsible* across all node replicas i. That is, $\delta_i = 1$, $\forall s, r \in \{1, ..., M\}$, with $s < r$ and $i \in V$.

Definition 4.2.3 (Totally non-collapsible)**.** Where $|nQ_{s_i} - nQ_{r_j}| > \varepsilon n\bar{Q}_i$ for all pairs of layers s and r, we say that nQ at all node replicas i are *totally non-collapsible*. That is, $\delta_i = 0$, $\forall s, r \in \{1, ..., M\}$, with $s < r$ and $i \in V$.

The above definitions of collapsibility were inspired by the measure of *flexibility* in multiplex networks introduced by Bassett *et al.* [17].

Definition 4.2.4. The *flexibility* of a node f_i equates to the number of times that node changes group assignment across the layers of a multiplex network, normalized by the total number of consecutive layer pairs [17]. The flexibility of the overall network is defined as the mean flexibility over all nodes $F = \frac{1}{N}\sum_{i=1}^{N} f_i$ [17].

In this study, we explored flexibility in conjunction with collapsibility given that they are both derived from nodal group assignments obtained from the maximization of modularity. Where collapsibility is calculated based on the variability of nodal contributions to modular group structure, flexibility is calculated from the variability of modular group assignment. In this study we will explore the interactions between these two measures to test the extent in which collapsibility is similar to flexibility.

Verification of nQ and collapsibility

Previously, in Chapter 3, we compared nQ to other common measures of node influence in several datasets. While we found the behaviour of nQ to be unique for two dual-layer neuroimaging datasets and a single-layer social network, we also explore the behaviour of nQ in larger surrogate networks to determine, as network nodes and layers increase, whether nQ's behaviour remains unique.

For this purpose, we calculate multiplex clustering coefficient, degree, and PageRank in all 153600 surrogate networks as standard. We also calculate nQ as in Chapter 3 but now with 10 iterations for stability when performing modularity maximization. The reason for the reduction in iterations was due to limitations in computing speed when calculating modularity in a large number of surrogate networks with a high number of nodes and layers. However, given that these networks are binary, the variability in Q over each run was reduced and thus had a tight distribution.

For each network, we calculate Pearson correlation between nQ and clustering coefficient, PageRank, and degree, reporting the mean correlation as the number of nodes and layers in the surrogate networks increase. Additionally, we explore the cases where $r > |0.6|$ to determine what network parameters drive correlations between nQ and the other network measures. This threshold represents the lower range of "moderate" correlation and was chosen to assess trends in the parameters of the SBTM [223]. Additionally, we explore collapsibility for our networks for different collapsibility thresholds (ε) and compare them to standard flexibility as the size of the network increases. We then report on recommendations for picking ε.

Lastly, using insights from correlations between the graph measures above, we explore a variation of our surrogate networks that mimics task dynamics in functional brain networks. The purpose of this experiment was to question whether some of the high positive and negative correlations between nQ and the other graph measures were driven more by SBM block construction or by network parameters. This is achieved by changing the $probExist$ and $classChangeRate$ parameters every 3 layers to simulate periods of stability followed by a restructuring to mimic the interplay of stimuli and rest in task-based studies of fMRI and EEG.

4.2.2 Application to EEG

In this section we explore the application of nQ and collapsibility to VSTMBT-EEG multiplex networks.

Participants

The participants were those explored in this study [70] consisting of 215 subjects recruited from Southern Colombia and following “An Inclusive Approach to Recruitment in Underrepresented Populations” [70]. Participants had to pass strict inclusion criteria relating to physical and psychological health, alcohol/drug history, and had to have an MMSE $\geq$ 24. Subjects underwent screening with a battery of neuropsychological tests (see [70]) and EEG acquisition at the Universidad Surcolombiana and Universidad de la Amazonía in Southern Colombia. After accounting for any technical failures in EEG acquisition, 107 were Healthy Controls (HC) and 108 met the criteria for Mild Cognitive Impairment (MCI). See Table 4.2 for further detail.

Table 4.2: Demographic variables of healthy controls and MCI subjects. Note that this table was recreated from the table by Gonzalez-Montealegre *et al.* [70] which contains further information on the neuropsychological data. Furthermore, note the correlation in age and years of education between the healthy controls and MCI.

	All ($N = 215$)	**HC** ($N = 107$)	**MCI** ($N = 108$)	p **value**[a]
Age, years	60.9 (6.6)	59.5 (6.4)	62.2 (6.5)	0.002
Years of education	10.5 (6)	13 (5.6)	8 (5.4)	0.001
Gender (female)	79%	82.4%	75.7%	0.227[b]

Note: HC = healthy controls, MCI = mild cognitive impairment, N = number of subjects
a = Student's t-test
b = Chi-squared test

During the EEG session, participants completed the same VSTMBT as in Chapter 3, where shapes or coloured shapes are presented (encoding - 2000ms), must be remembered (maintenance - 1000ms), and the same or a new set of shapes/coloured shapes are presented (probe - 4000ms or until an answer) where the participant must determine whether the new set is the same or different, followed by an inter-trial interval of 1000ms. The analysis only considered trials with correct responses. Again, we refer to the shape only task as *shape* and the coloured shape task as *binding*. Of note, the experimental design consisted of a brief practice session for each condition followed by 100 test trials per condition (shape and binding).

EEG pre-processing

EEG data was recorded using 64 channels with ActiveTwo equipment (Biosemi, Amsterdam, The Netherlands), with two external electrodes for EOG (VEOL and HEOR). Signals were recorded at a sampling rate of 1024Hz, and EEG data was pre-processed using FASTER (version 1.2.4 [224]) and EEGLAB (version 2022.1). Signal pre-processing steps were as followed: the signal was filtered to 1-30Hz and down-sampled to 250Hz, ICA for oculormotor artifact removal (including visual inspection), epoched to -250 to 1300ms locked to stimulus onset (encoding and probe) with remaining artefactual epochs manually removed, and yielding waveforms for each individual and for each trial of the shape and binding tasks. For more detailed information see [70].

To improve spatial resolution, EEG source localization methods attempt to pinpoint the internal sources of these electrophysiological signals [94]. This is done through two stages, the forward problem and the inverse problem. To solve the forward problem, an approximation of the head (including aspects such as conductance) is modelled through various methods such as the finite or boundary element methods (FEM and BEM). To solve the inverse problem is to estimate the location of a greater number of sources than given electrodes causing it to be an ill-posed problem [225]. Several methods exist to solve these such as the minimum norm

method (MN) [226] and low resolution brain electromagnetic tomography (LORETA) [227], but note that while some newer methods (i.e., exact LORETA – eLORETA) have been developed for better localization of deep sources [225], spatial resolution and signal strength is still limited.

In this study, source space estimation was completed with EEGLAB (v2024.2.1) with the FieldTrip (Fieldtrip-lite v20240111) and dipfit (v5.5) plugins. For each of the subjects, tasks (shape and binding), and each of the two task phases (encoding and probe) the following is done: EEG electrodes are aligned to the standard 10-05 electrode positions using EEGLAB. We construct the source model using a grid with $4mm^3$ resolution and define the non-zero entries based on the Automated Anatomical Labelling atlas (AAL, and included in FieldTrip) warped to dipfit's standard MRI (Colin27 MRI). We then use this source model with the standard BEM head-model (included in dipfit) to calculate the lead field. The covariance matrix is calculated from the pre-stimulus data and used in the following step to compare post-stimulus source activity to baseline. Source space estimation is then achieved using the lead field and head models described previously, with exact low resolution brain electromagnetic tomography (eLORETA) for improved sub-cortical source estimation [225], as many of these regions are heavily impacted in AD (i.e., the hippocampus). Each trial's 3D virtual time series is reconstructed using the spatial filter calculated from the source space reconstruction multiplied by the raw time series. From the source estimation, power time series is calculated from the 3D moments as standard (the sum of the squared current moments). The AAL atlas is then interpolated (using the nearest-neighbour method) to match the dimensions of our source estimation and the time-series are averaged across atlas ROIs.

Network construction

To calculate functional connectivity, we use the source estimated activity from the pervious step to perform time-frequency analysis using the standard ft_freqanalysis function with the (multi-)tapered fast Fourier transform (mtmfft) method, with a single-taper (Hanning window) for each of the two task phases (encoding and probe) and the following frequency bands with 2Hz resolution – delta (2-4Hz), theta (4-8Hz), alpha (8-12Hz), and beta (12-30Hz). We then obtain the cross-spectral density and use this to calculate the de-biased weighted phase lag index (referred to as wPLI from here on) [107]. We used wPLI for its robustness to volume conduction, and the de-biased version to avoid potential positive or negative bias in the imaginary component of coherence [107]. In total, for each of our subjects and each task (shape and bind) we have 8 adjacency matrices representing wPLI connectivity between each of our 85 ROIs for encoding, probe, and the 4 frequency bands.

For each task (shape and binding) and task phase (encoding and probe), we construct multiplex frequency networks by connecting each ROI to their spatial replicas in consecutive frequency bands (as in Fig. 4.1). These edges are set to 1 as is standard in prior studies on multiplex brain networks [17, 159, 25].

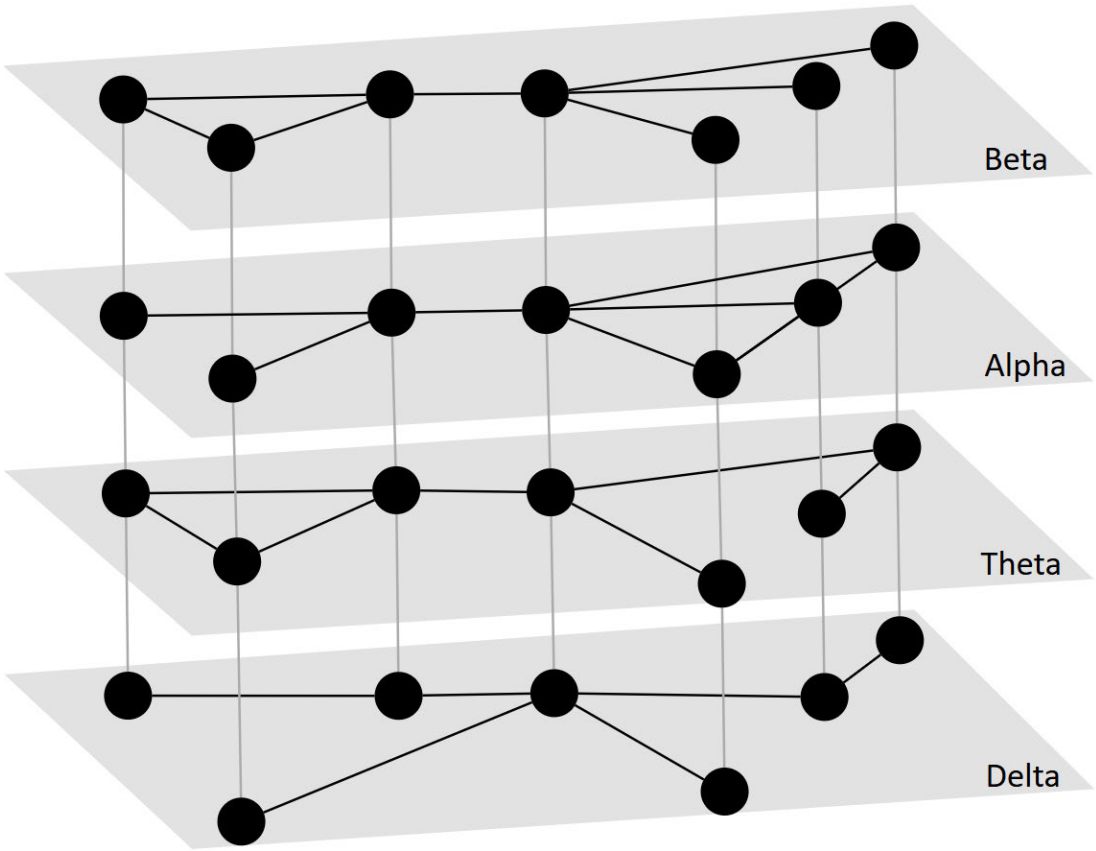

Figure 4.1: Multiplex frequency networks. Each layer of the network is composed of nodes (ROIs) and weighted edges determined by the wPLI between each pair of ROIs for a specific frequency band. These networks are connected to each other consecutively via inter-layer edges (light grey) that connect each ROI to itself in the following frequency band. This multiplex frequency network is constructed for each of our tasks (binding and shape) and each task phase (encoding and probe).

Experimental procedure

In this section, we outline the exploration of nQ, collapsibility, and flexibility in our multiplex frequency VSTMBT-EEG networks. For our healthy controls and MCI subjects, we calculate nQ, collapsibility, and flexibility for each of our multiplex frequency networks – encoding in binding, encoding in shape, probe in binding, and probe in shape. Note that modularity is maximized with 100 iterations for both the calculation of nQ and flexibility using Eq. 3.1 and Definition 4.2.4, and follows the methodology in Section 3.2.7 on modularity maximisation. However, note that wPLI is positive (range [0,1]), so no adjustment is needed to handle

negative edge weights as was needed in the prior chapter when exploring correlation-based networks of fMRI data. Collapsibility is calculated from our nQ values as in Definition 4.2.1, with a collapsibility threshold of 0.2 based on our surrogate network results in the following section. See Fig. 4.2 for a visualization of module assignment in multiplex networks and discussion of these measures.

We then compare our controls to MCI, for each ROI, using two statistical tests – permutation test and the Receiver Operating Characteristic (ROC). Note that p-values derived from the permutation test are controlled with the Benjamini-Hochberg false discovery rate (FDR) to control for false positives for multiple comparisons.

These methods are the same as those used in Section 3.2.8. In brief, we calculate the permutation test with 10000 permutations using publicly available code [186]. The p-value of the permutation test represents the proportion of sampled permutations where the absolute difference in means is different from our originally observed difference in means [185]. We apply FDR to these p-values to control for the potential for false positives in the data given the large number of statistical comparisons for each ROI in our networks (116 ROIs in collapsibility and flexibility as these values are calculated across the four layers of our network, and 464 ROIs for our nQ comparisons representing all nodes from each layer). FDR correction was performed with the Multiple Testing Toolbox in Matlab [189]. We apply FDR with a threshold of $\alpha = 0.2$ which corresponds to the acceptance of up to 20% of the statistically significant results ($p \leq 0.05$) as false positives. In addition, we calculate the area under the curve of the ROC (ROC AUC) which is a measure of sensitivity vs. specificity where the AUC ranges from 0.5 (no apparent distributional difference between the two groups of test values) to 1 (perfect separation of the test values of the two groups) [188]. ROC AUC was calculated using the built in perfcurve function in Matlab. We report ROIs that pass the permutation test at $p \leq 0.05$, survive FDR correction at $\alpha = 0.2$, and report the ROC AUC for completeness. We then visualize these results on a brain mesh using BrainNet Viewer [190].

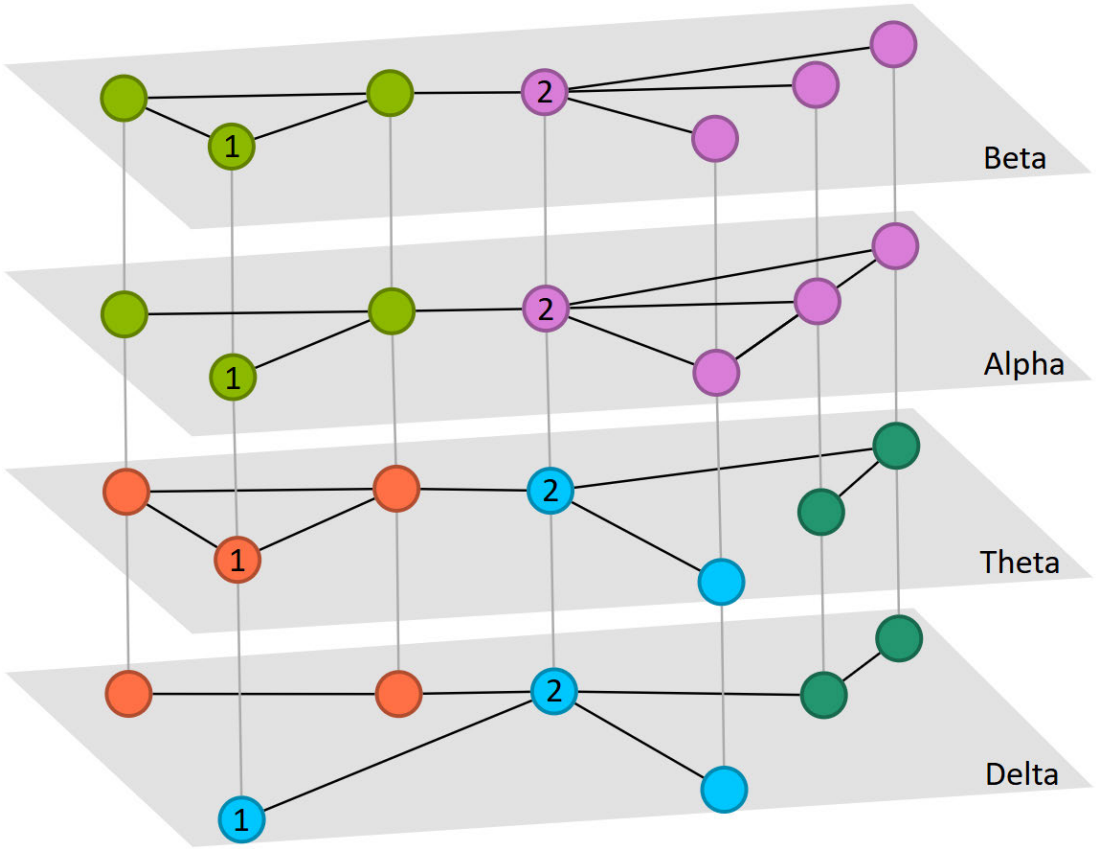

Figure 4.2: Modular multiplex frequency networks. Visualized is a multiplex frequency network for the 4 frequency bands – delta, theta, alpha and beta. Multiplex modularity has been calculated for the network and nodes have been given a group assignment based on colour. To visualize flexibility in this network consider node one. Node one swaps group assignment twice (blue→orange then orange→green) of 3 consecutive layer pairs giving it a flexibility of $\frac{2}{3}$. For collapsibility, consider node two in the beta layer. We compare the nQ (contribution to modularity) for this node to its spatial replica in the other layers and count the number of times where the difference in nQ is less than our collapsibility threshold ε multiplied by the average nQ across these node replicas ($\overline{nQ_i}$). For instance, compare node two in the beta layer to node two in the alpha layer. Both nodes share similar topology and group structure and thus do not have very different values of nQ. On the other hand, node two in the beta layer has substantially different topology to node two in the theta layer. In this case, the difference in nQ would require a large ε to count towards our value of collapsibility. It follows that we compare all nQ across all layer pairs and determine the proportion of nodes where the difference in nQ is under $\varepsilon\overline{nQ_i}$, and normalized by all layer pairs in the network. For a recap and more detailed explanation and visualization of nQ see Fig. 3.2 in the prior chapter.

4.3 Results

In this section, we present the results of our analysis of the surrogate networks as in Section 4.2.1 and application to VSTMBT-EEG data described in Section 4.2.2.

4.3.1 Surrogate network results

Initially, we explored the behaviour of nQ in comparison to other common measures of node influence (degree, multiplex clustering coefficient and multiplex PageRank) with increasing network size (both nodes and layers) across our SBTM surrogate networks. We find that, as the number of layers increases, that the mean correlation between degree and nQ increases from a weak negative correlation ($r = -0.3$) to close to no correlation at layer 30 ($r = -0.16$), as in Fig. 4.3a. Similarly, the correlation between nQ and the multiplex clustering coefficient approaches no correlation as the number of layers increases ($r = 0.3 \rightarrow r = -0.05$) as in Fig. 4.3b. On the other hand, the correlation between nQ and PageRank decreases with the number of layers ($r = -0.036 \rightarrow r = -0.054$) but remains close to no correlation and has a slight increase when going from 2 to 4 layers as seen in Fig. 4.3c.

When exploring these dynamics as the number of nodes increases, we observe a decreases in nQ vs. degree ($r = -0.2 \rightarrow r = -0.243$) and multiplex clustering coefficient ($r = 0.075 \rightarrow r = -0.005$) in Fig. 4.3a and 4.3b, while nQ vs. PageRank increases ($r = -0.057 \rightarrow r = -0.035$).

In sum, all three comparisons show a very low mean correlation with increases in both the number of layers and nodes. In addition, the variability in all cases is high and will be explored in more detail in the following analyses.

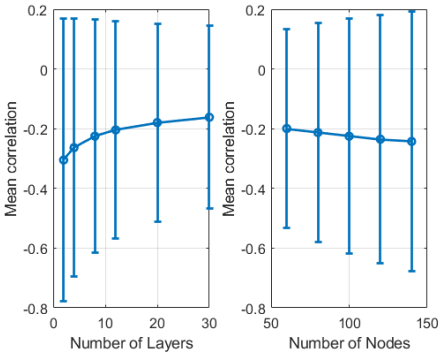

(a) Degree vs. nQ

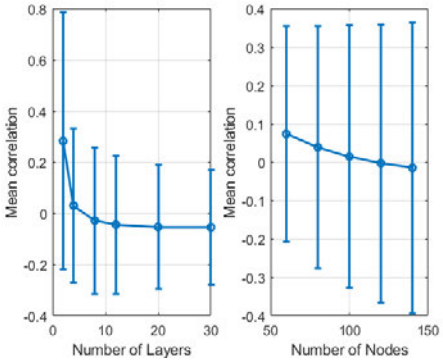

(b) Clustering Coefficient vs. nQ

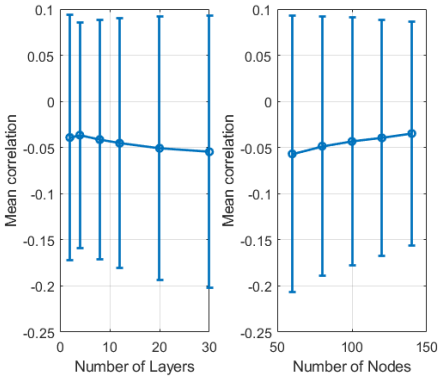

(c) PageRank vs. nQ

Figure 4.3: Mean correlation between network measures. Here, we visualize the mean correlation across our surrogate networks between our measures of node importance and nQ as a function of network size (number of nodes and number of layers). In addition, the standard deviation for each comparison is represented by bars.

Similarly, we also look at the mean correlation between flexibility and collapsibility in our surrogate networks as the number of layers increases for various collapsibility thresholds. As visualized in Fig. 4.4, for all collapsibility thresholds, the correlation decreases with the number of layers but remains close to zero. The correlation become slightly stronger with an increasing collapsibility threshold with the strongest negative correlation occurring for $\varepsilon = 0.9$ and at layer 30 where $r = -0.1$. In general, correlations between collapsibility and flexibility remain close to zero across the number of layers and collapsibility thresholds.

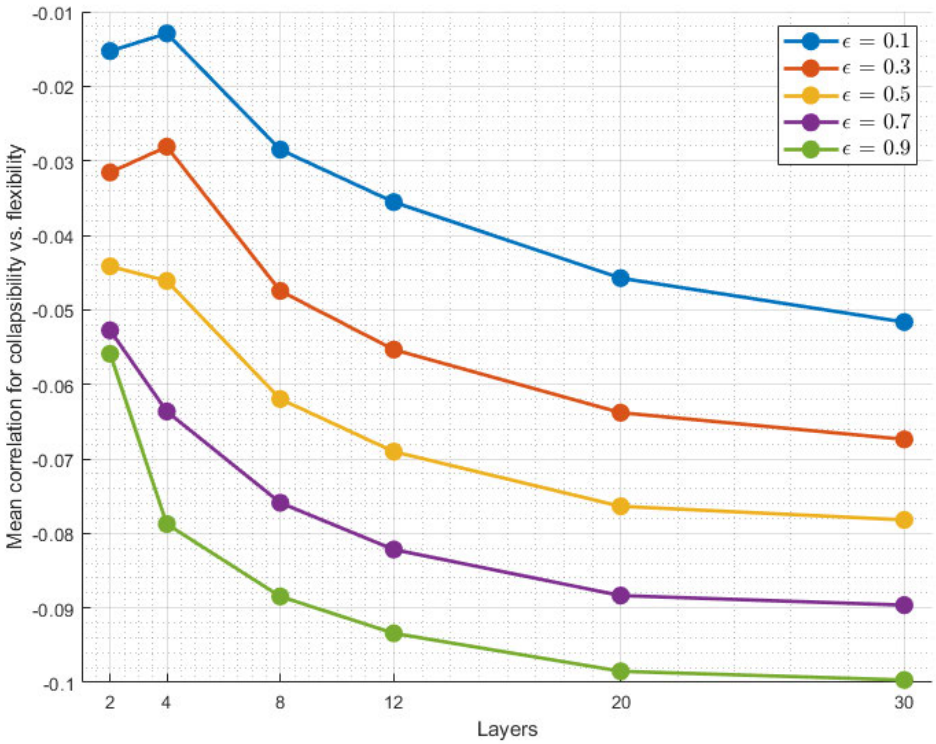

Figure 4.4: Collapsibility vs. flexibility as network size increases. Here we explore the mean correlations between collapsibility and flexibility as the number of layers in the network increases. This is done for a range of collapsibility thresholds (ε). While collapsibility and flexibility become more negatively correlated as the number of layers increases, this correlation remains very small.

Additionally, we look at the distributions of collapsibility for nodes in the network as the collapsibility threshold (ε) increases. As expected, as ε approaches 1, more nodes in the network are collapsible and the collapsibility of the network also approaches 1. However, notice that the largest change in distribution happens between $\varepsilon = 0.1$ and $\varepsilon = 0.3$ and that further increases in ε result in smaller changes in distribution, as seen in Fig. 4.5.

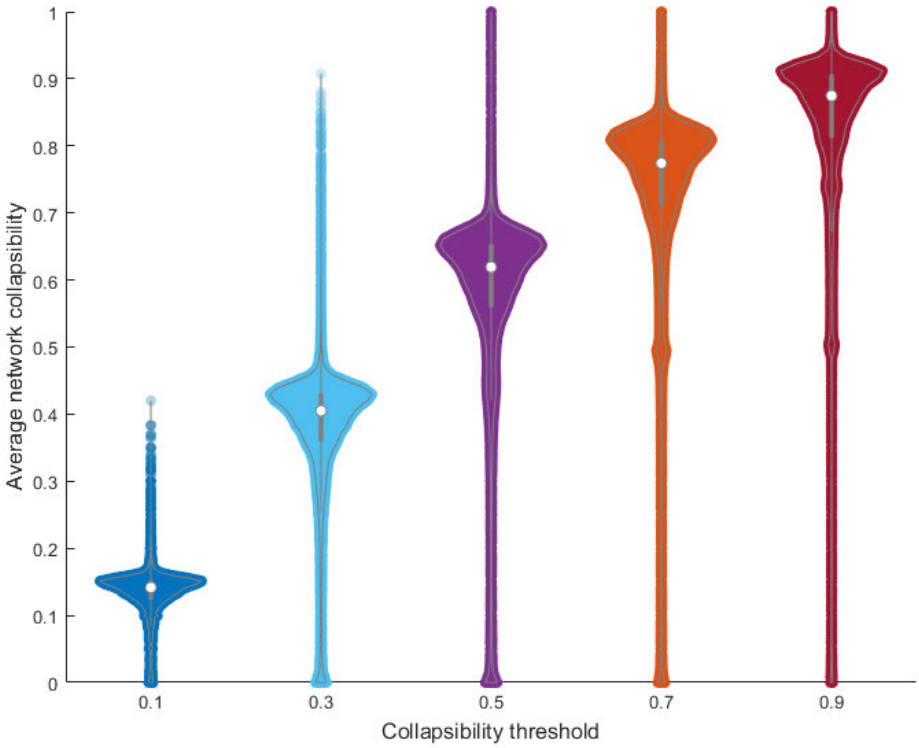

Figure 4.5: Distributions of collapsibility for different collapsibility thresholds. We visualize the distributions of average network collapsibility for different collapsibility thresholds (ε), using violin plots from publicly available code [195]. As we increase ε, average network collapsibility approaches 1 as expected (that is all nodes become totally collapsible). Interestingly, the jump in average network collapsibility sees the biggest increase from $\varepsilon = 0.1 \rightarrow 0.3$. Increases in network-wide collapsibility decreases as ε approaches 1, indicating that ε values between 0.1 and 0.3 may be most suitable in determining node level changes in nQ variability.

We wanted to explore these distributions for low values of ε in more detail. We do so in increments of 0.05 for the range $\varepsilon = 0.05 - 0.3$. We find that incremental increases of ε in this range result in proportional increases in mean collapsibility as seen in Fig. 4.6. As such, and given the large increase in collapsibility from $\varepsilon = 0.1$ and $\varepsilon = 0.3$, we choose an $\varepsilon = 0.2$ for our analysis of the EEG data in the next Section 4.3.2.

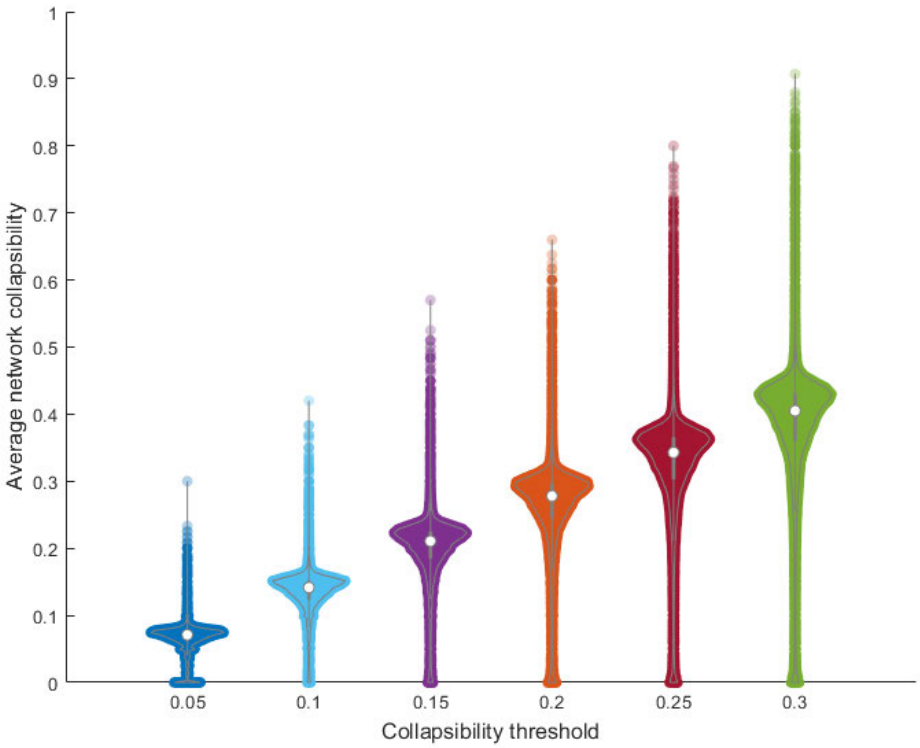

Figure 4.6: Collapsibility distributions in finer detail. Expanding on the results visualized in Fig. 4.5, we explore the distributions of average network collapsibility for ε in the range [0.05, 0.3].

Returning to the correlations between nQ and the other graph measures, we wanted to explore these distributions in more depth. Specifically, observe the correlations between nQ and multiplex clustering coefficient and degree as the number of layers increases as seen in Fig. 4.7 and 4.8. We can see that, while the mean correlation may have been low, that some of the surrogate networks contain high positive and negative correlations.

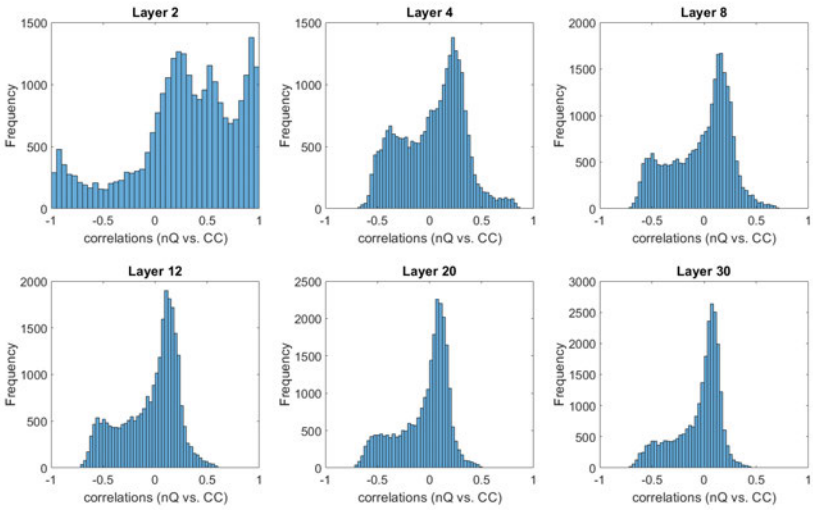

Figure 4.7: Correlations between nQ and multiplex clustering coefficient in SBTM surrogate networks. Here we visualize correlations between nQ and multiplex clustering coefficient (CC), and the frequency of their occurrence, as the number of layers in the network increases. While the majority of correlations remain low for all layer constructions, the presence of high negative and positive correlations decreases with network size.

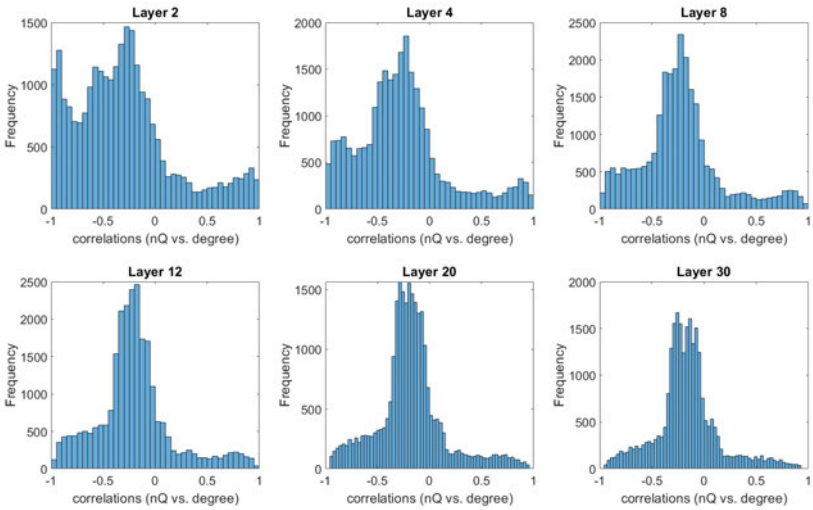

Figure 4.8: Correlations between nQ and Degree in SBTM surrogate networks. Visualizations of the correlations between nQ and degree, and the frequency of their occurrence, in the multiplex SBTM surrogate networks as the number of layers increases. Similar to our multiplex clustering coefficient results, we observe a decrease in the presence of high positive and negative correlations as the number of layers increases as expected. Note however that there are more high correlations for degree than clustering coefficient. This may be due to the simplicity of stochastic block modelling along with construction with high modular structure (nodes within these modules have high connectivity leading to both a high nQ and degree).

We explore what parameters drive these high and low correlations by calculating the mean of the parameters for positive and negative correlations that pass $r \geq |0.6|$. We find that, for the multiplex clustering coefficient, 4 parameters drive both the positive and negative correlations – p_{in}, p_{out}, $probNew$, and $probExist$. Specifically, network constructions with high p_{in} with low p_{out} (indicating a highly modular network), and a low number of communities (decreasing with the number of layers), drive the significant negative correlations between nQ and multiplex clustering coefficient as seen in Table 4.3. This suggests a key structural distinction between nodal modularity and multiplex clustering coefficient. Specifically, nodes with high nQ in larger multiplex networks with few communities tend to be strongly embedded within modular structure across layers and are therefore more robust to changes in local connectivity (driven by $probNew$ and $probExist$) that may disrupt multiplex triangles. In contrast, nodes with a high number of multiplex triangles do not necessarily contribute strongly to modular structure and may therefore exhibit lower nQ, particularly in larger multiplex networks where the impact on modularity of a node with a high number of multiplex triangles carries less weight due to the local nature of the measure. This distinction between nQ and multiplex clustering coefficient helps to explain the negative correlations observed. It should be noted that the 2 and 4 layer constructions also exhibit lower $probNew$ and $probExist$ (only $probExist$ is lower in the 4 layer case and with a low $classChangeRate$). That is, less edges are retained and not many new edges form which could lead to some network constructions with a lower number of multiplex triangles but where some nodes are still important to modular structure (high nQ). This behaviour in the 2 and 4 layer constructions but not for a higher number of layers may be due to the first layer in the SBTM having high modularity (high p_{in} and low p_{out}), where nQ would still remain high even though modular structure is disrupted in subsequent layers (leading to a proportionally higher reduction in multiplex triangles).

Table 4.3: Parameters for high negative correlations between nQ and multiplex clustering coefficient. This table presents the average of each parameter for nQ vs. multiplex clustering coefficient correlations with $r \leq -0.6$ as the number of layers in our SBTM networks increases. Each parameter is listed, followed by the overall mean, then the average for each specific layer setup with standard deviation. Note that negative correlations occur almost always in highly modular networks - the highest choice for p_{in} (within module connections) and lowest p_{out} (between module connections), and with a low number of communities.

Parameters	Mean	2 layers	4 layers	8 layers	12 layers	20 layers	30 layers
Nodes	100	106 ± 27.3	110 ± 25.8	117 ± 23.2	119 ± 22.3	120 ± 21.1	122 ± 19.4
Communities	6	3.23 ± 1.85	2.49 ± 0.864	2.82 ± 1.23	2.68 ± 1.11	2.58 ± 1.06	2.46 ± 0.903
p_{in}	0.5	0.733 ± 0.242	0.9 ± 0	0.891 ± 0.0356	0.887 ± 0.0418	0.889 ± 0.0391	0.895 ± 0.0281
p_{out}	0.5	0.267 ± 0.242	0.1 ± 0	0.109 ± 0.0356	0.113 ± 0.0418	0.111 ± 0.0391	0.105 ± 0.0281
$probNew$	0.5	0.354 ± 0.304	0.579 ± 0.185	0.564 ± 0.210	0.581 ± 0.228	0.590 ± 0.241	0.604 ± 0.238
$probExist$	0.5	0.208 ± 0.145	0.151 ± 0.0878	0.528 ± 0.352	0.590 ± 0.344	0.647 ± 0.330	0.656 ± 0.329
$classChangeRate$	0.5	0.468 ± 0.315	0.200 ± 0.156	0.476 ± 0.320	0.464 ± 0.316	0.462 ± 0.315	0.462 ± 0.316

On the other hand, positive correlations are largely driven by less modular networks, with low p_{in} and high p_{out} (aside from the 2 layer networks), and with a higher number of communities on average (see Table 4.4). Furthermore, we see $probExist$ decreasing and $probNew$ increasing substantially from layer 4 onwards indicating that positive correlations are also driven by layer dynamics which lead to large changes in network structure. This could lead to the formation of multiplex triangles where edges which form part of the multiplex triangle disappear on one layer to then close the triangle on the next layer. The closing and unclosing of multiplex triangles caused by a high $probNew$ and a low $probExist$ could lead to nodes that have a high multiplex clustering coefficient and high nQ (repeated structures forming cross-layer modules). However, this behaviour seems to have a limit as from layer 20 onwards we saw no significant positive correlations within the surrogate networks. This could be explained by the multiplex clustering coefficient being a more local measure of connectivity than nQ where more layers can result in more complex modular structure that is less influenced by local dynamics captured by the multiplex clustering coefficient.

Table 4.4: Parameters for high positive correlations between nQ and multiplex clustering coefficient. Here, we present the average of each parameter for nQ vs. multiplex clustering coefficient correlations with $r \geq 0.6$ as the number of layers increases. Each parameter is listed, followed by the overall mean, then average for each specific layer setup with standard deviation. Note that positive correlations occur almost always in highly non-modular networks - the lowest choice for p_{in} (within module connections) and highest p_{out} (between module connections). However, this is not the case for 2 layer networks where high positive correlations exist for modular network constructions. This could be due to how multiplex clustering coefficient is calculated for networks with 2 vs. 3 or more layers, discussed below. Additionally, positive correlations exist in networks with a larger number of average communities (~ 5) unlike the negative correlations.

Parameters	2 layers	4 layers	8 layers	12 layers
Nodes	104 ± 27.6	109 ± 26.8	116 ± 23.6	140 ± 0
Communities	5.84 ± 2.57	5.24 ± 1.91	4.95 ± 1.29	5 ± 1.41
pin	0.708 ± 0.294	0.104 ± 0.0247	0.1 ± 0	0.1 ± 0
p_{out}	0.292 ± 0.294	0.896 ± 0.0247	0.9 ± 0	0.9 ± 0
$probNew$	0.697 ± 0.242	0.827 ± 0.0963	0.887 ± 0.0497	0.9 ± 0
$probExist$	0.533 ± 0.316	0.154 ± 0.0887	0.1 ± 0	0.1 ± 0
$classChangeRate$	0.493 ± 0.317	0.488 ± 0.314	0.453 ± 0.298	0.5 ± 0.283

In sum, we see a pattern where significant positive or negative correlations are largely driven by both ends of the extreme in modular or non-modular networks. It should also be noted that networks constructed from two layers have slightly different behaviour for our multiplex measures other than nQ. This is due to their definitions considering both the following and preceding layers in their calculation. For networks with three or more layers, the central layer has both following an preceding layers considered in calculation while the first and third layers only have either one preceding or one following layer influencing its value.

Next, we explore the parameters that drive the significant positive and negative correlations between nQ and degree.

For both the negative and positive correlations we see increasing p_{in} and decreasing p_{out} with the number of layers along with a decreasing number of communities as seen in Table 4.5 and 4.6. However, positive correlations occurred where the number of communities was lower and $probNew$ and $probExist$ were significantly smaller. This suggests that positive correlations occurred where the modular network underwent less dynamic change across layers, whereas negative correlations occurred where modular structure was more disrupted in subsequent layers.

Table 4.5: Parameters for high negative correlations between nQ and degree. This table shows the average parameters used to construct SBTM networks when correlations between nQ and degree have $r \leq -0.6$. Similarly to multiplex clustering coefficient, as the number of layers increases, these negative correlations occur largely in high modularity networks with high p_{in} and low p_{out}, and decreasing community size.

Parameters	2 layers	4 layers	8 layers	12 layers	20 layers	30 layers
Nodes	104 ± 27.9	107 ± 27.2	108 ± 26.9	109 ± 26.5	110 ± 26.3	111 ± 26.2
Communities	5.93 ± 2.59	5.47 ± 2.43	5.09 ± 2.33	4.81 ± 2.27	4.45 ± 2.20	4.19 ± 2.10
p_{in}	0.684 ± 0.310	0.776 ± 0.236	0.832 ± 0.151	0.847 ± 0.108	0.856 ± 0.0684	0.855 ± 0.0686
p_{out}	0.316 ± 0.310	0.224 ± 0.236	0.168 ± 0.151	0.153 ± 0.108	0.144 ± 0.0684	0.145 ± 0.0686
$probNew$	0.731 ± 0.214	0.733 ± 0.210	0.715 ± 0.227	0.711 ± 0.231	0.714 ± 0.227	0.721 ± 0.221
$probExist$	0.525 ± 0.317	0.587 ± 0.313	0.677 ± 0.278	0.727 ± 0.240	0.782 ± 0.184	0.823 ± 0.125
$classChangeRate$	0.494 ± 0.317	0.489 ± 0.316	0.490 ± 0.316	0.488 ± 0.316	0.489 ± 0.316	0.489 ± 0.316

Table 4.6: Parameters for high positive correlations between nQ and degree. Here we show the average parameters used to construct SBTM networks when correlations between nQ and degree have $r \geq 0.6$. Positive correlations also occur largely in highly modular networks with high p_{in}, low p_{out} and decreasing community size as with the negative correlations. However, the main difference is in $probNew$ and $probExist$ being significantly lower than for the negative correlations. That is, positive correlations are driven by less network dynamics as expected (the highly modular network remains similar and thus nodes within modules have a large number of connections yielding high degree and high nQ).

Parameters	2 layers	4 layers	8 layers	12 layers	20 layers	30 layers
Nodes	105 ± 27.7	105 ± 27.5	106 ± 27.3	106 ± 27	109 ± 26.5	111 ± 25.9
Communities	4.01 ± 2.37	3.94 ± 2.32	3.67 ± 2.13	3.41 ± 1.9	3.07 ± 1.53	2.84 ± 1.24
p_{in}	0.811 ± 0.138	0.832 ± 0.0747	0.834 ± 0.0745	0.837 ± 0.0741	0.839 ± 0.0736	0.844 ± 0.0726
p_{out}	0.189 ± 0.138	0.168 ± 0.0747	0.166 ± 0.0745	0.163 ± 0.0741	0.161 ± 0.0736	0.156 ± 0.0726
$probNew$	0.211 ± 0.12	0.154 ± 0.107	0.145 ± 0.0834	0.143 ± 0.0822	0.139 ± 0.0793	0.13 ± 0.0711
$probExist$	0.206 ± 0.148	0.234 ± 0.175	0.238 ± 0.181	0.24 ± 0.182	0.242 ± 0.189	0.234 ± 0.187
$classChangeRate$	0.497 ± 0.317	0.496 ± 0.317	0.497 ± 0.316	0.5 ± 0.317	0.494 ± 0.316	0.496 ± 0.316

Given the highly structured nature of the SBTM, we investigated whether these parameters still drive these high and low correlations when the transition steps of the model are more complex. Specifically, we explored 100 surrogate networks that follow network dynamics based on a task with rest and stimuli (see Section 4.2.1). Specifically, we explored high p_{in} with low p_{out} (both cases [0.9,0.1] and [0.75,0.25] with 100 nodes, 8 layers, and 3 communities). See Fig. 4.9 and 4.10 for example structure.

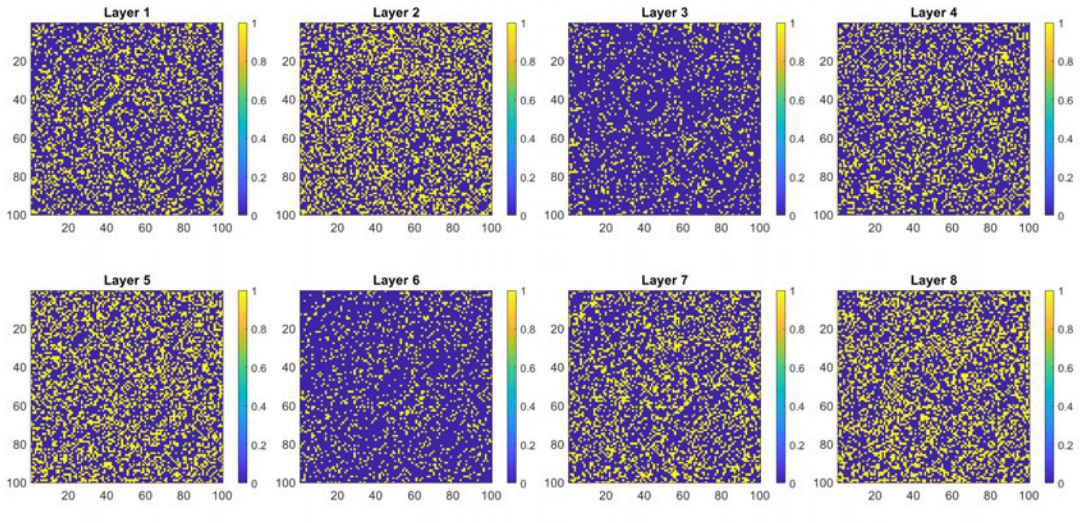

Figure 4.9: SBTM simulating task-based activity with p_{in} = 0.9, p_{out} = 0.1. This figure visualizes an augmented version of the SBTM with states of high and low activity to imitate task-based neuroimaging networks. These were constructed with parameters that yielded a high correlation between nQ and both degree and multiplex clustering coefficient. In this example, we found $r = -0.0019$ and $r = 0.1852$ for multiplex clustering coefficient and degree respectively. Correlations with multiplex PageRank also remained low at $r = 0.0835$.

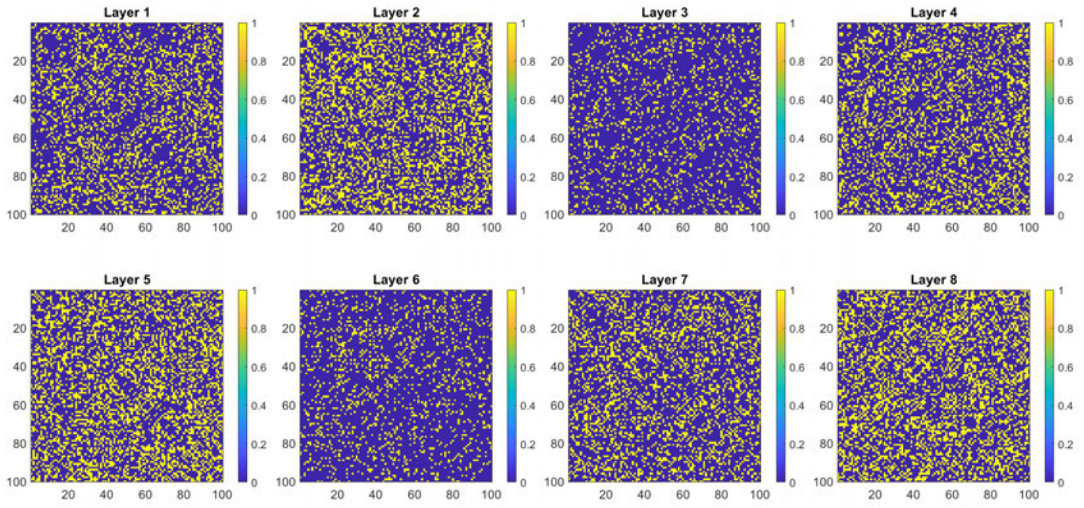

Figure 4.10: SBTM simulating task-based activity with p_{in} = 0.75, p_{out} = 0.25. We visualize SBTM networks with task-based network dynamics to more closely imitate real-world, task-based networks, in neuroimaging. We find, like with the prior example (p_{in}=0.9 and p_{out}=0.1), that constructing these networks with parameters that yielded high correlations between nQ and the other graph measures no longer does. Specifically, we found $r = -0.0011$ for nQ vs. multiplex clustering coefficient, $r = 0.1875$ for degree, and $r = 0.084$ for multiplex PageRank.

In these two examples (p_{in}=0.75, p_{in}=0.9), we find that correlation between nQ and multiplex clustering coefficient, degree, and PageRank are all very low ($r = (-0.0011, -0.0019)$, $r = (0.1874, 0.1852)$ and $r = (0.084, 0.0835)$, respectively). This suggests that the previously observed strong correlations between nQ and the other graph measures, explored in Tables 4.3 - 4.6, may have been driven by the homogenous per-layer network dynamics imposed by the standard SBTM, in which $probNew$, $probExist$ and $classChangeRate$ are fixed. In contrast, real-world network dynamics and particularly in task-based brain networks, are substantially more heterogeneous. Incorporating even simple network dynamics designed to mimic those present in task-based brain networks markedly changes the relationship between nQ and the other graph measures. These findings, complementary to those in Chapter 3, provide further support that nQ captures distinct aspects of multiplex network organization that are not reflected by standard metrics, supporting its use as a complementary measure for multiplex brain network analyses.

4.3.2 Application to EEG data

Here, we explore the changes in nQ, flexibility and collapsibility between controls and MCI using permutation test and the area under the curve of the ROC, reporting brain regions that pass the thresholds of $p \leq 0.05$ and where p is FDR controlled at $\alpha = 0.2$.

We find that, for the probe phase of the binding task in the delta frequency band, that several brain regions exhibit statistically significant decreases in nQ for MCI subjects (see Fig. 4.11 and Table 4.7). These ROIs show very low p-values (range: [0.0006, 0.0011]), moderate negative effect sizes (range: [-0.4823,-0.4546]) and ROC AUC in the range: [0.6239, 0.6416]. Note that these ROIs were accepted at $\alpha = 0.2$ during FDR correction which means that up to 20% of the detected ROIs could be false positives. Furthermore, see B.1 for visualizations of all FDR corrections for the results given in this section.

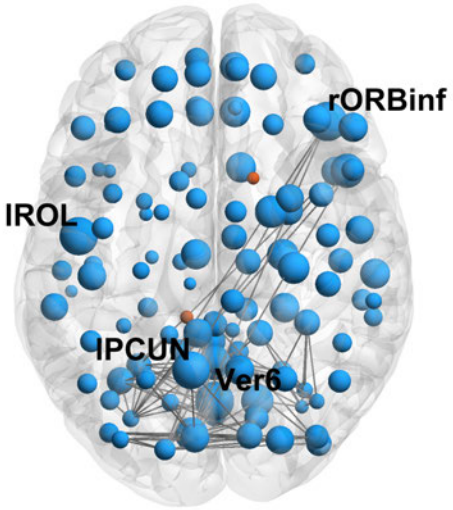

Figure 4.11: Changes in nQ for the probe phase of the binding task. We visualize changes in nQ between controls and MCI for the multiplex frequency networks of the VSTMBT-EEG data. We only found statistically significant changes in the delta band and so have simplified the visualization to include only one brain (rather than all four frequency bands in a multiplex construction as in Fig. 4.2). Here, nodes in blue represent a loss in nQ while orange represents a gain and the size of the node is the magnitude of this change. Labelled nodes are those that passed $p \leq 0.05$ in the permutation test and FDR corrected at $\alpha = 0.2$. These labels follow the form l or r for left or right hemisphere respectively, followed by the shortened version of the ROI (i.e., CUN refers to the cuneus). Refer to Table 4.7 for more detail. This visualization was achieved with BrainNet viewer [190] and with the top 1.5% of the edges are visualized for clarity. Note that almost all nodes observe a loss in nQ.

Table 4.7: Changes in nQ for EEG multiplex binding probe for controls vs. MCI. This table displays the ROIs which pass $p \leq 0.05$ and FDR correction at $\alpha = 0.2$. L and R refer to the left and right hemisphere of the brain respectively. p-values and effect sizes are given from the permutation test and the area under the curve (AUC) of the receiver operating characteristic (ROC).

ROIs	p	effect size	ROC AUC
R Inferior Frontal Orbital	0.0006	-0.4823	0.6416
L Rolandic Operculum	0.0006	-0.4638	0.6239
L Precuneus	0.0011	-0.4546	0.6290
Vermis 6	0.0011	-0.4741	0.6388

Next, we explore these same changes in flexibility between controls and MCI. We find statistically significant changes in both the probe phases of the binding task (see Fig. 4.12 and Table 4.8) and shape task (see Table 4.9). Given that findings are primarily found for the binding task (both across these comparisons in EEG and in the prior chapter in fMRI), we focus on reporting visualization for the binding task only. Note that only one ROI passes statistical thresholds for flexibility in the binding task, while three are found in shape. This is an unusual result given the known sensitivity of specifically the binding task to early stage AD.

Table 4.8: Changes in flexibility for EEG multiplex binding probe for controls vs. MCI. Here we display the ROIs which pass $p \leq 0.05$ and FDR corrected at $\alpha = 0.2$. L and R indicated the left and right hemispheres of the brain respectively. p-values and effect sizes were obtained from permutation testing and the standard area of the curve of the receiver operating characteristic is given (ROC AUC).

ROIs	p	effect size	ROC AUC
R Rectus	0.0001	-0.1846	0.5093

Table 4.9: Changes in flexibility for EEG multiplex shape probe for controls vs. MCI. As before, we display the ROIs which pass $p \leq 0.05$ and FDR corrected at $\alpha = 0.2$. L and R indicated the left and right hemispheres of the brain respectively. p-values and effect sizes were obtained from permutation testing and the standard area of the curve of the receiver operating characteristic is given (ROC AUC). Interestingly, for flexibility, we find more significant ROIs in the shape task than the binding task. This is despite known deficits in visual memory binding in MCI which are not typically seen in the shape only task.

ROIs	p	effect size	ROC AUC
L Anterior Cingulum	0.0001	-0.2396	0.5140
R inferior Occipital	0.0021	0.4061	0.5417
R Superior Temporal Pole	0.0032	0.3972	0.5370

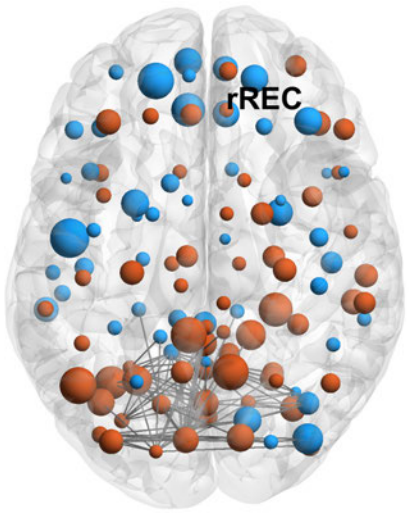

Figure 4.12: Changes in node flexibility in controls vs. MCI for the probe phase of the binding task. As before, blue nodes represent a loss of flexibility while red nodes represent a gain. The magnitude of this change is node size, labelled nodes are those that pass the statistical thresholds, and visualization of this network was achieved with the BrainNet viewer with the top 1.5% of edges shown for clarity. Here, one brain is shown (rather than four for each frequency band) since flexibility is an aggregated measure which captures the variability of module assignment over the layers of the network. Edges visualized are taken from the average MCI network.

Lastly, we explore the changes in collapsibility between controls and MCI. We find that, for the binding task only, that we see statistically significant changes in collapsibility for both the encoding (see Fig. 4.13 and Table 4.10) and probe (see Fig. 4.14 and Table 4.11) phases of the task. However, more significant changes are found in probe (7 ROIs vs. 1 ROI). For the probe phase, p-values are very small (range: [0.0003, 0.0121]), with low-moderate effect sizes (range: [-0.4735, 0.3654]) and low ROC AUC (range: [0.5962 - 0.6171]). See Table 4.11 for more detail.

Table 4.10: Changes in collapsibility for EEG multiplex binding encoding for controls vs. MCI. Table details follow from Table 4.7.

ROIs	p	effect size	ROC AUC
L Middle Frontal	0.0011	-0.4547	0.6130

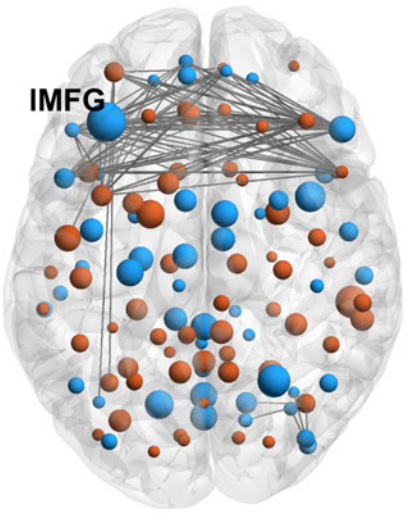

Figure 4.13: Changes in collapsibility in controls vs. MCI for the encoding phase of the binding task. Figure generation and details follow from Fig. 4.11. Additionally, collapsibility is an aggregated measure of nQ variability across the four frequency bands. As such, only one brain is visualized for this and the edges displayed come from the averaged MCI network.

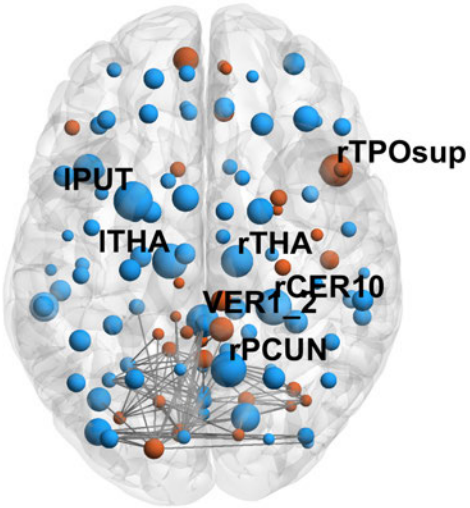

Figure 4.14: Changes in collapsibility between controls vs. MCI for the probe phase of the binding task. Figure generation and details follow from Fig. 4.11. As before, one brain is visualized since collapsibility is an aggregated measure across the four frequency bands.

Table 4.11: Changes in collapsibility for EEG multiplex binding probe for controls vs. MCI. Table details follow from Table 4.7.

ROIs	p	effect size	ROC AUC
R Precuneus	0.0019	-0.4173	0.6036
L Putamen	0.0003	-0.4736	0.6171
L Thalamus	0.0039	-0.4093	0.6016
R Thalamus	0.0121	-0.3577	0.6004
R Superior Temporal Pole	0.0070	0.3654	0.5962
R Cerebellum_10	0.0019	-0.4268	0.6154
Vermis 1_2	0.0076	-0.3686	0.6101

4.4 Discussion

The following sections explore nQ's validation in synthetic networks and how aggregation methods can support the understanding of nQ in multiplex networks. Additionally, we discuss how nQ, flexibility, and collapsibility change in VSTMBT-EEG frequency networks and how these may reflect neuroanatomical deficits due to early AD.

4.4.1 nQ as a relevant measure in large multiplex networks

Multiplex networks in neuroimaging have revealed insights into how the brain dynamically evolves over time and how this effects modular organization and inter-frequency dynamics [17, 171]. We had introduced nQ as a means to explore granular community structure in single-layer and multiplex networks. However, our previous study of fMRI and DTI was limited in multiplicity by only considering single-layer and dual-layer networks. This is despite the fact that many multiplex network measures behave differently in networks with three or more layers (given that nodes in middle layers have two inter-layer edges while edge layers have one) [156, 124]. To tackle these limitations, we explored nQ in surrogate networks covering typical multiplex network sizes in neuroimaging. We found that nQ only showed significant correlation with other common multiplex measures of node influence under specific network constructions on either ends of the extremes for modular networks. We tested sample constructions of these modular networks under more realistic task-based scenarios and found that these same correlations do not hold. While not an exhaustive exploration, our findings reflect hypotheses in the prior chapter which posit that nQ provides novel insight into granular community structure particularly in real-world data where the existence of noise, hub-nodes, and complex dynamic network architecture create complex topological relationships in the data. This is expected given that nQ takes into account farther reaching network structure than other more localized measures of group structure.

Additionally, a problem posed when calculating nodal measures in multiplex networks with many layers is the number of values for which meaningful interpretation becomes challenging. One method to tackle this is by creating aggregate node measures which summarize multiplex interactions over the layers of the network [156]. We introduced collapsibility as an aggregate method to measure the variability in nQ over the layers of the network and showed that it provided unique insights from its most comparable measure – node flexibility.

4.4.2 Neuroanatomical exploration of VSTMBT-EEG networks

Initially, we discuss the neuroanatomical interpretation of nQ, collapsibility, and flexibility in the context of VSTMBT-EEG networks. To reiterate, multiplex networks were constructed from four frequency bands of the EEG signal – delta, theta, alpha, beta. In this context, modules can exist across frequency bands where nQ describes the contribution of an ROI to its within or across-frequency module. As such, decreases in nQ can be interpreted as decreased functional involvement or specialization of a brain region within its own group and/or an increase in between group connectivity both within and across frequency bands. A decrease in nQ can be interpreted as a loss of brain activity in a specific ROI, and/or as a result of increased between-group connectivity. These changes can reflect compensatory functional reorganization as a result of diseases such as AD where this reorganization has been observed in its early stages in EEG data [69].

Changes in nQ (specifically decreases) were only observed in the delta layer of the multiplex frequency network. The hallmark of AD in EEG is a shift in the power spectrum from faster to slower frequencies [228, 229, 230]. At the MCI stage, these increases in delta are less significant with more increases in theta. Increases in connectivity in the theta band could result in decreases in nQ in delta given the potential increase in modular importance of the theta band (i.e., increased nQ in theta causing decreases in nQ in neighbouring delta). The multiplex frequency networks may be capturing the shift in power spectrum seen in AD, though further studies are needed across the stages of MCI, and with the addition of single-frequency network analyses, to confirm these cross-network interactions. We saw cross-brain decreases in nQ in the delta band, visualized in Fig. 4.11, with 4 ROIs passing FDR correction. Of particular note is the decrease in nQ in the left precuneus. Meta-analyses of fMRI studies consistently show disruption in the bilateral precuneus [231]. In addition, cortical thinning (measured with MRI) in the precuneus was found in patients with amnestic MCI [232], and associations between these MRI-based changes and the relationship between the upper and lower parts of the alpha frequency band were found in rs-EEG [233]. In addition, this same study found that subjects with cortical thinning in the precuneus also had increased theta power, which could then lead to decreased nQ in the precuneus in delta as was observed in our study.

Next, we look at collapsibility which measures the variability of nQ across the layers of the network. In this way, a loss of collapsibility can be seen as an increase in the variability of nQ for an ROI while an increase represents a reduction in variability. In the context of this study, decreases in collapsibility can be interpreted as a greater variability in nQ across the different frequency bands, and may indicate frequency specific changes in group structure as a result of disease. Again, we see changes in the precuneus but now in the right hemisphere. This could indicate two different types of loss – one due to increases in theta power leading to reduced importance in the left precuneus within the delta band and the other due to increases in nQ variability across all frequency bands which could be additionally linked to changes in alpha observed in this study [233]. Furthermore, we observed significant changes in collapsibility in the bilateral thalamus which is known to be a key ROI to cognition and memory [234, 235, 236] along with its role in subcortical integration (i.e., with the putamen which also saw a significant loss in collapsibility) [237]. Studies of rs-fMRI have also found decreases in connectivity between the thalamus and several ROIs with significant changes in collapsibility – superior temporal gyrus [238], precuneus [239, 240], and inferior frontal gyrus (which all saw a significant change in nQ) [240]. In addition, grey matter loss within the thalamus is one of the earliest signs of cognitive decline in MCI [241]. These results further support a growing body of evidence that some of the earliest deficits in short-term memory binding in early AD are linked to changes in subcortical brain regions (specifically the thalamus and putamen in our research) [72]. Lastly, one ROI had a significant loss in collapsibility for the encoding phase of the task – the middle frontal gyrus. rs-fMRI studies have found increased functional connectivity within the middle frontal gyrus in MCI subjects, perhaps as a result of damage due to disease [242]. This is in tandem with research showing decreased functional connectivity between the thalamus and the middle frontal gyrus [239] connecting to results found in collapsibility changes in the probe phase of the task.

Flexibility, which measures the number of times an ROI changes group assignment, can be interpreted as the number of different group roles an ROI plays across the frequency bands. When flexibility increases, it can indicate an increase in instability in node membership across the frequency bands. This could indicate a loss of network integrity across the frequency bands as a result of disease pathology. However, it should be noted that instability in node membership is not necessarily a negative. For instance, both increases and decreases in node flexibility (for multiplex temporal networks) have been shown to be important for learning in task-fMRI [17].

Interestingly, while we did not find many significant results for flexibility in the probe phase of the binding task (1 ROI), we did find 3 ROIs in the shape task. There has been very little study of node flexibility in MCI and AD, with this recent paper [243] being the only one to our knowledge. Interestingly, they found brain wide increases in flexibility with the most significant changes occurring in the visual network in multiplex temporal networks of rs-fMRI. Our results

reflect this visually where increases in flexibility were observed in primarily the occipital lobe (see Fig. 4.12), while in the shape task we saw the presence of the right inferior occipital gyrus. The research in this chapter marks the first study of node flexibility in MCI within EEG networks.

In sum, we found significant changes in ROIs associated with changes in grey matter volume and functional connectivity from functional MRI and EEG studies in early AD and especially in nQ and collapsibility metrics. These changes were almost exclusively found in the binding task and not shape, agreeing with prior literature on the VSTMBT where binding deficits are specifically impaired in early AD [29]. Interestingly, almost all significant findings were observed in the probe phase of the VSTMBT and not the encoding phase. Gonzalez-Montealegre *et al.* [70] found that over-recruitment in brain activity occurred during the probe phase specifically in the same cohort of subjects. However, our results do not reflect the loss in encoding activity that they also observed.

Interestingly, in this VSTMBT-EEG cohort, we saw a greater number of ROIs when comparing controls to MCI than in our fMRI multiplex networks in the prior chapter (4 vs. 0 ROIs). This is surprising given that the EEG cohort had some heterogeneity in MCI diagnosis (18% of the subjects had non-amnestic MCI). However, the difference in our EEG and fMRI results in these chapters may largely be explained by modality differences. A simultaneous EEG-fMRI study highlights these differences, where abnormalities in EEG-fMRI signal coupling between controls and MCI were seen in the DMN, salience network, fronto-parietal network, and thalamus while amyloid pathology was specifically associated with fMRI specifically (consistent with the results in Chapter 3) [244]. Additionally, in the prior chapter, we explored dual-layer temporal networks of the VSTMBT. Here, we look at frequency-based networks of the VSTMBT for encoding and probe separately. This may indicate that cross-frequency interactions in nQ may be an early indicator of MCI for the binding task of the VSTMBT. Given that we saw only changes in the delta frequency band, known to be one of the earliest affected in AD, it could indicate that further research should explore how the delta band interacts with the other frequencies topologically through nQ. In addition, it is of interest to see if these changes are reflected in later stages of the disease and specifically in MCI converters. The EEG cohort used in this study is in the process of obtaining MCI converter data after a 3-year follow up with the subjects. Future work should continue this study as this data becomes available.

In this chapter, we explored source-space networks of VSTMBT-EEG data. However, source estimation techniques often struggle with the reconstruction of deep-brain sources due to volume conduction effects leading to inaccurate measures of functional connectivity [245]. Newer methods such as eLORETA (used in this study) provide better localization of deep sources and perform above most other methods [246]. However, no one method is perfect

in the estimation of EEG source activity. eLORETA still has some source localization error which can influence the functional connectivity of the networks constructed in this study [246]. Future work may consider combining multiple source localization methods to improve performance [246].

It should be noted that in all of our nQ, collapsibility, and flexibility results we found very low p-values but moderate effect sizes and poor ROC AUC. While p-values are encouragingly low and corrected for multiple comparisons (see B.1 for more detail), the low ROC AUC indicates a weak ability to discriminate controls from MCI on a subject specific basis. This is likely due to the modest effect sizes and to both the early stage of the disease and the heterogeneity of MCI diagnosis. Specifically, 19 of the 108 (18%) subjects had non-amnestic MCI which is not considered a prodromal stage of AD [70]. Furthermore, a limitation of this study was that both age and years of education were cofactors in the comparisons of healthy and MCI that were not accounted for in the statistical analyses. While the difference in age between healthy subjects and MCI was small (~1.7 years), there was a large gap in the years of education (~5 years less in the MCI cohort). However, Gonzalez-Montealegre *et al.* [70] suggest that the reduced years of education in our MCI subjects, but similar MMSE scores to a closely related study by Pietto *et al.* [247], indicate that the subjects are in less advanced stages of MCI. This was additionally supported by increased neural recruitment over regions where Pietto *et al.* [247] found decreases. Additionally, no information on follow-up yet means that some subjects could be MCI converters, further increasing heterogeneity. The prior chapter provided evidence that nQ is sensitive to this stage of AD specifically (in fMRI) and the potential presence of these subjects in the MCI cohort could negatively influence discriminative capabilities (given that nQ effect sizes in the fMRI cohort were both large and positive opposed to the primarily negative effect sizes observed in the EEG cohort).

4.5 Conclusion

In the prior chapter, nQ was established as a novel method of granular community detection to understand node-level network dynamics in multiplex networks and how these change with diseases known to effect modular structure such as AD. However, the study of nQ was limited in network size to dual-layer temporal networks, which can behave differently to multiplex networks of three or more layers given that middle layers contain two inter-layer edges while beginning and end layers have one. While results in chapter 3 were positive in categorizing a key stage of AD (MCI converters), they were achieved using fMRI data which is costly and not widely available.

To tackle this, we explored nQ in larger multiplex surrogate networks of typical size in neuroimaging studies. Given that changes in nodal graph measures (such as nQ) can be difficult to interpret as network size increases, we also introduced a novel aggregated network measure, collapsibility, to measure nQ variability in these networks. Lastly, we explored these measures in source space VSTMBT-EEG multiplex frequency networks.

We found that nQ maintained novel behaviour as network size increased in comparison to other common multiplex measures of node influence. Furthermore, cases where nQ behaved similarly to these measures were in scenarios of simple or highly modular connectivity and not reflective of real-world scenarios that contain more complex topology and noise. We also found that collapsibility was distinct from its most similar nodal measure of node flexibility. However, we note a limitation of this study in that the SBTM networks used in this study lack some typical characteristics of real-world networks such as real-world noise, existence of hub nodes which connect communities across layers, and lack of realistic variability in community size and internal densities.

In the VSTMBT-EEG multiplex networks, we found changes in nQ and collapsibility which agreed with changes in grey matter and with known changes in functional connectivity centred around the thalamus – a key ROI in memory. Furthermore, changes in nQ in the delta band could be linked to shifts in the power spectra from higher to lower frequencies, a hallmark of AD in EEG data. In addition, almost all results were found for the binding task and not the shape task which is consistent with known binding deficits in MCI and AD. However, effect sizes were moderate and ROC AUC was poor (likely linked to effect size and sample heterogeneity). Further research of VSTMBT-EEG multiplex networks are needed to explore whether these results are seen in less heterogeneous MCI and in later stages of the disease (MCI converters) where these effects are expected to be more dramatic. This would present a promising case for the use of nQ and collapsibility for MCI and AD in understanding brain related changes in an affordable modality at the earliest stages of disease.

Separate to our EEG findings, it is important for future work to consider the synergy between collapsibility and flexibility in exploring granular dynamics in group structure. There is interest in differentiating ROIs which undergo changes in group assignment and high nQ variability, indicating high dynamic activity with changes in both group involvement and importance. These ROIs may give insight into novel nodal dynamics which have been left unstudied, and are not accessible with flexibility or collapsibility on their own. In this case, it may be beneficial to adjust the calculation of collapsibility to count nQ variability in sequential layers rather than over total layer pairs as was done in this study. Additionally, it is not well known how to choose the collapsibility threshold. In this study we based our choice of collapsibility threshold on results from our SBTM surrogate networks, but future studies may want to consider exploring the parameter in larger and more diverse datasets to find an appropriate choice for understanding early stage AD. Lastly, Chapter 3 emphasized the importance of nQ,

not only to network neuroscience, but to other disciplines where modularity is a hallmark of organization. The methods presented in this chapter expand on these results by providing methodological considerations for the use of nQ in large networks (in network neuroscience and beyond) and a novel measure of nQ variability to improve interpretation.

Chapter 5

Targeted attacks on occipital-frontal functional connections simulates AD progression for a visual short-term memory binding task

5.1 Introduction

It has been well established that Alzheimer's disease (AD) damages functional brain networks [20, 248]. In prior chapters, we explored this in more detail through novel measures of granular community structure and how these can be used to characterize early stage AD. However, the mechanisms in which changes to functional connectivity occur is not well understood. In this chapter we explore methods of attacking networks to simulate damage associated with AD.

In network science, targeted attack strategies are often used to assess network vulnerability through the removal or reduction of nodes and/or edges. For instance, targeted attack-based methods are used to identify candidates for vaccination to minimize disease spread [249, 250, 251] or to assess power grid vulnerabilities that could lead to cascade failures [252, 206]. Similar approaches have been applied to brain networks, where targeted attack methods simulate disease progression by iteratively removing or degrading key functional connections or brain regions, allowing for the testing of hypotheses around network degeneration associated with AD. For instance, Stam *et al.* [125] explored iterative targeted attacks between high degree (hub) nodes in rs-MEG under the hypothesis that these influential brain regions would be more susceptible to damage as a result of AD. They found that preferentially targetting these specific edges better explained the loss of functional connectivity due to AD than random attacks, suggesting a disruption of the brain's small-world architecture towards random. Similarly, this behaviour is seen in resting state functional magnetic resonance imaging (rs-fMRI) [167], whereby targeting hub nodes in addition to adding random edges resulted in a loss of small-worldness and simulated AD disease progression.

However, targeted attacks research in neuroimaging for AD remains limited with the following studies relating to the bulk of the research [169, 125, 167, 253, 168]. This research has primarily focused on attacks on high-degree hub nodes. However, node degree is a local measure which does not consider the more complex (secondary, tertiary, etc.) functional interactions which are important to group structure. It remains an open question whether node degree is the optimal measure for targeted attack models in simulating AD progression. This is especially relevant given that, while AD seems to preferentially target hub nodes, this is more heavily weighted to long-range connections [254, 255]. Lastly, to our knowledge, no study has explored targeted attack models in task-fMRI.

For this purpose, we explored a variety of targeted attack models in fMRI networks of the visual short-term memory binding task (VSTMBT) to determine whether previous models extend to task-based fMRI in an earlier stage of AD – MCI converters. Additionally, we introduce several novel targeted attack models of AD based on distance and nQ, exploring whether nQ is an improved measure for targeted attacks in this setting, and whether distance based restrictions improve model performance.

The contributions of this chapter are:

- Examining whether prior targeted attack methods extend to task-fMRI networks in an earlier stage of AD and whether nQ improves the targeting in this setting.
- Introduction of a novel, brain lobe-based targeted attack model, which improves on prior models in simulating AD and showing that this effect is not driven by Euclidean distance alone.
- Introduction of a second novel targeted attack model which combines lobe-based and nQ-based targeting which also improves on prior models in simulating AD.

5.2 Materials and Methods

5.2.1 Participants

Participants for this study were taken from the same VSTMBT-fMRI cohort described in Chapter 3, Section 3.2.1. As a brief summary, this longitudinal study consisted of healthy subjects and those with several stages of MCI – eMCI, MCI and MCI converters (those that converted to AD after a 2-year follow up). These subjects underwent fMRI scanning during which they performed the VSTMBT as in Fig. 3.1.

In this study, we explore targeted attack models inspired by Stam *et al.* [125], which require an overall decrease in network edge weight. Given this, we only explore the healthy subjects and those with MCI which converted to AD given that earlier stages of AD did not experience as consistent a loss in network edge weight. In addition, only 5 of the healthy participants

(of 8) had high enough average network edge weight such that the targeted attack models discussed in the following Sections 5.2.3 and 5.2.4 were feasible. Thus, these 5 healthy subjects (Age:75.4±4.7, Sex:1M;4F) and the 6 MCI converters (Age:76.3±5.1, Sex:4M;2F) were used for this pilot study.

5.2.2 fMRI pre-processing and network construction

fMRI pre-processing and network construction follows from Chapter 3. That is, each subject has two 85×85 functional connectivity matrices constructed using Spearman correlation between each brain region's fMRI signal across repetitions of the encmaint and probe phases of the task. However, note that in this chapter the networks constructed from encmaint and probe phases of the task are explored separately and not in a multiplex construction as previously.

5.2.3 Benchmark attack models

Here, we introduce the benchmark attack models which we use to compare our novel model performance to. Specifically, we use three main models as benchmarks – a random attack model and the same targeted attack model adapted from [256] and introduced in neuroimaging studies by Stam *et al.* [125], and a Euclidean distance-based attack model.

The random attack model assumes that network changes due to AD are as a result of random decreases in network edge strength [125]. That is, for each healthy subject, we iteratively reduce an edge in the network (encmaint and probe networks explored separately) by a factor of two at random until the average network edge weight is equal to the average network edge weight of our MCI converters (calculated *a priori*). See Fig. 5.1a for a visualization of this process.

The targeted attack model is based off of the hypothesis that high degree (hub) nodes are preferentially targeted in AD [125]. For each healthy subject, we follow two steps. 1) We calculate the degree of each node in the network (see section 2.3.5 for detail). 2) We then choose an edge with a probability based on the summed degree of the two nodes connecting it and reduce it by a factor of two. These two steps are repeated iteratively until the average network edge weight is the same as the average of the network edge weight of our MCI converters. This process can be visualized in Fig. 5.1b.

The Euclidean distance-based model assumes that longer-range connections are preferentially targeted in AD. It was implemented given observations that long range connections in fMRI are preferentially damaged in AD [255, 254]. It follows a similar two-step iterative approach as the targeted attack model, but where the probability of an edge being selected to be reduced is based on the Euclidean distance between the two nodes (longer-range connections are preferentially reduced). See Fig. 5.1c for more detail.

Thus, for each healthy subject we have a simulated network of disease progression for each of the above attack models for both the encmaint and probe phases of the task.

5.2.4 Lobe and nQ-based targeted attacks

Here, we introduce three novel attack models – nQ-based targeted attacks, lobe-based with a focus on occipital and frontal lobes, and this same model with the addition of nQ instead of degree to determine hub nodes.

First, we determine whether attacks based on nQ improve model performance in comparison to hub nodes. Next, we hypothesized that Euclidean distance alone would not explain network edge weight differences due to AD, specifically given variations seen in [254, 255]. Instead, we explored the extent of disconnection between hub nodes in four major brain lobes – frontal, parietal, occipital, and temporal lobes. In addition, we hypothesized that connections between the occipital and frontal regions and the rest of the brain would be particularly of interest given large increases in nQ that were seen in ROIs in these lobes in Chapter 3, which could indicate a functional segregation of these lobes with the rest of the brain network, and especially given the importance of these ROIs to visual memory binding.

As such, we begin by defining the *targeted* nQ attack model as an extension of the targeted attack model in the prior section. It follows a similar two-step iterative process where first we calculate the nQ of each node in the network (see Eq. 3.3 in Section 3.2.6 for detail). Then, we choose an edge probabilistically based on the summed nQ of the two connecting nodes and reduce it by a factor of two. This is repeated iteratively until the average network edge weight is the same as the average network edge weight of our MCI converters, as seen in Fig. 5.1d. The calculations of modularity, and subsequently nQ, follow from methodology on modularity maximisation given in Section 3.2.7. Note that modularity and nQ calculations are done with 10 iterations (rather than 100 as in Chapter 3) as nQ is recalculated after each edge is reduced in the targeted nQ model. This results in a high computational time and, given the probabilistic selection of edges, slight variations in modularity calculation are not expected to lead to an appreciable change in simulated network outcome. This methodology is used for all subsequent calculations of modularity and nQ.

Next, we introduce a novel simulation model, *targeted OF*, with four pre-defined lobes and the rest of the ROIs grouped separately. These lobes include the four standard cerebral lobes (frontal, parietal, temporal and occipital lobes) and where the fifth, insular lobe, is coupled with the other remaining ROIs in the atlas [257]. See Table 5.1 for which ROIs are included in each group and note that we use more recent definitions of the temporal lobe which include key ROIs important to memory such as the hippocampus and amygdala [258, 259]. This model consists of attacking the network with a probabilistic approach on the edges in the following groups: occipital to frontal (OF), occipital to parietal or temporal (OPT), frontal to parietal or temporal (FPT), and all other remaining edges (AO).

Table 5.1: ROIs in each group. Here we show the 85 ROIs of the modified Desikan atlas introduced in Section 3.2.3 and their lobe-based groupings. The 47 entries in the table each correspond to a distinct anatomical region where all but the brain-stem are defined per hemisphere, totalling 85 ROIs.

Lobe	ROIs
Frontal	caudalanteriorcingulate, caudalmiddlefrontal, lateralorbitofrontal, medialorbitofrontal, paracentral, parsopercularis, parsorbitalis, parstriangularis, precentral, rostralanteriorcingulate, rostralmiddlefrontal, superiorfrontal, frontalpole, insula
Parietal	inferiorparietal, postcentral, posteriorcingulate, precuneus, superiorparietal, supramarginal
Occipital	cuneus, fusiform, lateraloccipital, lingual, pericalcarine
Temporal	hippocampus, amygdala, bankssts, entorhinal, inferiortemporal, isthmuscingulate, middletemporal, parahippocampal, superiortemporal, temporalpole, transversetemporal
Other	thalamus, caudate, putamen, pallidum, brain-stem, accumbens-area, ventralDC,

Using these groups, we first define a set of probabilities which control which between-lobe edge group we are attacking. Subsequently, we pick an edge from this set preferentially targeting high degree nodes and reduce it by a factor of 2. Then, as before, we check if the average network edge weight is equal to that of the average MCI converter network. If not, this process is repeated iteratively by first choosing the between-lobe edge set, reducing an edge between high degree nodes, and comparing to the MCI converter network. A visualization of this process can be seen in Fig. 5.1e. Additionally, we explore this model's performance across a range of probability sets to determine whether preferentially targeting edges between specific lobes improves model performance.

The second novel attack model, *targeted OF with* nQ, proceeds in a similar manner as the targeted OF model but where probabilities of choosing an edge are based on nQ. That is, first a between-lobe edge set is chosen based on a list of predefined probabilities. Next, an edge is selected based on the summed nQ between the two nodes and reduced by a factor of 2. Lastly, the network average edge weight is compared to that of the average network edge weight of the MCI converters network. This process is then repeated until the simulated network has the same average network edge weight as the MCI converters network. A visualization of this process is given in Fig. 5.1f.

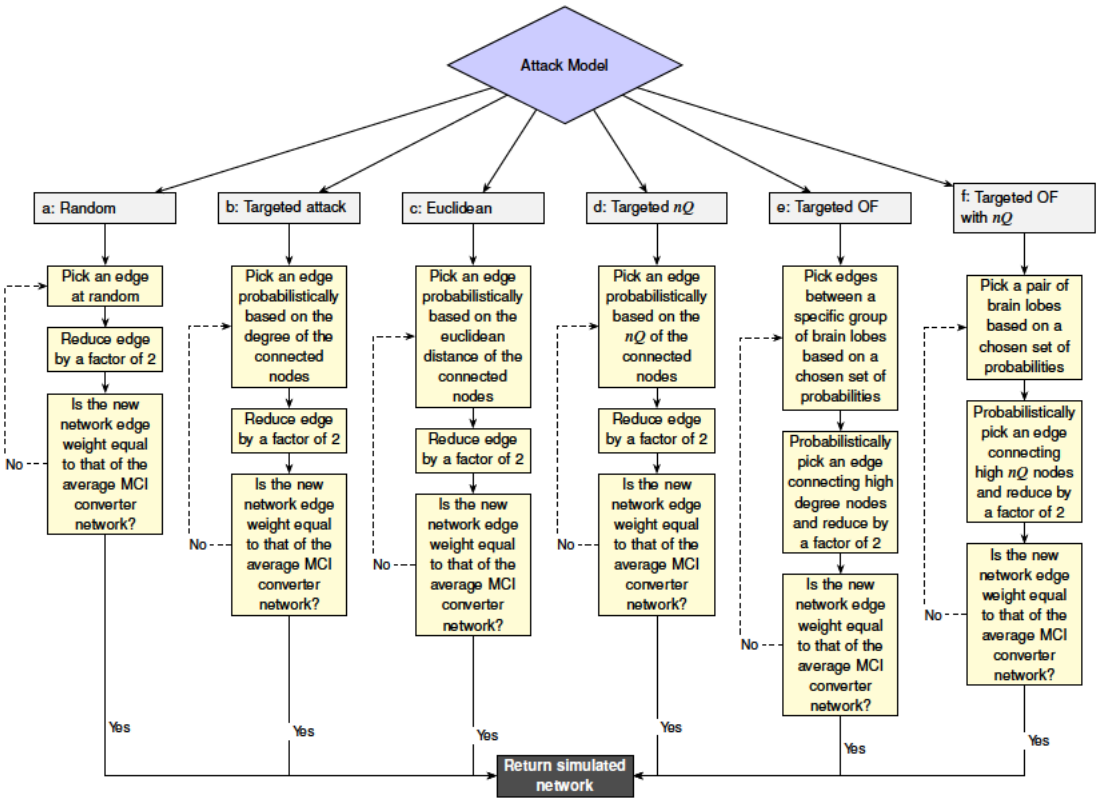

Figure 5.1: Attack models to simulate MCI converters. Here we visualize the six attack models used in this study. Each model follows an iterative attack method on edges in the networks of the healthy subjects until the average network edge weight is the same as that of the average network edge weight of the MCI converters. The method of choosing which edges to target changes with each model. a) edges are attacked at random. b) edges are attacked probabilistically between high degree ROIs. c) edges are attacked between ROIs which are distant (euclidean distance). d) edges are attacked between ROIs with high nQ. e) a between-lobe edge group is selected first (probabilistically), then an edge is attacked between high degree nodes. f) a between-lobe edge group is first selected, followed by an attack between high nQ nodes.

5.2.5 Network analysis

In this section, we outline the network measures used to compare features of network topology between our healthy, MCI converters, and attack model simulated networks. Specifically, we use the single-layer metrics of degree, clustering coefficient, modularity, path length, and eccentricity introduced in Sections 2.3.5, 2.3.6, 2.3.9, and 2.3.8, respectively. Note that all network metrics other than modularity and nQ were calculated with the Brain Connectivity Toolbox [103].

We calculate these network measures in healthy subjects, MCI converters, and in simulated networks obtained from the five attack models described in the prior two sections (for both encoding and probe networks). To compare clustering coefficient, path length, and eccentricity across the networks, we normalise these values by adapting the methodology by Stam *et al.* [125]. Specifically, we calculate the mean clustering coefficient, $\widehat{C_m} = C_m / \langle C_m^{surrogate} \rangle$, mean path length, $\widehat{PL_m} = PL_m / \langle PL_m^{surrogate} \rangle$, and mean eccentricity, $\widehat{e_m} = e_m / \langle e_m^{surrogate} \rangle$. Here, $\langle C_m^{surrogate} \rangle$, $\langle PL_m^{surrogate} \rangle$, and $\langle e_m^{surrogate} \rangle$, denote the clustering coefficient, path length, and eccentricity, averaged over an ensemble of 50 surrogate networks obtained from randomly shuffling the edge weights of the original network (m, which is all five simulation models, control, and MCI converter networks). Note that we do not complete this step for modularity as comparison to a random null-model is inherent within its calculation. The distribution of these network measures are used to compare controls and MCI converters to the simulated network models for the encoding and probe phases of the VSTMBT.

5.3 Results

In this section we explore the effectiveness of three novel simulation models, targeted nQ, targeted OF and targeted OF with nQ, at simulating MCI converters in VSTMBT-fMRI data.

5.3.1 Lobe-based targeted attacks

Initially, we compare the distributions of clustering coefficient, path length, eccentricity, and modularity across our controls, MCI converters, and the targeted OF simulated networks for a range of probabilities on the various between-lobe edge sets (OF, OPT, FPT, and AO). We start with only attacks on AO, gradually decreasing these while increasing attacks on long-range OF connections for encoding and probe networks, Fig. 5.2 and 5.3. This was done to determine what between-lobe attacks resulted in the best performance to then compare to our other attack models.

For the encoding networks, and as we increase the attacks on OF connections, we see increases in clustering coefficient which closely matches that of our MCI converters group as in Fig. 5.2a. Path length also increases with increasing attacks on OF connections, approaching MCI converter, but differs significantly from the MCI converter networks (see Fig. 5.2b). A similar increasing trend is seen in modularity, but note that while the mean approaches that of the MCI converters group with increasing attacks on OF connections, that the distribution of the MCI converters is large as seen in Fig. 5.2c. On the other hand, node eccentricity is closest for [OF=0.2, OPT=0.1, FPT=0.1, AO=0.6], suggesting that while path length is increasing in general, that some of the long-range OF connections have been over corrected for.

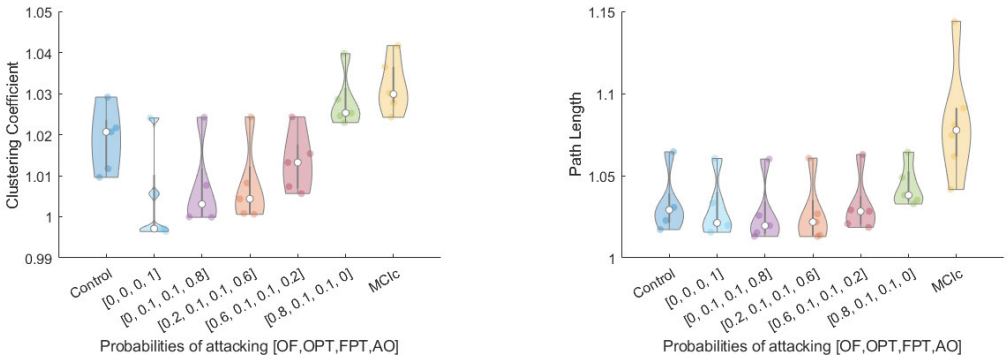

(a) Clustering coefficient.

(b) Path length.

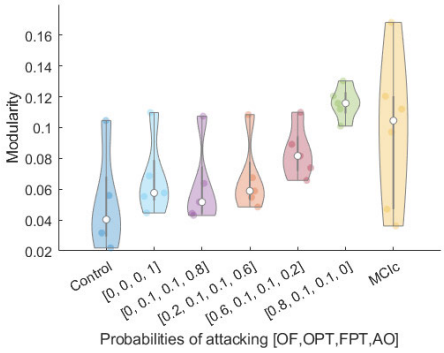

(c) Modularity.

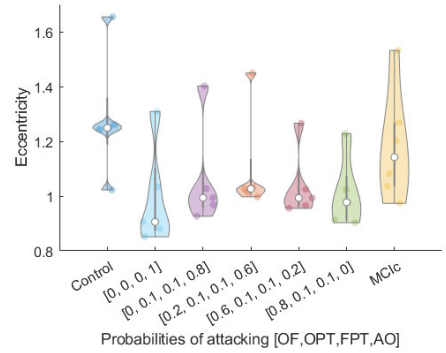

(d) Eccentricity.

Figure 5.2: Targeted OF attack model for a range of chosen probabilities in encmaint. Here we show the performance of the targeted OF attack model as targeted attacks on OF connections increase. As these OF connections are attacked with higher probability, the clustering coefficient (a) and modularity (c) of the simulated network approaches that of the MCI converters. Path length also trends towards the MCI converters but not appreciably (b). Lastly, eccentricity begins to decrease with increased attacks on OF suggesting that some long distance paths have been over corrected in these models (d).

In the probe networks we see a similar result. Clustering coefficient in the simulated networks closely matches that of the MCI converters as attacks on long-range OF connections increases. This can also be seen for the mean of modularity, though note the wide distribution in the MCI converters in Fig. 5.3c. Path length also increases with increasing attacks on OF but underperforms as with the encoding networks (see Fig. 5.3b). Lastly, eccentricity also most closely matches for [OF=0.2, OPT=0.1, FPT=0.1, AO=0.6] as seen in Fig. 5.3.

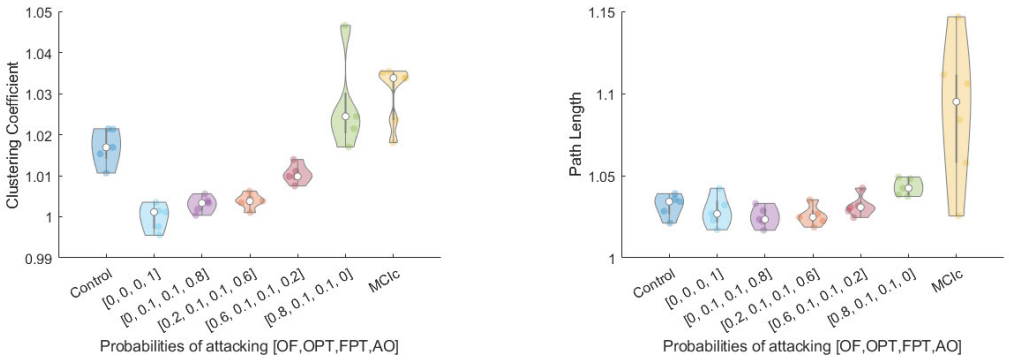

(a) Clustering coefficient.

(b) Path length.

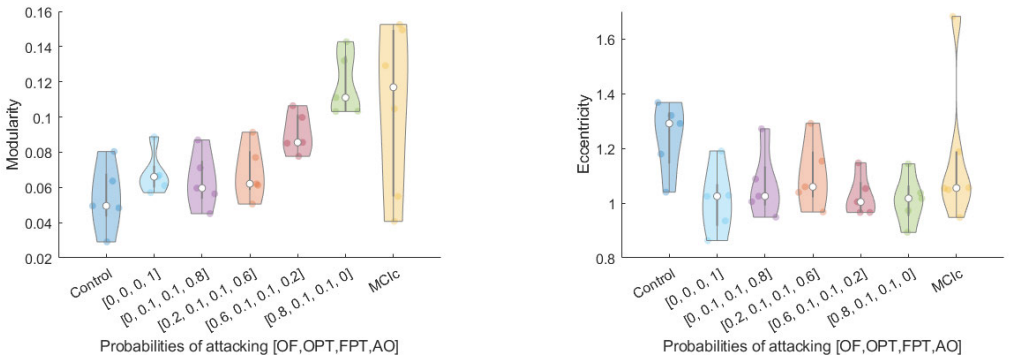

(c) Modularity.

(d) Eccentricity.

Figure 5.3: Targeted OF attack model for a range of chosen probabilities in probe. We visualize the targeted OF model with an increasing probability of attacking OF connections. As we increase attacks on OF, and similar to the encoding results, we find that clustering coefficient (a) and modularity (b) more closely match our MCI converters than the other models. However, note that while mean is well expressed, the MCI converters have a wide distribution of modularity in these networks covering all models. As before, path length trends upward with increased attacks on OF connections though not appreciably (b). In the case of eccentricity, there is a large overlap between all initial probability sets which does not appreciably change with increases in attacks on OF connections (d).

In sum, across the four metrics, the targeted OF model performs best when attacks are more heavily weighted toward OF connections.

5.3.2 Comparisons between all network models

Here, we compare all of our simulation models in the encoding and probe networks – random, targeted, euclidean, targeted OF, and targeted OF with nQ. For the targeted OF and targeted OF with nQ models, we choose a lobe-based probability set of [OF=0.8, OPT=0.1, FPT=0.1, AO=0] given its performance in the previous section.

First, we explore the encoding networks. For clustering coefficient, we find that the random, Euclidean and targeted nQ attack models yield no appreciable change, while the original targeted attack model performs the worst. Targeted OF and targeted Of with nQ models perform the best with the nQ-based attack model improving slightly on the OF model. See Fig. 5.4a for more detail. For path length, the original targeted attack model performs the worst with all other models performing similarly and about as good as random (Fig. 5.4b). The targeted OF with nQ model performs slightly better but not appreciably. It's important to note the poor performance in path length across all models. On the other hand, node eccentricity varies much more from model to model with the random, targeted, targeted nQ, and Euclidean models performing better than the targeted Of and OF with nQ models as seen in Fig. 5.4d. This suggests that lobe-based targeting may be over correcting the longest distance connections. Lastly, the performance of the random, targeted, targeted nQ and euclidean models are poor in modularity while targeted OF, and more specifically targeted OF with nQ, perform similarly in capturing the mean modularity of the MCI converters. See Fig. 5.4c for more detail. Additionally, it is important to note the poor performance of the original targeted attack model and the contrast between the two OF models and euclidean distance model in clustering coefficient and modularity specifically. This will be discussed in the following section.

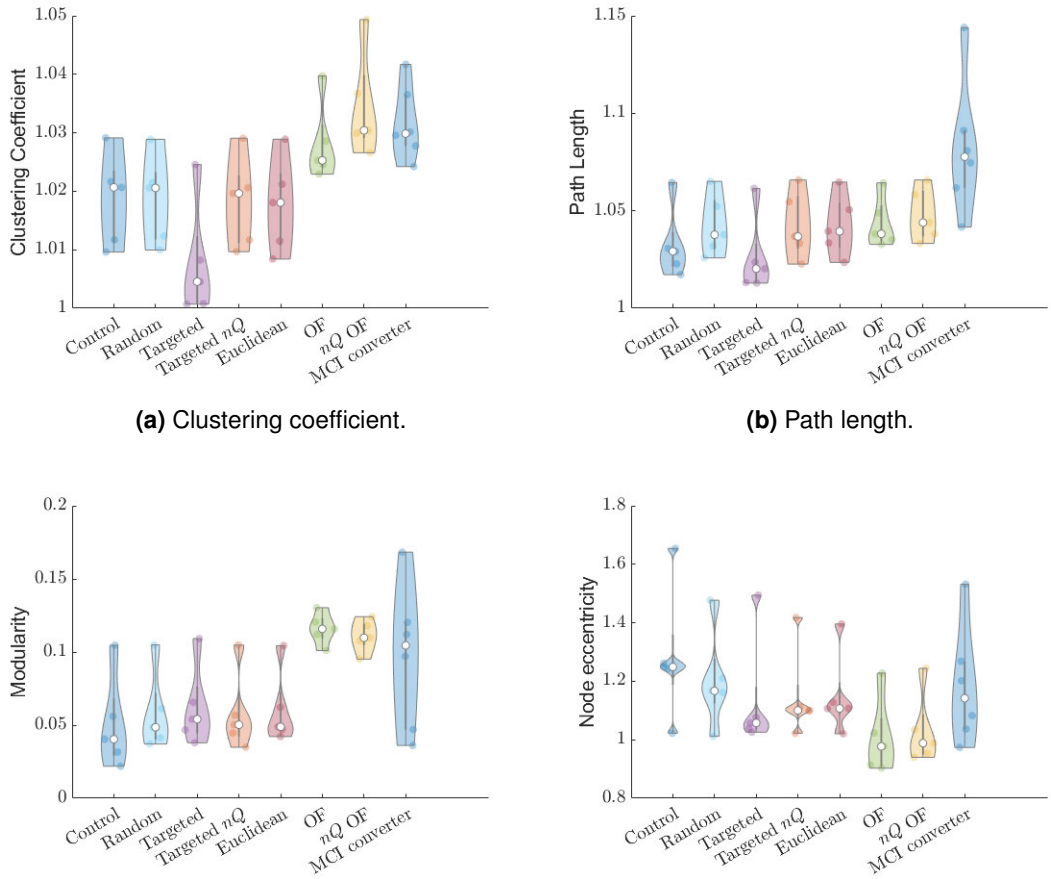

(a) Clustering coefficient.

(b) Path length.

(c) Modularity.

(d) Eccentricity

Figure 5.4: Comparison of attack models for the encmaint networks. Here we show the six attack models in comparison to control and MCI converter networks for each of our network measures. a) For clustering coefficient, we see the targeted attack model perform the worst while the targeted OF (OF) and targeted OF with nQ models (nQ OF) perform best. b) The path length is poorly expressed across all simulation models. c) Modularity is expressed similarly in the random, targeted, targeted nQ and Euclidean models, while OF and nQ OF more closely match the mean Modularity. d) The eccentricity on the other hand shows poor performance in OF and nQ OF models and where euclidean and random models perform best.

For our probe networks we see a similar result. Clustering coefficient performance in the original targeted attack model is very poor while targeting based on euclidean distance and nQ performs about the same as random (see Fig. 5.5a). On the other hand, performance is improved in the targeted OF model and further improved with the addition of nQ. As before, path length is poorly expressed in all attack models but with the poorest performance in the original targeted attack model as seen in Fig. 5.5b. However, the targeted OF and OF with nQ

attack models perform best in expressing the eccentricity of the MCI converters network along with the targeted attack model (see Fig. 5.5d). Similarly to our encoding networks, modularity is expressed best in the target OF and slightly better in the targeted OF with nQ models while the others perform about as well as random. See Fig. 5.5c.

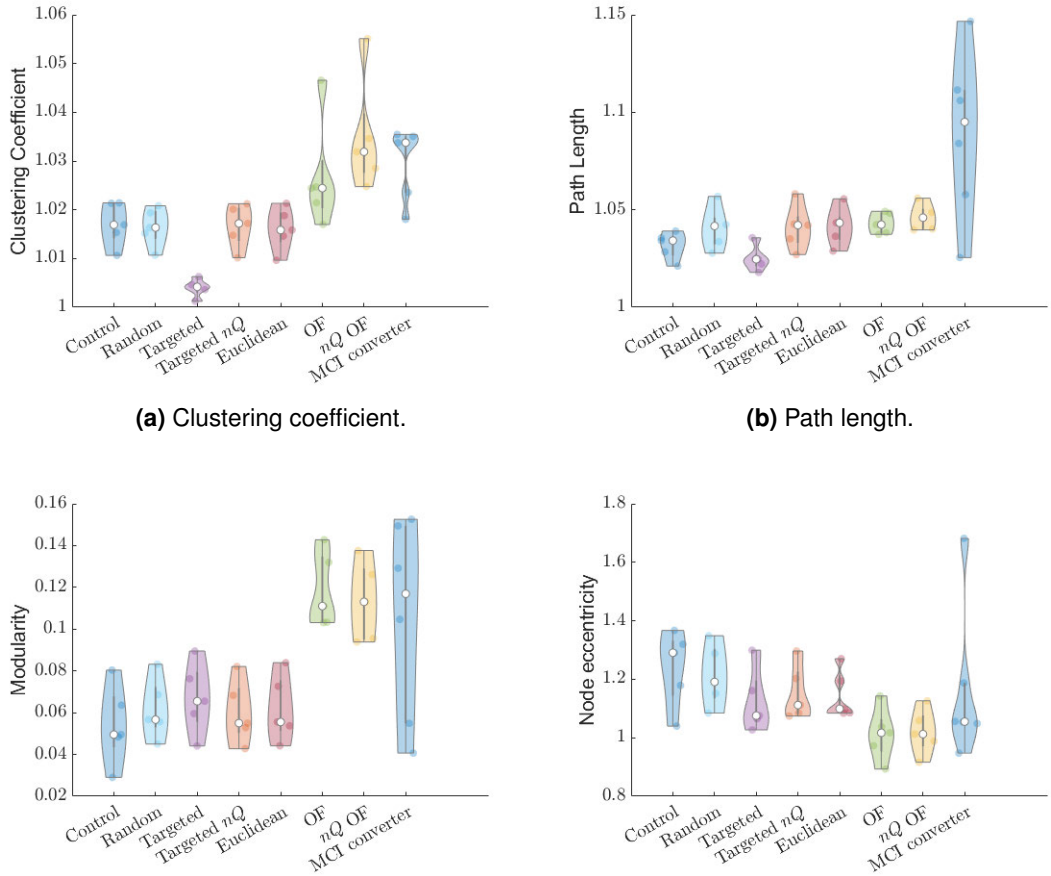

(a) Clustering coefficient.

(b) Path length.

(c) Modularity.

(d) Eccentricity.

Figure 5.5: Attack Models Probe. Here we show the performance of the six attack models in comparison to controls and those with late-stage MCI (MCI converters). Results remain largely similar to the encoding networks with the OF and nQ OF models performing best in clustering coefficient (a) and modularity (c). Path length is poorly expressed across all models (b), and unlike the encoding networks, the eccentricity is best in the OF and nQ OF models (d).

In sum, and across encoding and probe phases of the VSTMBT, the targeted OF model performs better than the original targeted attack model at expressing the clustering coefficient and modularity of the MCI converter networks. This is further improved in the targeted OF with nQ model. This same performance is not seen in path length, though performance was poor across all models, and the associated results in eccentricity suggest that some long-range connections could be over corrected.

5.4 Discussion

This section explores the performance of a collection of benchmark and novel simulation models of the progression from healthy to late-stage MCI (MCI converters).

5.4.1 Extension of targeted attack models to VSTMBT-fMRI

Targeted attack models have been used to understand the high-level mechanisms of functional and structural brain organization. Predominantly, it has been found in studies of MEG, fMRI, EEG, and DTI that connections between hub nodes are preferentially targeted in AD [169, 125, 167, 253, 168]. However, while prior evidence has shown promise in simulating AD progression with the targeted attack model in rs-fMRI [167], task-fMRI has not yet been explored. Furthermore, prior research explored control to AD and MCI conversion only. We questioned whether these methods would extend to task-fMRI and in later stage MCI (MCI converters). For this purpose, we employed the popular targeted attack model introduced by Stam *et al.* [125], which preferentially attacks these hub nodes to VSTMBT-fMRI. We found that network metrics of the simulated networks were substantially different from that of the MCI converters, and especially the case in clustering coefficient in both phases of the VSTMBT (encoding and probe). This suggests that hub node vulnerability may not describe the effects of late-stage MCI and/or changes in task-specific functional connectivity unique to the VSTMBT.

To tackle this, we wanted to test whether changes in targeting based on a different measure of node influence (nQ rather than degree) would provide an improvement in the simulated networks. nQ has been shown to be sensitive to AD in both MCI converters in fMRI and EEG (Chapters 3 and 4), and that modularity as a metric has been shown to be sensitive across the stages of disease in fMRI [20]. However, we found that targeting based on nQ alone was not appreciably different from random attacks or those based on euclidean distance. However, it did not experience the same drop in performance that the targeted attack model did in clustering coefficient.

In sum, neither the popular degree-based targeted attack model nor that based on nQ effectively described the changes in the VSTMBT-fMRI networks of MCI converters. Whether this effect is due to task-based network structure or differences in early-stage AD is uncertain and requires further research.

5.4.2 Attacks on occipital-frontal functional connectivity

An observation in Chapter 3 was that changes in nQ as a result of MCI converting to AD were largely composed of increases in modularity in frontal and occipital regions of the brain and consistent with AD progression pathways and ROI involvement in the VSTMBT. These increases in nQ can indicate a functional segregation or specialization as a result of damage, reflecting an inhibited communication between brain functional networks (i.e., decreased correspondence between systems involved in visual processing and working memory). To capture the potential disconnection between these two systems, we hypothesized that restricted attacks targeting connections between brain functional sub-networks would lead to improved simulation performance.

As such, we introduced two novel targeted attack models centred on increased attacks on occipital-frontal lobe connectivity. We found that increased attacks on functional connectivity between these specific networks resulted in marked improvement in two network measures which describe network organization (clustering coefficient and modularity). This suggests that brain organizational-based changes in connectivity may be driven by disconnections between these two systems specifically. Prior research has shown that long-distance connections (i.e., those between occipital and frontal regions) are damaged in MCI, early-AD, and AD in rs-fMRI [255, 254]. Interestingly, while prior research found that these decreases in functional connectivity were Euclidean distance dependent in early-AD [254], we found that lobe-based attacks heavily outperformed the euclidean distance model. This discrepancy may be explained by the task-specific demands of visual short-term memory binding. The VSTMBT requires integration of occipital regions which underpin the retention of visually bound features (i.e., coloured shapes) in conjunction with frontal regions as part of the working memory network of the brain [69, 77, 260, 261, 262]. The improved performance in clustering coefficient and modularity were seen in both targeted OF and targeted OF with nQ models. However, it should be noted that while performance was similar, targeting based on nQ improved performance slightly. This could suggest that a modular approach to attacking brain networks, by first selecting between-group edges to target, may benefit from subsequent targeting based on nodal contributions to modular group structure. It is of interest to extend these methods to more refined functional network groupings (such as DMN, attentional, salience, etc.) to see if similar results are observed. For instance, by specifically targeting occipital-frontal disconnection in the DMN which has been observed in rs-fMRI [255].

It is important to note the generally poor performance in path length across all models. While those based on OF connections trended towards the measurements of path length in the MCI converters, the path lengths remained low. Prior research has also found difficulties in modelling changes in path length between controls and AD [125, 167]. In the present study, brain ROIs were grouped based on lobe-assignment which is limited in its complexity. Models

which consider finer groupings (such as the inclusion of DMN, attentional, salience networks, etc.) may observe an increased average path length connecting nodes within group to all others. In addition, the decreased eccentricity suggests that some of the longest paths in the network have been over corrected in the OF models.

Additionally, the wide distribution of the network measure results in our MCI converters is a limitation. Given that AD varies at the individual level, and that AD-subtyping is becoming more prevalent [200], per-subject trajectories could be possible by varying attacks between different functional networks. While this was not able to be tested in this research given sample size restrictions, future research should explore how varying attacks between different functional sub-networks (perhaps informed by subject-specific task performance, or a priori exploration of nQ), can test subject-specific AD trajectories. Additionally, a limitation of the attack models proposed in this research is that they operate under the assumption that the average network edge weight decreases from healthy to disease. While this is generally observed in network-based studies of AD [125, 167, 168], some of our healthy controls had to be omitted from the study given that their initial network edge weights were below that of our MCI converters. This could be due to the early stage of AD that we are exploring, where network-based effects have yet to have a large enough effect. In addition, further exploration of AD-subtypes may result in separate simulation targets for individual healthy controls and thus overcoming the issue mentioned earlier.

It is important to mention that more complex simulation models exist for AD. For instance, The Virtual Brain (TVB) is a multimodal simulation method of the human brain which can estimate functional activity such as EEG, fMRI, and MEG from a subject's structural MRI and connectivity (i.e., structural MRI and DTI) [263]. The integration of these imaging modalities can allow for the exploration of simulated connectivity networks and an estimation of the excitatory/inhibitory (E/I) balance of neurons in the brain which have been shown to capture disease-specific alterations in AD [264, 265]. The simulation models presented in this chapter are complimentary to more complex methods like TVB by providing an easily interpretable and computationally fast way of probing and testing hypotheses in the simulation of AD progression (which can then be further refined in TVB-based simulations). The nQ-based simulation methods scale linearly with the number of edges (m) in the network $O(m \cdot I \cdot J)$, where I is the number of iterations until convergence in the iterated version of the GenLouvain method (typically only a few), and J is the number of attacks before the target average edge weight is reached. In the case of the lobe-based targeted attack method on node hubs (degree-based), the computational time is $O(m \cdot J)$.

5.5 Conclusion

Previous chapters of this thesis introduced nQ as a method of quantifying granular changes in modular community structure for use in single and multiplex networks, and in applications of nQ to neuroimaging data of early stage AD where modularity is known to be affected. In Chapter 3, we found significant increases in nQ between controls and those with MCI which converted to AD centred on occipital and frontal regions of the brain. It was natural to question what mechanisms lead to these changes in nQ in the VSTMBT-fMRI networks. One method to accomplish this is through simulated attack models which test hypotheses in how AD affects brain networks by reducing edges in healthy networks to simulate damage due to disease.

We found that previous methods in targeted attacks, which focus on attacking edges between hub nodes (high degree), did not extend to VSTMBT-fMRI networks. As such, we explored whether targeted attacks between nodes with high nQ would improve performance. However, we found that results in this model performed about as well as our benchmarks. Given observations of increased nQ in occipital and frontal lobes in Chapter 3, we introduced two novel lobe-based attack models (targeted OF and targeted OF with nQ) which perform particularly well at capturing changes in network organization due to early-stage AD (MCI converters). However, like in prior studies, the models do not perform well in capturing network path length of the MCI converters. This may suggest that further refinement of the lobe-based attacks into typical brain sub-networks such as the DMN is needed. This proposed methodology also assists in the analysis of subject-specific trajectories of AD by allowing for specific between-subnetwork attacks to be tuned based on subject-specific task performance deficits, or by taking into account AD-subtypes and the networks they primarily effect.

The proposed targeted attack models serve as a way to capture connectivity changes specific to the VSTMBT in early AD. Though limited by sample size, it motivates further research in how we can assess the mechanisms of AD progression. Namely, a refinement of attacks to incorporate further biological or imaging-related disease mechanisms, and extensions of targeted attack methods to other imaging modalities like task-EEG.

Chapter 6

Thesis Discussion, Limitations, and Future Work

6.1 Thesis Discussion

This thesis focused on the application of granular network measures and models to Alzheimer's disease (AD), the leading cause of dementia, along with prodromal stages of the disease (amnestic mild cognitive impairment, aMCI) [4, 5]. Prior research combining biological biomarkers, neuropsychological tests, and genetic risk markers have contributed to accurate methods of defining the stages of AD and in pinpointing its progression with high accuracy [9, 10]. However, these methods are often costly, biased to the global north, and much is still unknown given that AD varies significantly at the individual level [49]. This motivates the development of novel methods of exploring AD, especially those sensitive to the early-stages of AD where less damage has been done, and those that are cheaply applicable and verified in diverse populations (i.e., the visual short-term memory binding task – VSTMBT). For this purpose, this thesis aimed to advance the current methods of modelling and analysing human brain networks to improve our understanding of AD. Novel network measures and models for the analysis of single and multiplex networks were introduced, along with applications to multiple types of neuroimaging data of MCI and early-AD in Chapters 3, 4, and 5. Along with exploring the early-stages of AD, this thesis focused on applying these methods to the VSTMBT, to provide further evidence of its sensitivity to early AD, along with application of these methods in cheaper acquisition methods (EEG) and across diverse cohorts (data from Scotland and Southern Colombia).

In Chapter 3 we introduced a novel extension of modularity, nodal modularity (nQ), from a global measure of brain organization to individual, per ROI, contributions. This measure provided novel insights into brain organization in comparison to other commonly used nodal graph measures. It was hypothesized that nQ would illuminate subtle changes in network organization which is known to be affected across the stages of AD [20]. Our results confirmed this hypothesis, whereby nQ explored in both single layer DTI and multiplex, temporal, task-fMRI for a VSTMBT showed marked differences in a key turning point of AD – MCI converters. Additionally, the results showed that this effect was only observed for the binding task and not

shape, agreeing with known sensitivity of the binding task to early-AD [29]. Furthermore, the ROIs detected in this study agreed with common biomarkers of the disease, amyloid-β and tau, in VSTMBT-fMRI, and where DTI results agreed with previously understood changes in white matter integrity in poor memory binders [149].

In Chapter 4, we expanded on the introduction of nQ in Chapter 3. Specifically, we explored nQ in large multiplex surrogate networks of a typical size used in neuroimaging and showed that nQ maintained its novel behaviour in comparison to other typical measures of multiplex node influence. Additionally, we provided a novel aggregate measure of nQ, *collapsibility*, and found that it was also distinct from its most comparable measure of node flexibility. We explored nQ and collapsibility in multiplex frequency networks of EEG during the VSTMBT in subjects with MCI. We found that large changes in nQ and collapsibility were mostly seen in the binding task and not in shape, consistent with our previous fMRI findings, and with the known sensitivity of the binding task to MCI [29]. These changes were consistent with augmented grey matter observed in MCI and changes in functional connectivity around the thalamus [231, 232, 234, 235, 236]. Furthermore, changes in nQ were only observed in the delta band which may reflect a hallmark of AD in EEG, the shift in power spectra from higher to lower frequencies [228, 229, 230].

In Chapter 5, we introduced three novel targeted attack models for the simulation of healthy to MCI converter progression in VSTMBT-fMRI. For this purpose, we explored several benchmark attack models and a popular attack model which targets node hubs. We found that these models did not express the changes in network organization that occur in early-AD in task-fMRI. In addition, one of the proposed targeted attack models on nodes with high nQ also performed about as well as our benchmark models. As such, we proposed two additional novel targeted attack models, targeted OF and targeted OF with nQ, which attack edges connecting brain lobes. We found that increased attacks on occipital-frontal connections resulted in much improved performance in capturing changes in brain organization due to early-AD, and is consistent with the task-specific demands of the VSTMBT.

Prior evidence has suggested that the VSTMBT may be a pre-clinical marker of AD. This was due to correlates between impaired short-term memory binding performance in preclinical familial and early-stage sporadic AD [29, 56] and with amyloid-β deposition [67, 68]. In addition, tasks which target short-term memory binding are especially important for AD given that they remain relatively unchanged with age while being highly sensitive to the disease [29]. This sensitivity is specific to AD where conjunctive short-term memory binding (i.e., between colour and shape) is impaired as opposed to other, non-AD, dementias where this effect is not observed [66]. The research presented in this thesis in Chapters 3, 4, and 5 provide further evidence to support the VSTMBT as a cognitive biomarker of AD.

Specifically, this thesis presents the first network-based analysis of VSTMBT-fMRI data and the first multiplex network analysis of VSTMBT-EEG data. In these chapters, we consistently saw significant results in the binding task and not shape, consistent with the known behaviour of the VSTMBT, in addition to statistically significant regional changes in specific ROIs connected to early-AD and/or important to memory binding, and how these changes evolve from healthy to early-AD. Furthermore, these results are further supported by co-authored research exploring graph-based permutation patterns of VSTMBT-fMRI signals on DTI networks (the same data as used in Chapters 3 and 5), which revealed changes in the binding task in ROIs across the stages of early-AD [78, 79]. More specifically, this novel method evaluates VSTMBT-fMRI signals at each node in the DTI structural network offering a powerful way to explore the interplay of brain structure and function. In [78], these permutation patterns at individual ROIs when comparing controls to eMCI, MCI, and MCI converters, revealed changes that follow a neuroanatomical trajectory consistent with the AD continuum. Subsequently, graph-based permutation patterns were extended to the continuos case by incorporating signal amplitude into pattern calculation [79] and explored in the same VSTMBT-fMRI and DTI dataset as in this thesis and in [78]. The application of the continuous method resulted in additional ROIs being identified in each stage of MCI and was consistent with the AD trajectory mentioned previously. In sum, this thesis contributes to a growing body of evidence which suggests that the VSTMBT is a cognitive biomarker of AD, and that nQ-based network measures may be sensitive to a key turning point of the disease where MCI converts to AD.

The reorganizational effects of AD on functional and structural brain connectivity has lead to AD being named a disconnection syndrome [147]. Prior research in network neuroscience had established that modularity is particularly sensitive to the stages of AD as opposed to other network measures of brain organization [20]. However, this understanding in the modular disruption of brain networks due to AD had been limited to a global level. This thesis provides, to our knowledge, the first quantification of modularity for individual nodes (ROIs) in single and multiplex networks, nQ, and how this measure varies, *collapsibility*. This presents a significant step in understanding the modular changes in AD given that these effects were observed in VSTMBT-fMRI, DTI, VSTMBT-EEG, and that observations from VSTMBT-fMRI could be used to improve models of simulated disease progression. This makes a case for nQ-based measures in the understanding and analysis of brain networks in early-AD and in identifying the transition phase of MCI to AD conversion.

In this thesis, we introduce novel models and network measures based off of single-layer and multiplex modularity. We used the commonly used Louvain and generalized Louvain methods for modularity maximization as detailed in Section 3.2.7. This thesis chose modularity-based measures given their wide-spread use, and that research supports changes in modularity as a marker of AD [20]. However, it was previously noted that while this method is computationally

fast, that the variability that occurs due to the randomized seeding of initial communities requires multiple iterations to achieve stability [136, 137], leading to increasingly higher computational demands as the number of edges and layers in the network increase. That is, for the iterated version of the general Louvain method that we used (iterated_genlouvain in [130]) the computational demands are $O(m \cdot L \cdot I \cdot K)$, where m is the number of edges on one layer (L), I is the number of iterations until convergence in the iterated_genlouvain method (typically only a few in our research), and K is the number of iterations of the iterated_genlouvain (10-100 in this thesis). This makes the nQ-based measures introduced in this thesis, when used in conjunction with Louvain-based modularity maximization, linear in relation to the number of total edges (m in single-layer networks and $m \times L$ in multiplex networks). While this did not pose a significant problem in this thesis, care should be used in the application of the network-measures and models introduced in this thesis in order to balance computational time and stability.

Modularity is widely used in literature beyond network neuroscience. For instance, in understanding the modular structure in networks of protein-protein interaction, ecosystems, biological systems, disease spread, and power grids [204, 205, 206]. The novel network measures introduced in this thesis can be generally applied to any network-based analysis exploring modular organization. This has been supported in Chapters 3 and 4, where results of nQ's use in neuroimaging data, other publicly available datasets, and in surrogate networks reflect the novel behaviour of nQ in comparison to other common measures of node influence. This represents a significant advancement in the modelling of network modularity for use across a multitude of domains.

In sum, this thesis centres around the development of novel granular measures of community structure and their use in understanding subtle changes in community structure in brain networks. Chapters 3 and 4 showed not only the validity of these measures in comparison to other single and multiplex measures of node influence, but consistent changes in both temporal and frequency-based multiplex brain networks in the stages of MCI across multiple neuroimaging modalities (task-fMRI, DTI, and task-EEG). Furthermore, both task-fMRI and task-EEG data results showed distinct and expected differences between binding and shape tasks where we observed close to no significant changes for shape across both modalities. It should be noted that for the analyses of fMRI, DTI, and EEG, that close to all ROI results in nQ and collapsibility were unique. While the detected ROIs were largely consistent with known regional changes in MCI and AD, and some part of similar sub-network dysfunction (i.e., the Thalamus in the VSTMBT-EEG data linking to the general limbic dysfunction observed in the VSTMBT-fMRI data), there was a lack of overlap. This could be explained by a number of factors. First, modality-specific differences between structural (DTI) and functional (fMRI and EEG) brain networks is expected. While there is some correlation between functional and structural connectivity [266], the modular organization of these networks can be substantially

different and was observed in our exploration of fMRI-DTI multiplex networks of healthy subjects in Section 3.3.2. Second, while the fMRI and EEG networks in Chapters 3 and 4 explored functional connectivity of the same task, they were constructed with different atlases (Desikan and AAL respectively), used two separate types of connectivity (correlation-based for fMRI and phase-based for EEG) and modelled as two different types of multiplex network (temporal and frequency-based, respectively). Furthermore, no statistically significant changes were observed in MCI for the VSTMBT-fMRI networks while changes were observed in MCI for the VSTMBT-EEG networks, where we did not have data of what subjects were MCI converters and MCI subjects were more heterogenous. In addition, spatial patterns between functional connectivity in EEG and fMRI can differ substantially and can be explained by differences in functional connectivity measures (i.e., correlation vs. phase) [267]. The combination of the above factors makes comparison between the results of Chapter 4 with Chapters 3 and 5 difficult.

Chapter 5 connects to Chapters 3 and 4 by introducing novel attack models that extend to task-fMRI and simulate these granular changes in early-AD. The results reflected this where nQ changes in Chapter 3 in occipital and frontal lobes were used to construct targeted attack models in Chapter 5 which outperformed the benchmarks.

6.2 Limitations and Future Work

This section describes the limitations and future work that connect across multiple Chapters of the thesis. Limitations and future work related to the individual chapters can be found in Chapters 3, 4, and 5.

In this thesis, we maximized modularity by choosing the highest output from multiple iterations. However, it should be noted that this does not take into account the potential for multiple high modularity partitions of the network [136], which could lead to interpretation issues in our real-world examples in AD. We expect this effect to be small given that we found modularity to be tightly distributed in our real-world datasets, which were modelled in relatively small networks, and thus the number of degenerate solutions to maximized modularity should remain small. Future research should attempt to address these degeneracies (particularly for very large networks where this effect is more extreme), such as by comparing the partitions from many high-modularity solutions [268] or other methods of consensus clustering [182]. In addition, future work may consider how nQ behaves when calculated from group assignments that are not derived from modularity maximization. nQ may be able to be used in conjunction with community detection algorithms that bring improvements in group segregation or computational efficiency, expanding nQ's utility to general community detection domains by providing an improved measure of node influence.

In addition, this thesis explores functional connectivity networks of VSTMBT-fMRI data in Chapters 3 and 5. These networks had limited functional dynamics given that the stages of the task (encoding, maintenance, and probe) are fast (2-8s) while fMRI acquisition time had a TR of 2s. This meant that the encoding phase had to be combined with the maintenance phase of the task to ensure that there was enough data to compute correlation-based functional connectivity. While Section 3.2.5 describes the measures taken to maximise the available data for task-based dynamics between encoding, maintenance, and probe, it should be noted that the encmaint networks do not reflect encoding and maintenance on their own and is thus limited in their interpretation. However, it should be noted that results in the encmaint networks produced consistent results across Chapters 3 and 5 along with two separate, co-authored, publications using the same data [78, 79] where there were expected differences between shape and binding tasks, along with ROIs consistent with known changes in MCI. While the number of subjects in this study was small, and the temporal dynamics of fMRI limited the resolution and interpretability of the encmaint networks, consistent results suggest that these networks are reflecting granular changes in the VSTMBT due to early-AD.

In this thesis, nQ was introduced for unsigned networks. While negative edge weights do have biological significance [15], the interpretation of modules constructed from negative and positive weights is not well understood. We worried that per-subject differences in the proportion of negative and positive edge weights would heavily influence nQ in the VSTMBT-fMRI data in Chapters 3 and 5 and so we considered negative weights as equal to positive weights for modularity maximization. It is of note that this was not relevant to Chapter 4, and to the DTI data in Chapters 3, given that the networks constructed from these were unsigned by nature. While nQ was only introduced for unsigned networks in this thesis, the general Louvain method has been described for both signed and directed networks where extension to nQ can follow similar methodology as described in Section 3.2.6. As such, future work should consider the extension of nQ to signed and directed networks for the associated applications.

An additional consideration is the exploration of temporal multiplex networks in Chapter 3. The general Louvain method used in this thesis is invariant to the inversion of the layers of the network ($G_{[0,T]} = G_{[T,0]}$). While the methods used in this thesis are consistent with other temporal explorations of multiplex networks that explore modularity [17], it should be noted that this feature of the general Louvain method is not a desirable quality for temporal network analysis given the asymmetric properties of time [216]. Some methods of combining nQ with other methods of community detection may be an avenue for future work, though community detection in temporal graphs remains an open question [216].

In Chapters 3, 4, and 5, we presented granular, network-based, models of the VSTMBT in fMRI and EEG with nQ-based methods. While these methods were explored in some non-VSTMBT real-world and surrogate data, nQ-based methods have yet to be proven outside this paradigm. Given that nQ is a mathematical extension of modularity, future work should

apply these methods to resting state neuroimaging data and in other domains where modular structure is present. Additionally, the results of this thesis present a compelling case for the use of nQ-based methods for the analysis of early-AD. More work is needed to test these methods in larger cohorts, determine whether MCI converters are also characterized in EEG, and in exploring granular changes of modular structure in the later stages of AD.

6.3 Conclusion

This thesis contributes novel methods in network neuroscience for the exploration of brain networks in early-AD. First, it improves the utility of modularity, heavily studied in network neuroscience and other domains, by extending the measure to individual nodes (nQ) for improved granular analysis of networks. This measure was explored in early-AD for which a hallmark of the disease is abnormal functional and structural connectivity in VSTMBT-fMRI, DTI, and VSTMBT-EEG data. Importantly, nQ-based measures characterized a key turning point of AD (MCI converters), agreed with known differences in binding and shape tasks, aided in the simulation of VSTMBT-fMRI, and showed promise in categorizing MCI in VSTMBT-EEG. The prevalence of AD continues to rise and inter-subject variability makes detection challenging. Current diagnostic methods for AD are often invasive and costly, increasing the need for cheap and widely available methods like EEG. In the future, local health clinics could combine EEG with the VSTMBT and network methods such as nQ for early screening. With advances in AD sub-typing and simulation models of brain-network progression, targeting specific brain sub-networks may help address subject variability and pinpoint their position along the disease continuum. This thesis contributes towards early-AD detection by demonstrating the feasibility of several novel granular methods and models in brain networks, though further research is needed before clinical application is possible.

Appendix A

Chapter 3 Supplemental Material

A.1 Code and data availability

Code to calculate nQ is publicly available at `https://github.com/AvalonC-C/Nodal_Modularity`. The NKI-Rockland dataset is publicly available with access, study information and pre-processing details given in [269]. Additionally, Zachary's Karate Club can be accessed at `http://konect.cc/networks/ucidata-zachary/`. Regrettably, data access to our VSTMBT-fMRI cohort (further information here [48]) requires clinical research access approval from NHS Lothian and cannot be shared with any 3rd party as per their confidentiality and disclosure of information policy. However, note that access to some of the contents of the secondary data (current results) may be available on individual request from Javier Escudero ( ) or Mario A. Parra ( ), and that clinical research access to raw data can be applied for through the NHS Lothian Health Board.

A.2 fMRI windowing.

During fMRI scanning, stimuli onset does not always line up perfectly with volume acquisition (i.e., a stimuli could be shown at 1.5s while the volume was acquired from 0-2s). We account for this by approximately aligning our encmaint and probe windows to stimuli onset and optimize to capture peak HRF. First, we compare onset of stimulus timings with the following trial and shift our window forward or backward a volume to minimize the offset of trial start and volume acquisition time. This resulted in an offset for our task phase window in the range $[-1.47\text{s}, 0.24\text{s}]$. We then shift forward our window by one volume (2s), resulting in an offset of $[0.53\text{s}, 2.24\text{s}]$. The reason to shift forward is to better capture the signal peak of the HRF. To illustrate this shift's interaction with the HRF, consider the 4s probe phase while accounting for the 2s shift to increase the separation between the two phases. This results in our images corresponding with the signal dynamics of the task from stimuli onset up until a point in the range $[6.53\text{s}, 8.24\text{s}]$. This ensures that the signal peak information occurring at 5s is captured. It is important to note that there are a very small number of samples that do not perfectly

capture the HRF peak. This occurs when the maintenance phase is 2s and the alignment of the task phase window is towards the lower bound of our offset in the range $t = [4.53\text{s}, 6.24\text{s}]$. Given that the number of cases where our window does not fully capture the HRF peak is very small, and that the offset is only 0.47s, we maintained these samples, acknowledging that in a small number of cases the analysed sample does not fall exactly on the peak of the HRF. This would very slightly reduce our ability to find differences due to stimuli in the encmaint phase of the task but we expect this effect to be minor.

A.3 Variable maintenance phase of the VSTMBT.

The maintenance phase, where subjects must remember the presented shapes or coloured shapes, is displayed for a variable time as discussed in Fig 3.1. This is part of the fMRI design optimization aimed at decoupling the BOLD signal from encoding and maintenance for analyses such as statistical parametric mapping (not explored in this study). In this study, we do not expect the variable maintenance window to appreciably influence the comparison of nodal modularity in healthy and diseased brain networks due to the following. First, each subject's encmaint brain network is constructed from the correlations between repetitions of combined instances of the encoding and maintenance phase preserving temporal variability between brain ROIs. Second, all subjects in the study had an equal number of trials of each maintenance phase length presented at random within the scanning session. This ensures that the total time of all maintenance phases for each subject is equal.

A.4 Description of publicly available datasets.

Zachary's Karate Club is a commonly used dataset for exploring community structure in networks [270, 14]. It is a social network modelling the split in a karate club with one leader leaving and forming their own club and taking half of the members with them. In this case, the network's nodes are people and the edges between them denote friendship. Zachary's Karate Club, though simple, features a clearly defined modular structure that aids in the interpretation of graph metrics. Data was accessed (16/02/2024) and downloaded from `http://konect.cc/networks/ucidata-zachary/`.

The NKI-Rockland cohort is a publicly available dataset containing 196 subjects across lifetime (114 male; age range: 4-89 y.o.) [271] of pre-processed rs-fMRI and DTI data. These were generated at 3T with the following: an acquisition time of 10:55, TR $= 2500$ms, TE $=$ 30ms, voxel size $= 3\text{mm}^3$, and on 38 slices. DTI had an acquisition time of 13:32, TR $=$ 10000ms, TE $= 91$ms, voxel size $= 2$mm, and on 58 slices. Each of the connectomes were parcellated into 188 regions of interest using the Craddock atlas. From these, the network

edge weights were computed using Pearson correlation and were normalized by the maximum edge weight to the range [0,1]. In the case of DTI, edge weight was determined by the number of fibers that intersected at least one voxel in both the source and target region of interest (ROI) and normalized with the same method as with the fMRI networks. For further information, pre-processing, and availability see [269] (accessed on 30/08/2021).

Using the provided rs-fMRI and DTI matrices above, we process each subject's data by taking the absolute values of the fMRI connectivity networks and threshold them. Edges with the lowest edge weight were removed until the fMRI network's density matched that of the the subject's corresponding DTI network. Matching densities in this way helps to minimize some modality specific weighting of modularity within a multiplex setting, as fMRI networks are inherently much denser than DTI networks. However, as will be seen in the results, the two modalities retain very different topologies as expected even after matching for density.

A.5 FDR plots.

This figure visualizes the Benjamini-Hochberg FDR correction for each of our comparisons. Plots of observed p-values (p_k) by rank (k) show the ranked p-values in our ROI comparisons of a) fMRI multiplex control vs. MCI converters, b) DTI control vs. MCI, c) DTI control vs. MCI converters, and d) DTI eMCI vs. MCI. FDR controlled p-values are all p_i from $i = 1...k$, where $p_k \leq \frac{\alpha k}{m}$, and α is our chosen threshold. Plots of FDR adjusted p-values are also given to more easily visualize those that pass FDR correction (those that fall under the dashed line at $\alpha = 0.2$). Note that the strength of FDR correction is influenced by the number of p-values and so the multiplex results are more strongly controlled.

a)

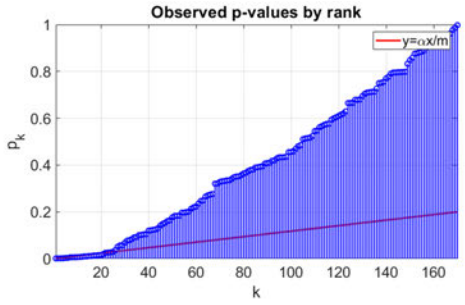
Observed p-values by rank
y=αx/m
p_k
k

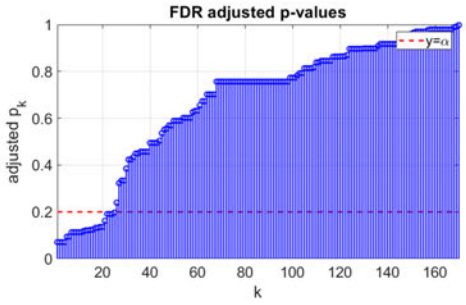
FDR adjusted p-values
y=α
adjusted p_k
k

b)

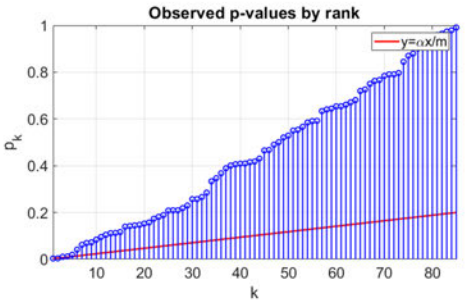
Observed p-values by rank
y=αx/m
p_k
k

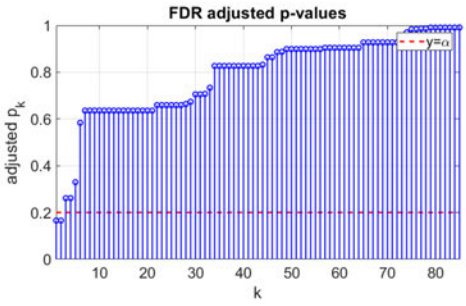
FDR adjusted p-values
y=α
adjusted p_k
k

c)

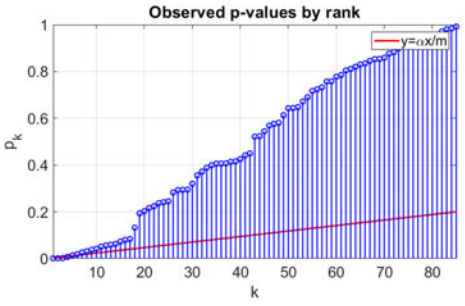
Observed p-values by rank
y=αx/m
p_k
k

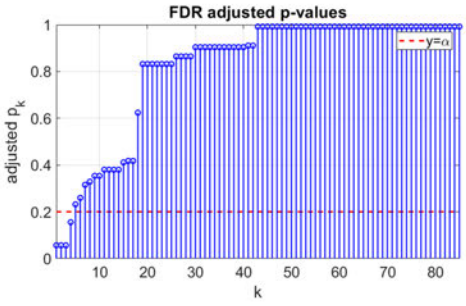
FDR adjusted p-values
y=α
adjusted p_k
k

d)

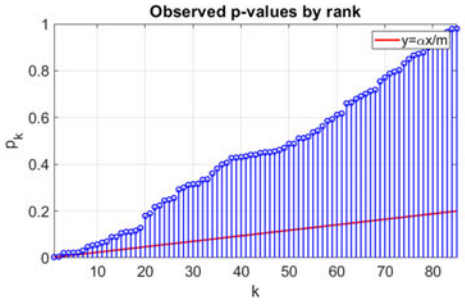
Observed p-values by rank
y=αx/m
p_k
k

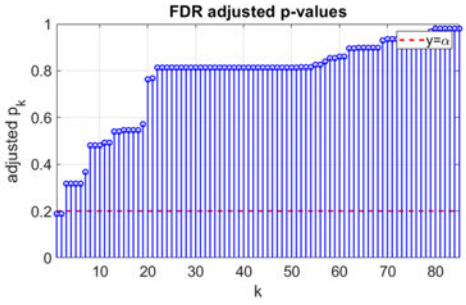
FDR adjusted p-values
y=α
adjusted p_k
k

A.6 Single-layer vs. multiplex results for the binding task.

This table displays the ROIs which pass the thresholds of $p \leq 0.05$ in the comparison of control vs. MCI converters and where p-values are controlled by FDR at $\alpha = 0.2$. These ROIs reside in either the encmaint (EM) or probe (P) single-layers or modeled together as a multiplex network (results given seperately in the left and right sides of the table respectively). Standard p-value (p) and effect size is displayed following permutation test and the area under the curve (AUC) of the Receiver Operating Characteristic (ROC). Multiplex construction yields a higher number of ROIs which pass the statistical thresholds (25 vs. 20), with lower p-values and higher effect sizes and ROC AUC among most ROIs. Additionally, note that FDR is applied to each layer separately in the single-layer case (85 ROIs each). Consequently, and since FDR is more strict for a higher number of comparisons, the multiplex model displays higher statistical power in determining regional changes in nQ between controls and MCI converters.

Single-layer				**Multiplex**			
ROIs	**p**	**effect size**	**ROC AUC**	**ROIs**	**p**	**effect size**	**ROC AUC**
EM R-caudalanteriorcingulate	0.003	2.067	0.938	EM R-caudalanteriorcingulate	0.002	2.362	0.938
EM R-fusiform	0.006	1.973	0.917	EM L-caudalanteriorcingulate	0.006	1.924	0.875
EM L-lingual	0.008	1.812	0.875	EM L-lingual	0.007	1.883	0.896
EM L-caudalanteriorcingulate	0.009	1.672	0.833	EM R-lingual	0.010	1.774	0.896
EM L-cuneus	0.010	1.608	0.875	EM L-middletemporal	0.008	1.708	0.896
EM R-lingual	0.019	1.537	0.833	EM L-pericalcarine	0.012	1.659	0.854
EM L-pericalcarine	0.024	1.478	0.771	EM R-parsopercularis	0.007	1.634	0.813
EM L-middletemporal	0.021	1.467	0.875	EM R-lateralorbitofrontal	0.006	1.624	0.875
EM R-lateralorbitofrontal	0.020	1.431	0.854	EM L-parsorbitalis	0.010	1.614	0.875
EM L-fusiform	0.026	1.379	0.813	EM L-cuneus	0.014	1.556	0.896
EM L-lateralorbitofrontal	0.025	1.129	0.771	EM L-parsopercularis	0.016	1.483	0.833
P R-caudalanteriorcingulate	0.001	2.191	0.979	EM L-fusiform	0.020	1.453	0.792
P R-lateralorbitofrontal	0.005	1.902	0.917	EM R-fusiform	0.029	1.394	0.813
P L-bankssts	0.003	1.876	0.938	EM L-lateralorbitofrontal	0.026	1.149	0.792
P L-fusiform	0.006	1.778	0.896	P R-caudalanteriorcingulate	0.001	2.363	0.979
P L-caudalanteriorcingulate	0.005	1.769	0.938	P L-caudalanteriorcingulate	0.003	2.039	0.917
P L-pericalcarine	0.009	1.763	0.854	P L-bankssts	0.001	1.722	0.958
P L-medialorbitofrontal	0.014	1.619	0.896	P L-lateralorbitofrontal	0.003	1.702	0.917
P L-parsorbitalis	0.008	1.447	0.917	P R-lateralorbitofrontal	0.006	1.663	0.896
P L-lateralorbitofrontal	0.018	1.413	0.875	P L-parsorbitalis	0.002	1.64	0.938
				P L-pericalcarine	0.012	1.626	0.833
				P R-lingual	0.015	1.531	0.854
				P L-fusiform	0.014	1.453	0.854
				P L-medialorbitofrontal	0.026	1.444	0.813
				P R-bankssts	0.027	1.382	0.833
				P L-lingual	0.037	1.29	0.854

A.7 Selected ROC plots.

Here we visualize a selection of the top performing ROC curves in distinguishing controls from MCI converters for ROIs in the fMRI multiplex binding networks. These plots represent sensitivity (true positive rate) against 1-specificity (false positive rate), where the area under the curve is a measure of the classifier's performance in separating the two groups. a) ROC curve for controls vs. MCI converters for the right caudal anterior cingulate in the probe layer of the network ($AUC = 0.979$). b) Left Bankssts in the probe layer ($AUC = 0.958$). c) Right caudal anterior cingulate in the encmaint layer ($AUC = 0.938$). d) Left pars orbitalis ($AUC = 0.938$). For a list of all statistically significant results in the fMRI multiplex binding networks see Table 3.2.

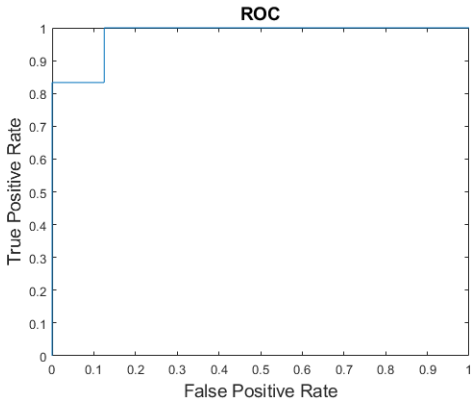

(a)

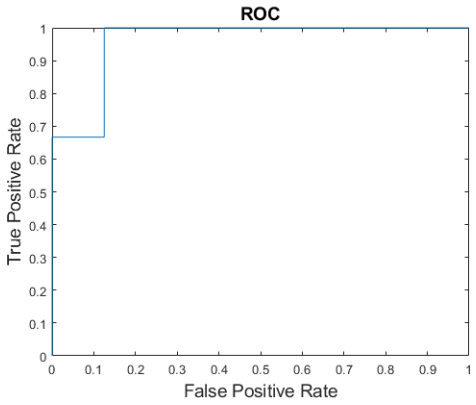

(b)

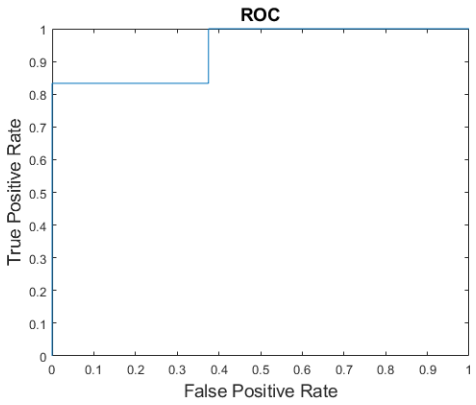

(c)

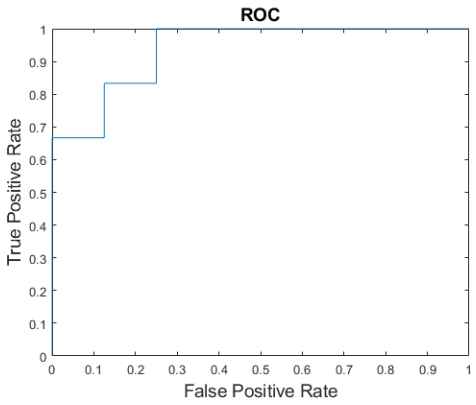

(d)

A.8 Changes in nQ in DTI for early MCI vs. MCI and MCI vs. MCI converters.

This table displays the ROIs which passed $p \leq 0.05$ and FDR controlled at $\alpha = 0.2$. L and R indicate the left or right hemispheres of the brain respectively. Standard p-value and effect size is displayed following permutation test and the area under the curve (AUC) of the Receiver Operating Characteristic (ROC).

Comparisons	ROIs	p	effect size	ROC AUC
early MCI vs. MCI	R-postcentral	0.003	1.850	0.929
	R-precentral	0.004	1.729	0.900
MCI vs. MCI converters				

A.9 Neurospsychological tests.

Here we show the neuropsychological profile of MCI patients, early MCI patients and healthy controls entering the study. ANOVA revealed that patients with MCI performed poorer than healthy controls on ACE [272], MMSE [272], HVLT-DELAY and TOT [273], FAS [274], DIGIT SYMBOL [275], REY-IMMEDIATE and DELAY [276], GNT [277], CLOCK [272], FCSRT-IFR and ITR [278], and TOPF [279]. More specifically, significant differences emerged from comparisons between MCI patients and healthy controls, and MCI patients versus early MCI patients overall. HVLT was carried out poorly from both MCI and early MCI patients compared to the control group, whereas Rey figure delayed copy was significantly underperformed by MCI patients only.

Although the conversion to AD in some patients has been ascertained once the collection of neuropsychological data was done, and MCI converters have not been taken into account here, we can conclude that these results are in line with clinical diagnosis and reflect the progression of the disease through the spectrum.

	MCI (N = 16)	**early MCI** (N = 7)	**Healthy Controls** (N = 8)	**ANOVA**
	M Mdn SD (range)	**M Mdn SD** (range)	**M Mdn SD** (range)	**E(2,28)** (p-value)
ACE	77.81 80 11.2 (53-97)	93.42 94 3.4 (90-98)	96.62 96.5 2.72 (91-100)	**16.49 (<0.001)**
MMSE	25.06 25.5 3.56 (17-30)	29.14 29 0.9 (28-30)	29.5 30 0.92 (28-30)	**9.83 (<0.001)**
TMT-A	71.31 55 66.77 (30-317)	40.85 41 10.76 (26-55)	39.37 40.5 7.23 (29-50)	1.55 (0.22)
TMT-B	200 160.5 147.21 (56-585)	132.26 131 40.46 (85-191)	100 91.5 39.97 (50-171)	2.42 (0.1)
HVLT-REC	9.68 10 2.21 (4-12)	10 10 1.63 (7-12)	11.25 12 1.16 (9-12)	1.87 (0.17)
HVLT-DELAY	2.62 0.5 3.44 (0-10)	4.85 7 3.23 (0-8)	8.87 8.5 2.41 (5-12)	**10.36 (<0.001)**
HVLT-TOT	14.56 14.5 6.13 (4-29)	17.28 17 3.9 (10-22)	23 23 4.37 (16-29)	**6.37 (0.004)**
FAS	32.62 31.5 16.19 (9-65)	51.57 52 8.1 (41-60)	49.12 50 11.4 (31-69)	**6.49 (0.005)**
ANIMAL FLUENCY	6.68 5.5 5.08 (1-12)	6.71 6 3.09 (3-13)	9.12 6.5 7.64 (6-28)	0.57 (0.56)
DIGIT SYMBOL	36.18 34.5 13.92 (10-60)	56.85 57 7.05 (48-66)	55 53 16.57 (35-85)	**8.21 (0.002)**
DIGIT SPAN	5.06 5 0.99 (3-7)	5.57 6 0.78 (4-6)	5.75 6 1.03 (4-7)	1.57 (0.22)
REY-COPY	32.71 34 3.02 (24-36)	31.42 34 7.43 (15-36)	33.62 34 3.62 (25-36)	0.45 (.64)
REY-IMMEDIATE	12.25 11.75 8.06 (0-23)	21.5 23 7.65 (6-30.5)	24.37 26.25 8.33 (13-34)	**7.19 (0.003)**
REY-DELAY	12.06 14.25 9.13 (0-24)	19.64 20.5 7.49 (5-30.5)	21.56 19.5 8.45 (10-34)	**(3.93) (0.003)**
GNT	18.06 19 4.78 (7-25)	23.57 24 4.19 (17-28)	24.62 26 3.7 (18-29)	**7.44 (0.003)**
CLOCK	4.25 4 0.77 (3-5)	4.71 5 0.48 (4-5)	5 5 0 (5-5)	**4.36 (0.02)**
FCSRT-IFR	12.18 9.5 10.29 (0-33)	25 24 5.65 (17-36)	26.37 26.5 6.54 (15-35)	**9.6 (0.001)**
FCSRT-ICR	13.06 14.5 3.66 (3-16)	15.28 16 1.89 (11-16)	15.87 16 0.35 (15-16)	3.2 (0.056)
FCSRT-ITR	32.93 38.5 15.78 (3-48)	45.85 48 4.41 (36-48)	47.5 48 1.06 (45-48)	**5.37 (0.01)**
TOPF	53.18 56.5 14.5 (27-70)	65.57 70 8.16 (48-70)	65.37 68 5.65 (55-70)	**4.32 (0.02)**
GDS	2 1 2.78 (0-10)	1.42 1 1.51 (0-4)	2.21 1 2.53 (0-6)	0.17 (0.84)

Note: Significant ($p < 0.05$) tests highlighted in bold.

N = Number of subjects; M = Mean; Mdn = Median; SD = Standard deviation.

ACE = Addenbrooke's Cognitive Examination; MMSE = Mini Mental State Examination; TMT = Trail Making Test (Version A and B) [280]; HVLT = Hopkins Verbal Learning Test-Revised (Recognition, Delayed Recall, Total Recall); REY = Rey-Osterrieth Complex Figure Test (Copy, Immediate Reproduction, Delayed Reproduction); GNT = Graded Naming Test; FCSRT = Free and Cued Selective Reminding Test (IFR = Immediate Free Recall; ICR = Immediate Cued Recall; ITR = Immediate Total Recall); TOPF = Test of Premorbid Functioning; GDS = Geriatric Depression Scale [281].

Appendix B

Chapter 4 Supplemental Material

B.1 FDR plots.

Here we show the Benjamini-Hochberg FDR correction for the control vs. MCI comparisons made in Chapter 4. Plots of observed p-values (p_k) by rank (k) show the ranked p-values in our ROI comparisons of a) nQ in multiplex frequency networks of control vs. MCI for the probe phase of the binding task, b) node flexibility in the probe phase of binding, c) node flexibility in the probe phase of the shape task, d) collapsibility in encoding binding, and e) collapsibility in the probe phase of binding. FDR controlled p-values are all p_i from $i = 1...k$, where $p_k \leq \frac{\alpha k}{m}$, and α is our chosen threshold. Plots of FDR adjusted p-values are also given to more easily visualize those that pass FDR correction (those that fall under the dashed line at $\alpha = 0.2$). Furthermore, note that (a) visualizes nQ in the multiplex network of the four frequency bands and thus has 464 comparisons. On the other hand, figures b-e show 116 comparisons given that collapsibility and flexibility are aggregate measures over the four frequency bands.

a)

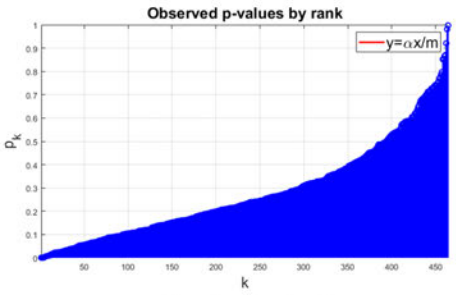
Observed p-values by rank
y=αx/m
p_k
k

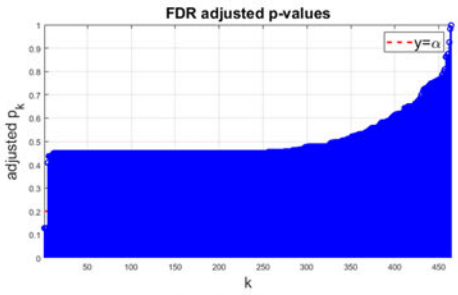
FDR adjusted p-values
y=α
adjusted p_k
k

b)

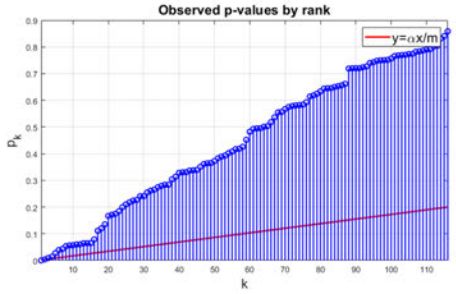
Observed p-values by rank
y=αx/m
p_k
k

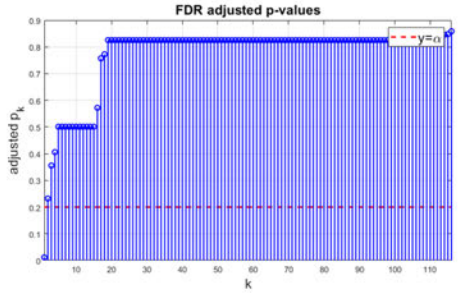
FDR adjusted p-values
y=α
adjusted p_k
k

c)

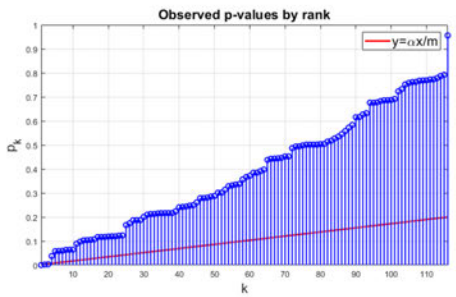
Observed p-values by rank
y=αx/m
p_k
k

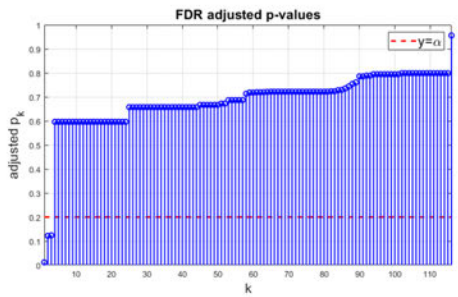
FDR adjusted p-values
y=α
adjusted p_k
k

d)

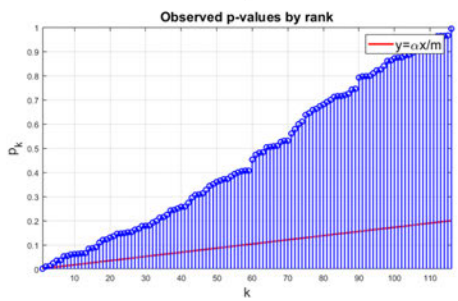
Observed p-values by rank
y=αx/m
p_k
k

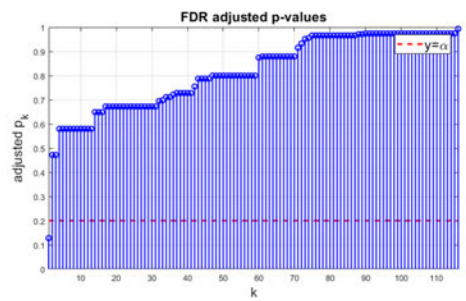
FDR adjusted p-values
y=α
adjusted p_k
k

e)

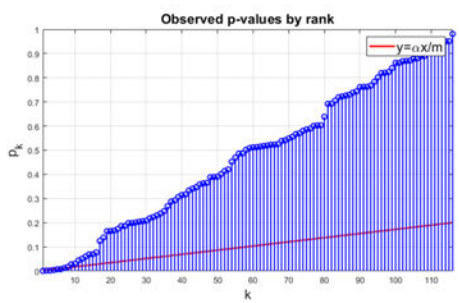
Observed p-values by rank
y=αx/m
p_k
k

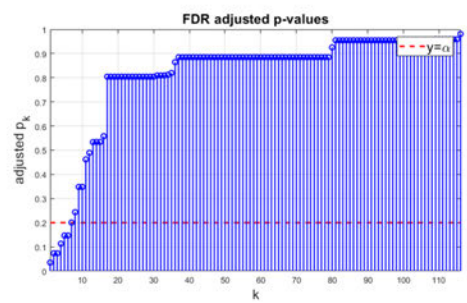
FDR adjusted p-values
y=α
adjusted p_k
k

Bibliography

[1] Frisoni GB, Hansson O, Nichols E, Garibotto V, Schindler SE, van der Flier WM, et al. New landscape of the diagnosis of Alzheimer's disease. The Lancet. 2025;406(10510):1389–1407. doi:10.1016/S0140-6736(25)01294-2.

[2] Scheltens P, De Strooper B, Kivipelto M, Holstege H, Chételat G, Teunissen CE, et al. Alzheimer's disease. The Lancet. 2021;397(10284):1577–1590. doi:10.1016/S0140-6736(20)32205-4.

[3] Kanasi E, Ayilavarapu S, Jones J. The aging population: demographics and the biology of aging. Periodontology 2000. 2016;72(1):13–18. doi:10.1111/PRD.12126.

[4] Sanford AM. Mild Cognitive Impairment. Clinics in geriatric medicine. 2017;33(3):325–337. doi:10.1016/J.CGER.2017.02.005.

[5] Gauthier S, Reisberg B, Zaudig M, Petersen RC, Ritchie K, Broich K, et al. Mild cognitive impairment. Lancet. 2006;367(9518):1262–1270. doi:10.1016/S0140-6736(06)68542-5.

[6] Zetterberg H, Bendlin BB. Biomarkers for Alzheimer's disease—preparing for a new era of disease-modifying therapies. Molecular Psychiatry. 2020;26(1):296–308. doi:10.1038/s41380-020-0721-9.

[7] Rossini PM, Di Iorio R, Vecchio F, Anfossi M, Babiloni C, Bozzali M, et al. Early diagnosis of Alzheimer's disease: the role of biomarkers including advanced EEG signal analysis. Report from the IFCN-sponsored panel of experts. Clinical Neurophysiology. 2020;131(6):1287–1310. doi:10.1016/j.clinph.2020.03.003.

[8] Mahaman YAR, Embaye KS, Huang F, Li L, Zhu F, Wang JZ, et al. Biomarkers used in Alzheimer's disease diagnosis, treatment, and prevention. Ageing Research Reviews. 2022;74:101544. doi:10.1016/J.ARR.2021.101544.

[9] Dubois B, Feldman HH, Jacova C, Cummings JL, DeKosky ST, Barberger-Gateau P, et al. Revising the definition of Alzheimer's disease: a new lexicon. The Lancet Neurology. 2010;9(11):1118–1127. doi:10.1016/S1474-4422(10)70223-4.

[10] Dubois B, Feldman HH, Jacova C, Hampel H, Molinuevo JL, Blennow K, et al. Advancing research diagnostic criteria for Alzheimer's disease: the IWG-2 criteria. The Lancet Neurology. 2014;13(6):614–629. doi:10.1016/S1474-4422(14)70090-0.

[11] Bullmore E, Sporns O. The economy of brain network organization. Nature Reviews Neuroscience. 2012;13(5):336–349. doi:10.1038/nrn3214.

[12] Liao X, Vasilakos AV, He Y. Small-world human brain networks: Perspectives and challenges. Neuroscience & Biobehavioral Reviews. 2017;77:286–300. doi:10.1016/J.NEUBIOREV.2017.03.018.

[13] Betzel RF, Bassett DS. Multi-scale brain networks. NeuroImage. 2017;160:73–83. doi:10.1016/j.neuroimage.2016.11.006.

[14] Girvan M, Newman MEJ. Community structure in social and biological networks. Proceedings of the National Academy of Sciences. 2002;99(12):7821–7826. doi:10.1073/PNAS.122653799.

[15] Sporns O, Betzel RF. Modular brain networks. Annual Review of Psychology. 2016;67:613–640. doi:10.1146/annurev-psych-122414-033634.

[16] Bassett DS, Sporns O. Network neuroscience. Nature Neuroscience. 2017;20(3):353–364. doi:10.1038/nn.4502.

[17] Bassett DS, Wymbs NF, Porter MA, Mucha PJ, Carlson JM, Grafton ST. Dynamic reconfiguration of human brain networks during learning. Proceedings of the National Academy of Sciences of the United States of America. 2011;108(18):7641–7646. doi:10.1073/pnas.1018985108.

[18] van den Heuvel MP, Hulshoff Pol HE. Exploring the brain network: A review on resting-state fMRI functional connectivity. European Neuropsychopharmacology. 2010;20(8):519–534. doi:10.1016/j.euroneuro.2010.03.008.

[19] Gamboa OL, Tagliazucchi E, Von Wegner F, Jurcoane A, Wahl M, Laufs H, et al. Working memory performance of early MS patients correlates inversely with modularity increases in resting state functional connectivity networks. NeuroImage. 2014;94:385–395. doi:10.1016/J.NEUROIMAGE.2013.12.008.

[20] Pereira JB, Mijalkov M, Kakaei E, Mecocci P, Vellas B, Tsolaki M, et al. Disrupted Network Topology in Patients with Stable and Progressive Mild Cognitive Impairment and Alzheimer's Disease. Cerebral Cortex. 2016;26(8):3476–3493. doi:10.1093/CERCOR/BHW128.

[21] Bullmore E, Sporns O. Complex brain networks: graph theoretical analysis of structural and functional systems. Nature Reviews Neuroscience. 2009;10(3):186–198. doi:10.1038/nrn2575.

[22] De Haan W, Van der Flier WM, Koene T, Smits LL, Scheltens P, Stam CJ. Disrupted modular brain dynamics reflect cognitive dysfunction in Alzheimer's disease. NeuroImage. 2012;59(4):3085–3093. doi:10.1016/J.NEUROIMAGE.2011.11.055.

[23] Sun Y, Yin Q, Fang R, Yan X, Wang Y, Bezerianos A, et al. Disrupted Functional Brain Connectivity and Its Association to Structural Connectivity in Amnestic Mild Cognitive Impairment and Alzheimer's Disease. PLOS ONE. 2014;9(5):e96505. doi:10.1371/JOURNAL.PONE.0096505.

[24] Jalili M. Graph theoretical analysis of Alzheimer's disease: Discrimination of AD patients from healthy subjects. Information Sciences. 2017;384:145–156. doi:10.1016/J.INS.2016.08.047.

[25] del Pozo SM, Laufs H, Bonhomme V, Laureys S, Balenzuela P, Tagliazucchi E. Unconsciousness reconfigures modular brain network dynamics. Chaos: An Interdisciplinary Journal of Nonlinear Science. 2021;31(9):093117. doi:10.1063/5.0046047.

[26] Chen X, Necus J, Peraza LR, Mehraram R, Wang Y, O'Brien JT, et al. The functional brain favours segregated modular connectivity at old age unless affected by neurodegeneration. Communications Biology 2021 4:1. 2021;4(1):1–16. doi:10.1038/s42003-021-02497-0.

[27] Contreras JA, Avena-Koenigsberger A, Risacher SL, West JD, Tallman E, McDonald BC, et al. Resting state network modularity along the prodromal late onset Alzheimer's disease continuum. NeuroImage: Clinical. 2019;22:101687. doi:10.1016/J.NICL.2019.101687.

[28] De Domenico M. Multilayer modeling and analysis of human brain networks. GigaScience. 2017;6(5):1–8. doi:10.1093/gigascience/gix004.

[29] Parra MA, Abrahams S, Logie RH, Méndez LG, Lopera F, Della Sala S. Visual short-term memory binding deficits in familial Alzheimer's disease. Brain. 2010;133(9):2702–2713. doi:10.1093/brain/awq148.

[30] Campbell-Cousins A, Guazzo F, Bastin ME, Parra MA, Escudero J. Multiplex nodal modularity: A novel network metric for the regional analysis of amnestic mild cognitive impairment during a working memory binding task. PLOS ONE. 2025;20(8):e0328736. doi:10.1371/JOURNAL.PONE.0328736.

[31] Wittenberg R, Knapp M, Hu B, Comas-Herrera A, King D, Rehill A, et al. The costs of dementia in England. Wiley Online Library. 2019;34(7):1095–1103. doi:10.1002/gps.5113.

[32] Dubois B, Hampel H, Feldman HH, Scheltens P, Aisen P, Andrieu S, et al. Preclinical Alzheimer's disease: Definition, natural history, and diagnostic criteria. Alzheimer's and Dementia. 2016;12(3):292–323. doi:10.1016/j.jalz.2016.02.002.

[33] Rostagno AA. Pathogenesis of Alzheimer's Disease. International Journal of Molecular Sciences 2023, Vol 24, Page 107. 2022;24(1):107. doi:10.3390/IJMS24010107.

[34] De Strooper B, Karran E. The Cellular Phase of Alzheimer's Disease. Cell. 2016;164(4):603–615. doi:10.1016/J.CELL.2015.12.056.

[35] Mueller SG, Weiner MW, Thal LJ, Petersen RC, Jack CR, Jagust W, et al. Ways toward an early diagnosis in Alzheimer's disease: The Alzheimer's Disease Neuroimaging Initiative (ADNI). Alzheimer's and Dementia. 2005;1(1):55–66. doi:10.1016/j.jalz.2005.06.003.

[36] Kivipelto M, Mangialasche F, Ngandu T. Lifestyle interventions to prevent cognitive impairment, dementia and Alzheimer disease. Nature Reviews Neurology 2018 14:11. 2018;14(11):653–666. doi:10.1038/s41582-018-0070-3.

[37] Veitch DP, Weiner MW, Aisen PS, Beckett LA, DeCarli C, Green RC, et al. Using the Alzheimer's Disease Neuroimaging Initiative to improve early detection, diagnosis, and treatment of Alzheimer's disease. Alzheimer's & Dementia. 2022;18(4):824–857. doi:10.1002/ALZ.12422.

[38] Venegas C, Kumar S, Franklin BS, Dierkes T, Brinkschulte R, Tejera D, et al. Microglia-derived ASC specks cross-seed amyloid-β in Alzheimer's disease. Nature 2017 552:7685. 2017;552(7685):355–361. doi:10.1038/nature25158.

[39] Sweeney MD, Sagare AP, Zlokovic BV. Blood-brain barrier breakdown in Alzheimer disease and other neurodegenerative disorders. Nature reviews Neurology. 2018;14(3):133–150. doi:10.1038/NRNEUROL.2017.188.

[40] Plog BA, Nedergaard M. The glymphatic system in CNS health and disease: past, present and future. Annual review of pathology. 2018;13:379. doi:10.1146/ANNUREV-PATHOL-051217-111018.

[41] Jack CR, Andrews JS, Beach TG, Buracchio T, Dunn B, Graf A, et al. Revised criteria for diagnosis and staging of Alzheimer's disease: Alzheimer's Association Workgroup. Alzheimer's & Dementia. 2024;20(8):5143–5169. doi:10.1002/ALZ.13859.

[42] Frisoni GB, Festari C, Massa F, Cotta Ramusino M, Orini S, Aarsland D, et al. European intersocietal recommendations for the biomarker-based diagnosis of neurocognitive disorders. The Lancet Neurology. 2024;23(3):302–312. doi:10.1016/S1474-4422(23)00447-7.

[43] Mankhong S, Kim S, Lee S, Kwak HB, Park DH, Joa KL, et al. Development of Alzheimer's Disease Biomarkers: From CSF- to Blood-Based Biomarkers. Biomedicines. 2022;10(4):850. doi:10.3390/BIOMEDICINES10040850.

[44] Grothe MJ, Teipel SJ. Spatial patterns of atrophy, hypometabolism, and amyloid deposition in Alzheimer's disease correspond to dissociable functional brain networks. Human Brain Mapping. 2016;37(1):35. doi:10.1002/HBM.23018.

[45] Berron D, van Westen D, Ossenkoppele R, Strandberg O, Hansson O. Medial temporal lobe connectivity and its associations with cognition in early Alzheimer's disease. Brain. 2020;143(3):1233–1248. doi:10.1093/BRAIN/AWAA068.

[46] Bastin C, Delhaye E. Targeting the function of the transentorhinal cortex to identify early cognitive markers of Alzheimer's disease. Cognitive, Affective, & Behavioral Neuroscience. 2023;23(4):986–996. doi:10.3758/S13415-023-01093-5.

[47] Didic M, Barbeau EJ, Felician O, Tramoni E, Guedj E, Poncet M, et al. Which memory system is impaired first in Alzheimer's disease? Journal of Alzheimer's disease : JAD. 2011;27(1):11–22. doi:10.3233/JAD-2011-110557.

[48] Parra MA, Calia C, Pattan V, Della Sala S. Memory markers in the continuum of the Alzheimer's clinical syndrome. Alzheimer's Research and Therapy. 2022;14(1):1–16. doi:10.1186/s13195-022-01082-9.

[49] Hernandez H, Baez S, Medel V, Moguilner S, Cuadros J, Santamaria-Garcia H, et al. Brain health in diverse settings: How age, demographics and cognition shape brain function. NeuroImage. 2024;295:120636. doi:10.1016/J.NEUROIMAGE.2024.120636.

[50] Sanei S. Adaptive Processing of Brain Signals. John Wiley & Sons, Ltd; 2013.

[51] Smith KM, Starr JM, Escudero J, Ibañez A, Parra MA. Abnormal Functional Hierarchies of EEG Networks in Familial and Sporadic Prodromal Alzheimer's Disease During Visual Short-Term Memory Binding. Frontiers in Neuroimaging. 2022;1:883968. doi:10.3389/FNIMG.2022.883968/BIBTEX.

[52] Hubert D Z, Mecklinger A, Lindenberger U. Levels of binding: types, mechanisms, and functions of binding in remembering. In: Handbook of Binding and Memory, Perspective from Cognitive Neuroscience. New York: Oxford University Press; 2006. p. 3–25. Available from: `https://pure.mpg.de/rest/items/item_2100788/component/file_2100787/content`.

[53] Colzato LS, Raffone A, Hommel B. What Do We Learn From Binding Features? Evidence for Multilevel Feature Integration. Journal of Experimental Psychology: Human Perception and Performance. 2006;32(3):705–716. doi:10.1037/0096-1523.32.3.705.

[54] Zimmer HD, Mecklinger A, Lindenberger U. Objects tokens, binding, and visual memory. In: Handbook of binding and memory, perspective from cognitive neuroscience. New York Oxford University Press; 2006. p. 315–338. Available from: `https://philpapers.org/rec/ZIMHOB`.

[55] Logie RH, Brockmole JR, Vandenbroucke ARE. Bound feature combinations in visual short-term memory are fragile but influence long-term learning. Visual Cognition. 2009;17(1-2):160–179. doi:10.1080/13506280802228411.

[56] Parra MA, Abrahams S, Fabi K, Logie R, Luzzi S, Sala SD. Short-term memory binding deficits in Alzheimer's disease. Brain. 2009;132(4):1057–1066. doi:10.1093/BRAIN/AWP036.

[57] Parra MA, Abrahams S, Logie RH, Sala SD. Age and binding within-dimension features in visual short-term memory. Neuroscience Letters. 2009;449(1):1–5. doi:10.1016/J.NEULET.2008.10.069.

[58] Parra MA, della Sala S, Logie RH, Abrahams S. Selective impairment in visual short-term memory binding. Cognitive Neuropsychology. 2009;26(7):583–605. doi:10.1080/02643290903523286.

[59] Chalfonte BL, Johnson MK. Feature memory and binding in young and older adults. Memory and Cognition. 1996;24(4):403–416. doi:10.3758/BF03200930/METRICS.

[60] Naveh-Benjamin M. Adult Age Differences in Memory Performance: Tests of an Associative Deficit Hypothesis. Journal of Experimental Psychology: Learning Memory and Cognition. 2000;26(5):1170–1187. doi:10.1037/0278-7393.26.5.1170.

[61] Chen T, Naveh-Benjamin M. Assessing the associative deficit of older adults in long-term and short-term/working memory. Psychology and Aging. 2012;27(3):666–682. doi:10.1037/A0026943.

[62] Baddeley A. Working memory. Current Biology. 2010;20(4):R136–R140. doi:10.1016/j.cub.2009.12.014.

[63] Parra MA, Fabi K, Luzzi S, Cubelli R, Hernandez Valdez M, Della Sala S. Relational and conjunctive binding functions dissociate in short-term memory. Neurocase. 2015;21(1):56–66. doi:10.1080/13554794.2013.860177.

[64] Geinisman Y, Detoledo-Morrell L, Morrell F, Heller RE. Hippocampal markers of age-related memory dysfunction: Behavioral, electrophysiological and morphological perspectives. Progress in Neurobiology. 1995;45(3):223–252. doi:10.1016/0301-0082(94)00047-L.

[65] Raz N. Aging of the brain and its impact on cognitive performance: Integration of structural and functional findings. In: The handbook of aging and cognition. 2nd ed. Lawrence Erlbaum Associates Publishers; 2000. p. 1–90. Available from: `https://psycnet.apa.org/record/2000-07017-001`.

[66] Della Sala S, Parra MA, Fabi K, Luzzi S, Abrahams S. Short-term memory binding is impaired in AD but not in non-AD dementias. Neuropsychologia. 2012;50(5):833–840. doi:10.1016/J.NEUROPSYCHOLOGIA.2012.01.018.

[67] Norton DJ, Parra MA, Sperling RA, Baena A, Guzman-Velez E, Jin DS, et al. Visual short-term memory relates to tau and amyloid burdens in preclinical autosomal dominant Alzheimer's disease. Alzheimer's Research and Therapy. 2020;12(1):1–11. doi:10.1186/S13195-020-00660-Z/FIGURES/3.

[68] Cecchini MA, Yassuda MS, Squarzoni P, Coutinho AM, de Paula Faria D, Duran FLdS, et al. Deficits in short-term memory binding are detectable in individuals with brain amyloid deposition in the absence of overt neurodegeneration in the Alzheimer's disease continuum. Brain and Cognition. 2021;152:105749. doi:10.1016/J.BANDC.2021.105749.

[69] Parra MA, Mikulan E, Trujillo N, Sala SD, Lopera F, Manes F, et al. Brain Information Sharing During Visual Short-Term Memory Binding Yields a Memory Biomarker for Familial Alzheimer's Disease. Current Alzheimer research. 2017;14(12). doi:10.2174/1567205014666170614163316.

[70] Gonzalez-Montealegre RA, González-Hernández A, Bonilla-Santos J, Cala-Martínez DY, Parra MA. Electrophysiological correlates of visual short-term memory binding deficits in community-dwelling seniors at risk of dementia. Clinical Neurophysiology. 2025;171:227–239. doi:10.1016/J.CLINPH.2025.01.009.

[71] Parra MA, Gazes Y, Habeck C, Stern Y. Exploring the Association between Amyloid-β and Memory Markers for Alzheimer's Disease in Cognitively Unimpaired Older Adults. Journal of Prevention of Alzheimer's Disease. 2024;11(2):339–347. doi:10.14283/jpad.2024.11.

[72] Valdés Hernández MC, Clark R, Wang SH, Guazzo F, Calia C, Pattan V, et al. The striatum, the hippocampus, and short-term memory binding: Volumetric analysis of the subcortical grey matter's role in mild cognitive impairment. NeuroImage: Clinical. 2020;25:102158. doi:10.1016/J.NICL.2019.102158.

[73] Baillet S. Magnetoencephalography for brain electrophysiology and imaging. Nature Neuroscience. 2017;20(3):327–339. doi:10.1038/NN.4504;TECHMETA.

[74] Pan R, Yang C, Li Z, Ren J, Duan Y. Magnetoencephalography-based approaches to epilepsy classification. Frontiers in Neuroscience. 2023;17:1183391. doi:10.3389/FNINS.2023.1183391/EPUB.

[75] Logothetis NK. What we can do and what we cannot do with fMRI. Nature. 2008;453(7197):869–878. doi:10.1038/nature06976.

[76] Peters F, Collette F, Degueldre C, Sterpenich V, Majerus S, Salmon E. The neural correlates of verbal short-term memory in Alzheimer's disease: an fMRI study. Brain. 2009;132(7):1833–1846. doi:10.1093/BRAIN/AWP075.

[77] Parra MA, Della Sala S, Logie RH, Morcom AM. Neural correlates of shape-color binding in visual working memory. Neuropsychologia. 2014;52(1):27–36. doi:10.1016/J.NEUROPSYCHOLOGIA.2013.09.036.

[78] Fabila-Carrasco JS, Campbell-Cousins A, Parra-Rodriguez MA, Escudero J. Graph-Based Permutation Patterns for the Analysis of Task-Related FMRI Signals on DTI Networks in Mild Cognitive Impairment. ICASSP, IEEE International Conference on Acoustics, Speech and Signal Processing - Proceedings. 2024; p. 2076–2080. doi:10.1109/ICASSP48485.2024.10447332.

[79] Roy O, Campbell-Cousins A, Carrasco-Stewart J, Parra MA, Escudero J. Activated Permutation Entropy for Graph Signals. Research Square (preprint). 2025;doi:10.21203/RS.3.RS-7220016/V1.

[80] Assaf Y, Pasternak O. Diffusion tensor imaging (DTI)-based white matter mapping in brain research: A review. Journal of Molecular Neuroscience. 2008;34(1):51–61. doi:10.1007/s12031-007-0029-0.

[81] Soares JM, Marques P, Alves V, Sousa N. A hitchhiker's guide to diffusion tensor imaging. Frontiers in Neuroscience. 2013;7(7 MAR):38546. doi:10.3389/FNINS.2013.00031/FULL.

[82] Lim KO, Helpern JA. Neuropsychiatric applications of DTI – a review. NMR in Biomedicine. 2002;15(7-8):587–593. doi:10.1002/NBM.789.

[83] Stebbins GT, Murphy CM. Diffusion Tensor Imaging in Alzheimer's Disease and Mild Cognitive Impairment. Behavioural Neurology. 2009;21(1-2):39–49. doi:10.3233/BEN-2009-0234.

[84] Naggara O, Oppenheim C, Rieu D, Raoux N, Rodrigo S, Dalla Barba G, et al. Diffusion tensor imaging in early Alzheimer's disease. Psychiatry Research: Neuroimaging. 2006;146(3):243–249. doi:10.1016/J.PSCYCHRESNS.2006.01.005.

[85] Oishi K, Mielke MM, Albert M, Lyketsos CG, Mori S. DTI analyses and clinical applications in Alzheimers Disease. Journal of Alzheimer's Disease. 2011;26(SUPPL. 3):287–296. doi:10.3233/JAD-2011-0007.

[86] Fellgiebel A, Wille P, Müller MJ, Winterer G, Scheurich A, Vucurevic G, et al. Ultrastructural hippocampal and white matter alterations in mild cognitive impairment: A diffusion tensor imaging study. Dementia and Geriatric Cognitive Disorders. 2004;18(1):101–108. doi:10.1159/000077817,.

[87] Kantarci K, Avula R, Senjem ML, Samikoglu AR, Zhang B, Weigand SD, et al. Dementia with Lewy bodies and Alzheimer disease: Neurodegenerative patterns characterized by DTI. Neurology. 2010;74(22):1814–1821. doi:10.1212/WNL.0B013E3181E0F7CF,.

[88] Rose SE, Janke AL, Chalk JB. Gray and white matter changes in Alzheimer's disease: A diffusion tensor imaging study. Journal of Magnetic Resonance Imaging. 2008;27(1):20–26. doi:10.1002/JMRI.21231,.

[89] Firbank MJ, Blamire AM, Teodorczuk A, Teper E, Mitra D, O'Brien JT. Diffusion tensor imaging in Alzheimer's disease and dementia with Lewy bodies. Psychiatry Research - Neuroimaging. 2011;194(2):176–183. doi:10.1016/j.pscychresns.2011.08.002.

[90] Brun A, Englund E. A white matter disorder in dementia of the Alzheimer type: A pathoanatomical study. Annals of Neurology. 1986;19(3):253–262. doi:10.1002/ANA.410190306,.

[91] Englund E, Brun A, Alling C. White matter changes in dementia of alzheimer's type: Biochemical and neuropathological correlates. Brain. 1988;111(6):1425–1439. doi:10.1093/BRAIN/111.6.1425,.

[92] Sjöbeck M, Haglund M, Englund E. Decreasing myelin density reflected increasing white matter pathology in azheimer's disease - A neuropathological study. International Journal of Geriatric Psychiatry. 2005;20(10):919–926. doi:10.1002/GPS.1384,.

[93] Jurcak V, Tsuzuki D, Dan I. 10/20, 10/10, and 10/5 systems revisited: Their validity as relative head-surface-based positioning systems. NeuroImage. 2007;34(4):1600–1611. doi:10.1016/J.NEUROIMAGE.2006.09.024.

[94] Michel CM, He B. EEG source localization. Handbook of Clinical Neurology. 2019;160:85–101. doi:10.1016/B978-0-444-64032-1.00006-0.

[95] Teplan M. Fundamentals of EEG Measurement. Measurement Science Review. 2002;2(2).

[96] Jeong J. EEG dynamics in patients with Alzheimer's disease. Clinical Neurophysiology. 2004;115(7):1490–1505. doi:10.1016/J.CLINPH.2004.01.001.

[97] Kowalski JW, Gawel M, Pfeffer A, Barcikowska M. The Diagnostic Value of EEG in Alzheimer Disease Correlation With the Severity of Mental Impairment. Journal of Clinical Neurophysiology. 2001;18(6):570–575. doi:10.1097/WNP.0000000000000301.

[98] Dauwels J, Vialatte F, Cichocki A. Diagnosis of Alzheimer's Disease from EEG Signals: Where Are We Standing? Current Alzheimer Research. 2010;7(6):487–505. doi:10.2174/156720510792231720.

[99] Babiloni C, Blinowska K, Bonanni L, Cichocki A, De Haan W, Del Percio C, et al. What electrophysiology tells us about Alzheimer's disease: a window into the synchronization and connectivity of brain neurons. Neurobiology of Aging. 2020;85:58–73. doi:10.1016/J.NEUROBIOLAGING.2019.09.008.

[100] Wen D, Zhou Y, Li X. A critical review: Coupling and synchronization analysis methods of EEG signal with mild cognitive impairment. Frontiers in Aging Neuroscience. 2015;7(APR):135928. doi:10.3389/FNAGI.2015.00054/BIBTEX.

[101] Babiloni C, Lizio R, Marzano N, Capotosto P, Soricelli A, Triggiani AI, et al. Brain neural synchronization and functional coupling in Alzheimer's disease as revealed by resting state EEG rhythms. International Journal of Psychophysiology. 2016;103:88–102. doi:10.1016/J.IJPSYCHO.2015.02.008.

[102] Boccaletti S, Bianconi G, Criado R, del Genio CI, Gómez-Gardeñes J, Romance M, et al. The structure and dynamics of multilayer networks. Physics Reports. 2014;544(1):1–122. doi:10.1016/j.physrep.2014.07.001.

[103] Rubinov M, Sporns O. Complex network measures of brain connectivity: Uses and interpretations. NeuroImage. 2010;52(3):1059–1069. doi:10.1016/J.NEUROIMAGE.2009.10.003.

[104] Bollobás B. Modern graph theory. Springer; 1998.

[105] van Diessen E, Numan T, van Dellen E, van der Kooi AW, Boersma M, Hofman D, et al. Opportunities and methodological challenges in EEG and MEG resting state functional brain network research. Clinical Neurophysiology. 2015;126(8):1468–1481. doi:10.1016/j.clinph.2014.11.018.

[106] Smith SM, Miller KL, Salimi-Khorshidi G, Webster M, Beckmann CF, Nichols TE, et al. Network modelling methods for FMRI. NeuroImage. 2011;54(2):875–891. doi:10.1016/J.NEUROIMAGE.2010.08.063.

[107] Vinck M, Oostenveld R, Van Wingerden M, Battaglia F, Pennartz CMA. An improved index of phase-synchronization for electrophysiological data in the presence of volume-conduction, noise and sample-size bias. NeuroImage. 2011;55(4):1548–1565. doi:10.1016/J.NEUROIMAGE.2011.01.055.

[108] Saramäki J, Kivelä M, Onnela JP, Kaski K, Kertész J. Generalizations of the clustering coefficient to weighted complex networks. Physical Review E - Statistical, Nonlinear, and Soft Matter Physics. 2007;75(2):027105. doi:10.1103/PHYSREVE.75.027105/FIGURES/3/MEDIUM.

[109] Raichle ME, MacLeod AM, Snyder AZ, Powers WJ, Gusnard DA, Shulman GL. A default mode of brain function. Proceedings of the National Academy of Sciences of the United States of America. 2001;98(2):676–682. doi:10.1073/PNAS.98.2.676,.

[110] Fox MD, Snyder AZ, Vincent JL, Corbetta M, Van Essen DC, Raichle ME. The human brain is intrinsically organized into dynamic, anticorrelated functional networks. Proceedings of the National Academy of Sciences of the United States of America. 2005;102(27):9673–9678. doi:10.1073/pnas.0504136102.

[111] Greicius M. Resting-state functional connectivity in neuropsychiatric disorders. Current Opinion in Neurology. 2008;21(4):424–430. doi:10.1097/WCO.0B013E328306F2C5,.

[112] Agosta F, Pievani M, Geroldi C, Copetti M, Frisoni GB, Filippi M. Resting state fMRI in Alzheimer's disease: Beyond the default mode network. Neurobiology of Aging. 2012;33(8):1564–1578. doi:10.1016/j.neurobiolaging.2011.06.007.

[113] Cole MW, Bassett DS, Power JD, Braver TS, Petersen SE. Intrinsic and task-evoked network architectures of the human brain. Neuron. 2014;83(1):238–251. doi:10.1016/j.neuron.2014.05.014.

[114] Gordon BA, Zacks JM, Blazey T, Benzinger TLS, Morris JC, Fagan AM, et al. Task-evoked fMRI changes in attention networks are associated with preclinical Alzheimer's disease biomarkers. Neurobiology of Aging. 2015;36(5):1771–1779. doi:10.1016/J.NEUROBIOLAGING.2015.01.019.

[115] Liu Q, Ganzetti M, Wenderoth N, Mantini D. Detecting large-scale brain networks using EEG: Impact of electrode density, head modeling and source localization. Frontiers in Neuroinformatics. 2018;12:323347. doi:10.3389/FNINF.2018.00004/BIBTEX.

[116] Paitel ER, Otteman CBD, Polking MC, Licht HJ, Nielson KA. Functional and effective EEG connectivity patterns in Alzheimer's disease and mild cognitive impairment: a systematic review. Frontiers in Aging Neuroscience. 2025;17:1496235. doi:10.3389/FNAGI.2025.1496235/FULL.

[117] Markett S, Nothdurfter D, Focsa A, Reuter M, Jawinski P. Attention networks and the intrinsic network structure of the human brain. Human Brain Mapping. 2022;43(4):1431–1448. doi:10.1002/HBM.25734.

[118] Buchanan CR, Pernet CR, Gorgolewski KJ, Storkey AJ, Bastin ME. Test–retest reliability of structural brain networks from diffusion MRI. NeuroImage. 2014;86:231–243. doi:10.1016/J.NEUROIMAGE.2013.09.054.

[119] Lo CY, Wang PN, Chou KH, Wang J, He Y, Lin CP. Diffusion tensor tractography reveals abnormal topological organization in structural cortical networks in Alzheimer's disease. Journal of Neuroscience. 2010;30(50):16876–16885. doi:10.1523/JNEUROSCI.4136-10.2010,.

[120] van den Heuvel MP, Sporns O. Rich-club organization of the human connectome. Journal of Neuroscience. 2011;31(44):15775–15786. doi:10.1523/JNEUROSCI.3539-11.2011.

[121] Fischer FU, Wolf D, Scheurich A, Fellgiebel A. Altered whole-brain white matter networks in preclinical Alzheimer's disease. NeuroImage: Clinical. 2015;8:660–666. doi:10.1016/J.NICL.2015.06.007.

[122] Fortunato S. Community detection in graphs. Physics Reports. 2010;486(3-5):75–174. doi:10.1016/J.PHYSREP.2009.11.002.

[123] Onnela JP, Saramäki J, Kertész J, Kaski K. Intensity and coherence of motifs in weighted complex networks. Physical Review E - Statistical, Nonlinear, and Soft Matter Physics. 2005;71(6):065103. doi:10.1103/PhysRevE.71.065103.

[124] Halu A, Mondragón RJ, Panzarasa P, Bianconi G. Multiplex PageRank. PLOS ONE. 2013;8(10):e78293. doi:10.1371/JOURNAL.PONE.0078293.

[125] Stam CJ, De Haan W, Daffertshofer A, Jones BF, Manshanden I, Van Cappellen Van Walsum AM, et al. Graph theoretical analysis of magnetoencephalographic functional connectivity in Alzheimer's disease. Brain. 2009;132(1):213–224. doi:10.1093/brain/awn262.

[126] Hage P, Harary F. Eccentricity and centrality in networks. Social Networks. 1995;17(1):57–63. doi:10.1016/0378-8733(94)00248-9.

[127] Clauset A, Newman MEJ, Moore C. Finding community structure in very large networks. Physical Review E - Statistical Physics, Plasmas, Fluids, and Related Interdisciplinary Topics. 2004;70(6):6. doi:10.1103/PhysRevE.70.066111.

[128] Newman MEJ. Modularity and community structure in networks. Proceedings of the National Academy of Sciences. 2006;103(23):8577–8582. doi:10.1073/PNAS.0601602103.

[129] Blondel VD, Guillaume JL, Lambiotte R, Lefebvre E. Fast unfolding of communities in large networks. Journal of Statistical Mechanics: Theory and Experiment. 2008;2008(10). doi:10.1088/1742-5468/2008/10/P10008.

[130] Jeub LGS, Bazzi M, Jutla SI, Mucha PJ. A generalized Louvain method for community detection implemented in MATLAB; 2011. Available from: `https://github.com/GenLouvain/GenLouvain`.

[131] Bassett DS, Wymbs NF, Rombach MP, Porter MA, Mucha PJ, Grafton ST. Task-Based Core-Periphery Organization of Human Brain Dynamics. PLoS Computational Biology. 2013;9(9):1003171. doi:10.1371/journal.pcbi.1003171.

[132] Canal-Garcia A, Veréb D, Mijalkov M, Westman E, Volpe G, Pereira JB. Dynamic multilayer functional connectivity detects preclinical and clinical Alzheimer's disease. Cerebral Cortex. 2024;34(2). doi:10.1093/cercor/bhad542.

[133] Betzel RF, Fukushima M, He Y, Zuo XN, Sporns O. Dynamic fluctuations coincide with periods of high and low modularity in resting-state functional brain networks. NeuroImage. 2016;127(4):287–297. doi:10.1016/j.neuroimage.2015.12.001.

[134] Telesford QK, Lynall ME, Vettel J, Miller MB, Grafton ST, Bassett DS. Detection of functional brain network reconfiguration during task-driven cognitive states. NeuroImage. 2016;142(7):198–210. doi:10.1016/j.neuroimage.2016.05.078.

[135] Puxeddu MG, Faskowitz J, Betzel RF, Petti M, Astolfi L, Sporns O. The modular organization of brain cortical connectivity across the human lifespan. NeuroImage. 2020;218:116974. doi:10.1016/j.neuroimage.2020.116974.

[136] Good BH, De Montjoye YA, Clauset A. Performance of modularity maximization in practical contexts. Physical Review E - Statistical, Nonlinear, and Soft Matter Physics. 2010;81(4):046106. doi:10.1103/PhysRevE.81.046106.

[137] Bazzi M, Porter MA, Williams S, McDonald M, Fenn DJ, Howison SD. Community Detection in Temporal Multilayer Networks, with an Application to Correlation Networks. Multiscale Modeling & Simulation. 2016;14(1):1–41. doi:10.1137/15M1009615.

[138] Bassett DS, Porter MA, Wymbs NF, Grafton ST, Carlson JM, Mucha PJ. Robust detection of dynamic community structure in networks. Chaos. 2013;23(1). doi:10.1063/1.4790830/153214.

[139] Ashourvan A, Telesford QK, Verstynen T, Vettel JM, Bassett DS. Multi-scale detection of hierarchical community architecture in structural and functional brain networks. PLOS ONE. 2019;14(5):e0215520. doi:10.1371/JOURNAL.PONE.0215520.

[140] Hanteer O, Magnani M. Unspoken Assumptions in Multi-layer Modularity maximization. Scientific Reports. 2020;10(1):1–15. doi:10.1038/s41598-020-66956-0.

[141] Sporns O, Honey CJ. Small worlds inside big brains. Proceedings of the National Academy of Sciences of the United States of America. 2006;103(51):19219–19220. doi:10.1073/pnas.0609523103.

[142] Bassett DS, Bullmore ET. Human Brain Networks in Health and Disease. Current opinion in neurology. 2009;22(4):340. doi:10.1097/WCO.0B013E32832D93DD.

[143] Bassett DS, Bullmore ET. Small-World Brain Networks Revisited. The Neuroscientist. 2016;23(5):499. doi:10.1177/1073858416667720.

[144] Collin G, Sporns O, Mandl RCW, Van Den Heuvel MP. Structural and Functional Aspects Relating to Cost and Benefit of Rich Club Organization in the Human Cerebral Cortex. Cerebral Cortex. 2014;24(9):2258–2267. doi:10.1093/CERCOR/BHT064.

[145] Van Den Heuvel MP, Stam CJ, Kahn RS, Hulshoff Pol HE. Efficiency of Functional Brain Networks and Intellectual Performance. The Journal of Neuroscience. 2009;29(23):7619. doi:10.1523/JNEUROSCI.1443-09.2009.

[146] van den Heuvel MP, Sporns O. Network hubs in the human brain. Trends in Cognitive Sciences. 2013;17(12):683–696. doi:10.1016/j.tics.2013.09.012.

[147] Delbeuck X, Van Der Linden M, Collette F. Alzheimer's Disease as a Disconnection Syndrome? Neuropsychology Review. 2003;13(2):79–92. doi:10.1023/A:1023832305702.

[148] Supekar K, Menon V, Rubin D, Musen M, Greicius MD. Network Analysis of Intrinsic Functional Brain Connectivity in Alzheimer's Disease. PLOS Computational Biology. 2008;4(6):e1000100. doi:10.1371/JOURNAL.PCBI.1000100.

[149] Parra MA, Saarimäki H, Bastin ME, Londoño AC, Pettit L, Lopera F, et al. Memory binding and white matter integrity in familial Alzheimer's disease. Brain. 2015;138(5):1355–1369. doi:10.1093/BRAIN/AWV048.

[150] Kabbara A, Eid H, El Falou W, Khalil M, Wendling F, Hassan M. Reduced integration and improved segregation of functional brain networks in Alzheimer's disease. Journal of neural engineering. 2018;15(2). doi:10.1088/1741-2552/AAAA76.

[151] Brier MR, Thomas JB, Ances BM. Network Dysfunction in Alzheimer's Disease: Refining the Disconnection Hypothesis. Brain Connectivity. 2014;4(5):299. doi:10.1089/BRAIN.2014.0236.

[152] Berlot R, Metzler-Baddeley C, Ikram MA, Jones DK, O'Sullivan MJ. Global efficiency of structural networks mediates cognitive control in mild cognitive impairment. Frontiers in Aging Neuroscience. 2016;8(DEC):230764. doi:10.3389/fnagi.2016.00292.

[153] Hilgetag CC, Goulas A. Is the brain really a small-world network? Brain Structure and Function. 2016;221(4):2361–2366. doi:10.1007/s00429-015-1035-6.

[154] Vaiana M, Muldoon SF. Multilayer Brain Networks. Journal of Nonlinear Science. 2020;30(5):2147–2169. doi:10.1007/s00332-017-9436-8.

[155] Huang J, Zhu Q, Wang M, Zhou L, Zhang Z, Zhang D. Coherent Pattern in Multi-Layer Brain Networks: Application to Epilepsy Identification. IEEE Journal of Biomedical and Health Informatics. 2020;24(9):2609–2620. doi:10.1109/JBHI.2019.2962519.

[156] Battiston F, Nicosia V, Latora V. Structural measures for multiplex networks. Physical Review E - Statistical, Nonlinear, and Soft Matter Physics. 2014;89(3):032804. doi:10.1103/PhysRevE.89.032804.

[157] Mucha PJ, Richardson T, Macon K, Porter MA, Onnela JP. Community Structure in Time-Dependent, Multiscale, and Multiplex Networks. Science. 2010;328(5980):876–878. doi:10.1126/SCIENCE.1184819.

[158] Reichardt J, Bornholdt S. Statistical mechanics of community detection. Physical Review E. 2006;74(1):016110. doi:10.1103/PhysRevE.74.016110.

[159] Battiston F, Nicosia V, Chavez M, Latora V. Multilayer motif analysis of brain networks. Chaos: An Interdisciplinary Journal of Nonlinear Science. 2017;27(4):047404. doi:10.1063/1.4979282.

[160] Guillon J, Chavez M, Battiston F, Attal Y, La Corte V, Thiebaut de Schotten M, et al. Disrupted core-periphery structure of multimodal brain networks in Alzheimer's disease. Network Neuroscience. 2019;3(2):635–652. doi:10.1162/NETN_A_00087.

[161] De Domenico M, Sasai S, Arenas A. Mapping Multiplex Hubs in Human Functional Brain Networks. Frontiers in Neuroscience. 2016;10(JUL):326. doi:10.3389/FNINS.2016.00326.

[162] Yu M, Engels MMA, Hillebrand A, Van Straaten ECW, Gouw AA, Teunissen C, et al. Selective impairment of hippocampus and posterior hub areas in Alzheimer's disease: an MEG-based multiplex network study. Brain. 2017;140(5):1466–1485. doi:10.1093/BRAIN/AWX050.

[163] Guillon J, Attal Y, Colliot O, Corte VL, Dubois B, Schwartz D, et al. Loss of brain inter-frequency hubs in Alzheimer's disease. Scientific Reports 2017 7:1. 2017;7(1):1–13. doi:10.1038/s41598-017-07846-w.

[164] Weissman DH, Roberts KC, Visscher KM, Woldorff MG. The neural bases of momentary lapses in attention. Nature Neuroscience 2006 9:7. 2006;9(7):971–978. doi:10.1038/nn1727.

[165] Prado J, Weissman DH. Heightened interactions between a key default-mode region and a key task-positive region are linked to suboptimal current performance but to enhanced future performance. NeuroImage. 2011;56(4):2276–2282. doi:10.1016/J.NEUROIMAGE.2011.03.048.

[166] Persson J, Lustig C, Nelson JK, Reuter-Lorenz PA. Age Differences in Deactivation: A Link to Cognitive Control? Journal of Cognitive Neuroscience. 2007;19(6):1021–1032. doi:10.1162/JOCN.2007.19.6.1021.

[167] Li W, Wang M, Zhu W, Qin Y, Huang Y, Chen X. Simulating the evolution of functional brain networks in Alzheimer's disease: Exploring disease dynamics from the perspective of global activity. Scientific Reports. 2016;6(1):1–11. doi:10.1038/srep34156.

[168] Tu JC, Millar PR, Strain JF, Eck A, Adeyemo B, Snyder AZ, et al. Increasing hub disruption parallels dementia severity in autosomal dominant Alzheimer's disease. Network Neuroscience. 2024;8(4):1265–1290. doi:10.1162/NETN_A_00395.

[169] He Y, Chen Z, Evans A. Structural insights into aberrant topological patterns of large-scale cortical networks in Alzheimer's disease. Journal of Neuroscience. 2008;28(18):4756–4766. doi:10.1523/JNEUROSCI.0141-08.2008.

[170] Zhang B, Xu Y, Zhu B, Kantarci K. The Role of Diffusion Tensor Imaging in Detecting Microstructural Changes in Prodromal Alzheimer's Disease. CNS Neuroscience & Therapeutics. 2014;20(1):3–9. doi:10.1111/CNS.12166.

[171] Buldú JM, Porter MA. Frequency-based brain networks: From a multiplex framework to a full multilayer description. Network Neuroscience. 2018;2(4):418–441. doi:10.1162/netn_a_00033.

[172] Desikan RS, Ségonne F, Fischl B, Quinn BT, Dickerson BC, Blacker D, et al. An automated labeling system for subdividing the human cerebral cortex on MRI scans into gyral based regions of interest. NeuroImage. 2006;31(3):968–980. doi:10.1016/J.NEUROIMAGE.2006.01.021.

[173] Fischl B, Van Der Kouwe A, Destrieux C, Halgren E, Ségonne F, Salat DH, et al. Automatically Parcellating the Human Cerebral Cortex. Cerebral Cortex. 2004;14(1):11–22. doi:10.1093/cercor/bhg087.

[174] Morcom AM, Bullmore ET, Huppert FA, Lennox B, Praseedom A, Linnington H, et al. Memory Encoding and Dopamine in the Aging Brain: A Psychopharmacological Neuroimaging Study. Cerebral Cortex. 2010;20(3):743–757. doi:10.1093/CERCOR/BHP139.

[175] Ashburner J. A fast diffeomorphic image registration algorithm. NeuroImage. 2007;38(1):95–113. doi:10.1016/J.NEUROIMAGE.2007.07.007.

[176] Ashburner J, Friston KJ. Computing average shaped tissue probability templates. NeuroImage. 2009;45(2):333–341. doi:10.1016/J.NEUROIMAGE.2008.12.008.

[177] Smith AM, Lewis BK, Ruttimann UE, Ye FQ, Sinnwell TM, Yang Y, et al. Investigation of low frequency drift in fMRI signal. NeuroImage. 1999;9(5):526–533. doi:10.1006/NIMG.1999.0435.

[178] de Winter JCF, Gosling SD, Potter J. Comparing the pearson and spearman correlation coefficients across distributions and sample sizes: A tutorial using simulations and empirical data. Psychological Methods. 2016;21(3):273–290. doi:10.1037/MET0000079.

[179] Bishara AJ, Hittner JB. Testing the significance of a correlation with nonnormal data: Comparison of Pearson, Spearman, transformation, and resampling approaches. Psychological Methods. 2012;17(3):399–417. doi:10.1037/A0028087.

[180] Korponay C, Janes AC, Frederick BB. Brain-wide functional connectivity artifactually inflates throughout functional magnetic resonance imaging scans. Nature Human Behaviour. 2024;8(8):1568–1580. doi:10.1038/s41562-024-01908-6.

[181] Arenas A, Duch J, Fernández A, Gómez S. Size reduction of complex networks preserving modularity. New Journal of Physics. 2007;9(6):176. doi:10.1088/1367-2630/9/6/176.

[182] Lancichinetti A, Fortunato S. Consensus clustering in complex networks. Scientific Reports. 2012;2(1):1–7. doi:10.1038/srep00336.

[183] Abbe E. Community Detection and Stochastic Block Models: Recent Developments. Journal of Machine Learning Research. 2018;18(177):1–86.

[184] Xu KS. MATLAB toolbox for fitting discrete-time dynamic stochastic block models; 2018. Available from: `https://github.com/IdeasLabUT/Dynamic-Stochastic-Block-Model`.

[185] Good P. Permutation Tests: A Practical Guide to Resampling Methods for Testing Hypotheses. Springer Science and Business Media; 2013.

[186] Krol LR. Permutation Test; 2024. Available from: https://github.com/lrkrol/permutationTest.

[187] Goulet-Pelletier JC, Cousineau D. A review of effect sizes and their condence intervals, Part I: The Cohen's d family. The Quantitative Methods for Psychology. 2018;14(4):242–265. doi:10.20982/tqmp.14.4.p242.

[188] Zweig MH, Campbell G. Receiver-operating characteristic (ROC) plots: a fundamental evaluation tool in clinical medicine. Clinical Chemistry. 1993;39(4):561–577. doi:10.1093/CLINCHEM/39.4.561.

[189] Martínez-Cagigal V. Multiple Testing Toolbox, MATLAB Central File Exchange; 2025. Available from: https://uk.mathworks.com/matlabcentral/fileexchange/70604-multiple-testing-toolbox.

[190] Xia M, Wang J, He Y. BrainNet Viewer: A Network Visualization Tool for Human Brain Connectomics. PLoS ONE. 2013;8(7):68910. doi:10.1371/JOURNAL.PONE.0068910.

[191] Benjamini Y, Hochberg Y. Controlling the False Discovery Rate: A Practical and Powerful Approach to Multiple Testing. Journal of the Royal Statistical Society: Series B (Methodological). 1995;57(1):289–300. doi:10.1111/J.2517-6161.1995.TB02031.X.

[192] García-Pérez MA. Use and misuse of corrections for multiple testing. Methods in Psychology. 2023;8:100120. doi:10.1016/J.METIP.2023.100120.

[193] Benjamini Y, Yekutieli D. The Control of the False Discovery Rate in Multiple Testing under Dependency. The Annals of Statistics. 2001;29(4):1165–1188.

[194] Slinger G, Stevelink R, van Diessen E, Braun KPJ, Otte WM. The importance of discriminative power rather than significance when evaluating potential clinical biomarkers in epilepsy research. Epileptic Disorders. 2023;25(3):285–296. doi:10.1002/epd2.20010.

[195] Bechtold B. Violin Plots for Matlab, Github Project; 2016. Available from: https://github.com/bastibe/Violinplot-Matlab.

[196] Parra MA, Pattan V, Wong D, Beaglehole A, Lonie J, Wan HI, et al. Medial temporal lobe function during emotional memory in early Alzheimer's disease, mild cognitive impairment and healthy ageing: an fMRI study. BMC Psychiatry. 2013;13:76. doi:10.1186/1471-244X-13-76.

[197] Du AT, Schuff N, Amend D, Laakso MP, Hsu YY, Jagust WJ, et al. Magnetic resonance imaging of the entorhinal cortex and hippocampus in mild cognitive impairment and Alzheimer's disease. Journal of Neurology, Neurosurgery & Psychiatry. 2001;71(4):441–447. doi:10.1136/jnnp.71.4.441.

[198] Igarashi KM. Entorhinal cortex dysfunction in Alzheimer's disease. Trends in Neurosciences. 2023;46(2):124–136. doi:10.1016/j.tins.2022.11.006.

[199] Braak H, Braak E. Evolution of neuronal changes in the course of Alzheimer's disease. Journal of Neural Transmission, Supplementa. 1998;53:127–140. doi:10.1007/978-3-7091-6467-9_11.

[200] Vogel JW, Young AL, Oxtoby NP, Smith R, Ossenkoppele R, Strandberg OT, et al. Four distinct trajectories of tau deposition identified in Alzheimer's disease. Nature Medicine. 2021;27(5):871–881. doi:10.1038/s41591-021-01309-6.

[201] St-Onge F, Chapleau M, Breitner JCS, Villeneuve S, Binette AP. Tau accumulation and its spatial progression across the Alzheimer's disease spectrum. medRxiv. 2024;6(1). doi:10.1101/2023.06.02.23290880.

[202] Xiong Y, Ye C, Chen Y, Zhong X, Chen H, Sun R, et al. Altered Functional Connectivity of Basal Ganglia in Mild Cognitive Impairment and Alzheimer's Disease. Brain Sciences. 2022;12(11):1555. doi:10.3390/brainsci12111555.

[203] Lopera F, Ardilla A, Martínez A, Madrigal L, Arango-Viana JC, Lemere CA, et al. Clinical features of early-onset Alzheimer disease in a large kindred with an E280A presenilin-1 mutation. JAMA. 1997;277(10):793–799. doi:10.1001/JAMA.277.10.793.

[204] Lorenz DM, Jeng A, Deem MW. The emergence of modularity in biological systems. Physics of Life Reviews. 2011;8(2):129–160. doi:10.1016/J.PLREV.2011.02.003.

[205] Nadini M, Sun K, Ubaldi E, Starnini M, Rizzo A, Perra N. Epidemic spreading in modular time-varying networks. Scientific Reports. 2018;8(1):1–11. doi:10.1038/s41598-018-20908-x.

[206] Nardelli PHJ, Rubido N, Wang C, Baptista MS, Pomalaza-Raez C, Cardieri P, et al. Models for the modern power grid. The European Physical Journal Special Topics 2014 223:12. 2014;223(12):2423–2437. doi:10.1140/EPJST/E2014-02219-6.

[207] Nowinski WL. Evolution of Human Brain Atlases in Terms of Content, Applications, Functionality, and Availability. Neuroinformatics. 2021;19(1):1–22. doi:10.1007/s12021-020-09481-9.

[208] Smith SM, Jenkinson M, Woolrich MW, Beckmann CF, Behrens TEJ, Johansen-Berg H, et al. Advances in functional and structural MR image analysis and implementation as FSL. NeuroImage. 2004;23(SUPPL. 1):S208–S219. doi:10.1016/J.NEUROIMAGE.2004.07.051.

[209] Woolrich MW, Jbabdi S, Patenaude B, Chappell M, Makni S, Behrens T, et al. Bayesian analysis of neuroimaging data in FSL. NeuroImage. 2009;45(1 Suppl). doi:10.1016/j.neuroimage.2008.10.055.

[210] Tzourio-Mazoyer N, Landeau B, Papathanassiou D, Crivello F, Etard O, Delcroix N, et al. Automated Anatomical Labeling of Activations in SPM Using a Macroscopic Anatomical Parcellation of the MNI MRI Single-Subject Brain. NeuroImage. 2002;15(1):273–289. doi:10.1006/NIMG.2001.0978.

[211] Schaefer A, Kong R, Gordon EM, Laumann TO, Zuo XN, Holmes AJ, et al. Local-Global Parcellation of the Human Cerebral Cortex from Intrinsic Functional Connectivity MRI. Cerebral Cortex (New York, NY). 2017;28(9):3095. doi:10.1093/CERCOR/BHX179.

[212] Hallquist MN, Hillary FG. Graph theory approaches to functional network organization in brain disorders: A critique for a brave new small-world. Network Neuroscience. 2018;3(1):1. doi:10.1162/NETN_A_00054.

[213] Makarov VV, Zhuravlev MO, Runnova AE, Protasov P, Maksimenko VA, Frolov NS, et al. Betweenness centrality in multiplex brain network during mental task evaluation. Physical Review E. 2018;98(6):062413. doi:10.1103/PhysRevE.98.062413.

[214] Chai LR, Mattar MG, Blank IA, Fedorenko E, Bassett DS. Functional Network Dynamics of the Language System. Cerebral Cortex. 2016;26(11):4148–4159. doi:10.1093/CERCOR/BHW238.

[215] Cai L, Wei X, Liu J, Zhu L, Wang J, Deng B, et al. Functional Integration and Segregation in Multiplex Brain Networks for Alzheimer's Disease. Frontiers in Neuroscience. 2020;14:478863. doi:10.3389/FNINS.2020.00051/BIBTEX.

[216] Holme P, Saramäki J. Temporal networks. Physics Reports. 2012;519(3):97–125. doi:10.1016/J.PHYSREP.2012.03.001.

[217] Madl J, Janka R, Bay S, Rohleder N. MRI as a Stressor: The Psychological and Physiological Response of Patients to MRI, Influencing Factors, and Consequences. Journal of the American College of Radiology. 2022;19(3):423–432. doi:10.1016/J.JACR.2021.11.020.

[218] Xu KS. Stochastic Block Transition Models for Dynamic Networks; 2015. Available from: `https://proceedings.mlr.press/v38/xu15.html`.

[219] Ishiguro K, Iwata T, Ueda N, Tenenbaum J. Dynamic Infinite Relational Model for Time-varying Relational Data Analysis. Advances in Neural Information Processing Systems. 2010;23.

[220] Benayoun M, Kohrman M, Cowan J, Van Drongelen W. EEG, temporal correlations, and avalanches. Journal of Clinical Neurophysiology. 2010;27(6):458–464. doi:10.1097/WNP.0B013E3181FDF8E5,.

[221] Olszowy W, Aston J, Rua C, Williams GB. Accurate autocorrelation modeling substantially improves fMRI reliability. Nature Communications. 2019;10(1):1220. doi:10.1038/S41467-019-09230-W.

[222] Cai L, Wang J, Guo Y, Lu M, Dong Y, Wei X. Altered inter-frequency dynamics of brain networks in disorder of consciousness. Journal of Neural Engineering. 2020;17(3):036006. doi:10.1088/1741-2552/AB8B2C.

[223] Schober P, Schwarte LA. Correlation coefficients: Appropriate use and interpretation. Anesthesia and Analgesia. 2018;126(5):1763–1768. doi:10.1213/ANE.0000000000002864.

[224] Nolan H, Whelan R, Reilly RB. FASTER: Fully Automated Statistical Thresholding for EEG artifact Rejection. Journal of Neuroscience Methods. 2010;192(1):152–162. doi:10.1016/J.JNEUMETH.2010.07.015.

[225] Jatoi MA, Kamel N, Malik AS, Faye I. EEG based brain source localization comparison of sLORETA and eLORETA. Australasian Physical and Engineering Sciences in Medicine. 2014;37(4):713–721. doi:10.1007/s13246-014-0308-3.

[226] Domingo Pascual-Marqui R. Review of Methods for Solving the EEG Inverse Problem. International Journal of Bioelectromagnetism. 1999;1(1):75–86.

[227] Pascual-Marqui RD, Esslen M, Kochi K, Lehmann D. Functional imaging with low resolution brain electromagnetic tomography (LORETA): a review. Methods and findings in experimental and clinical pharmacology. 2002;24:91–95.

[228] Bennys K, Rondouin G, Vergnes C, Touchon J. Diagnostic value of quantitative EEG in Alzheimer's disease. Neurophysiologie Clinique. 2001;31(3):153–160. doi:10.1016/S0987-7053(01)00254-4.

[229] Moretti DV, Babiloni C, Binetti G, Cassetta E, Dal Forno G, Ferreric F, et al. Individual analysis of EEG frequency and band power in mild Alzheimer's disease. Clinical Neurophysiology. 2004;115(2):299–308. doi:10.1016/S1388-2457(03)00345-6.

[230] Malek N, Baker MR, Mann C, Greene J. Electroencephalographic markers in dementia. Acta Neurologica Scandinavica. 2017;135(4):388–393. doi:10.1111/ane.12638.

[231] Talwar P, Kushwaha S, Chaturvedi M, Mahajan V. Systematic Review of Different Neuroimaging Correlates in Mild Cognitive Impairment and Alzheimer's Disease. Clinical Neuroradiology. 2021;31(4):953–967. doi:10.1007/s00062-021-01057-7.

[232] Haussmann R, Werner A, Gruschwitz A, Osterrath A, Lange J, Donix KL, et al. Precuneus Structure Changes in Amnestic Mild Cognitive Impairment. American Journal of Alzheimer's Disease and other Dementias. 2017;32(1):22–26. doi:10.1177/1533317516678087.

[233] Moretti DV. Theta and alpha eeg frequency interplay in subjects with mild cognitive impairment: Evidence from EEG, MRI and spect brain modifications. Frontiers in Aging Neuroscience. 2015;7(FEB):104963. doi:10.3389/FNAGI.2015.00031/REFERENCE.

[234] Bradfield LA, Hart G, Balleine BW. The role of the anterior, mediodorsal, and parafascicular thalamus in instrumental conditioning. Frontiers in Systems Neuroscience. 2013;7(OCT):54346. doi:10.3389/FNSYS.2013.00051/BIBTEX.

[235] Alcaraz F, Naneix F, Desfosses E, Marchand AR, Wolff M, Coutureau E. Dissociable effects of anterior and mediodorsal thalamic lesions on spatial goal-directed behavior. Brain Structure and Function. 2016;221(1):79–89. doi:10.1007/s00429-014-0893-7.

[236] Cholvin T, Loureiro M, Cassel R, Cosquer B, Geiger K, De Sa Nogueira D, et al. The Ventral Midline Thalamus Contributes to Strategy Shifting in a Memory Task Requiring Both Prefrontal Cortical and Hippocampal Functions. Journal of Neuroscience. 2013;33(20):8772–8783. doi:10.1523/JNEUROSCI.0771-13.2013.

[237] Mitchell AS, Dalrymple-Alford JC, Christie MA. Spatial Working Memory and the Brainstem Cholinergic Innervation to the Anterior Thalamus. Journal of Neuroscience. 2002;22(5):1922–1928. doi:10.1523/JNEUROSCI.22-05-01922.2002.

[238] Cai S, Huang L, Zou J, Jing L, Zhai B, Ji G, et al. Changes in Thalamic Connectivity in the Early and Late Stages of Amnestic Mild Cognitive Impairment: A Resting-State Functional Magnetic Resonance Study from ADNI. PLOS ONE. 2015;10(2):e0115573. doi:10.1371/JOURNAL.PONE.0115573.

[239] Zhou B, Liu Y, Zhang Z, An N, Yao H, Wang P, et al. Impaired Functional Connectivity of the Thalamus in Alzheimer’ s Disease and Mild Cognitive Impairment: A Resting-State fMRI Study. Current Alzheimer Research. 2013;10(7):754–766. doi:10.2174/15672050113109990146.

[240] Wang Z, Jia X, Liang P, Qi Z, Yang Y, Zhou W, et al. Changes in thalamus connectivity in mild cognitive impairment: Evidence from resting state fMRI. European Journal of Radiology. 2012;81(2):277–285. doi:10.1016/J.EJRAD.2010.12.044.

[241] Van De Mortel, Laurens Ansem, Thomas RM, Van Wingen, Guido Alexander. Grey Matter Loss at Different Stages of Cognitive Decline: A Role for the Thalamus in Developing Alzheimer's Disease. Journal of Alzheimer's Disease. 2021;83(2):705–720. doi:10.3233/JAD-210173.

[242] Zhao Q, Lu H, Metmer H, Li WXY, Lu J. Evaluating functional connectivity of executive control network and frontoparietal network in Alzheimer's disease. Brain Research. 2018;1678:262–272. doi:10.1016/J.BRAINRES.2017.10.025.

[243] Varangis E, Liu J, Miao Y, Zhu X, Stern Y, Lee S. Neural flexibility is higher in Alzheimer's disease and predicts Alzheimer's disease transition. Journal of Alzheimer's Disease. 2025;107(1). doi:10.1177/13872877251360025.

[244] Michels L, Riese F, Meyer R, Kälin AM, Leh SE, Unschuld PG, et al. EEG-fMRI Signal Coupling Is Modulated in Subjects With Mild Cognitive Impairment and Amyloid Deposition. Frontiers in Aging Neuroscience. 2021;13:631172. doi:10.3389/FNAGI.2021.631172/FULL.

[245] Barzegaran E, Knyazeva MG. Functional connectivity analysis in EEG source space: The choice of method. PLoS ONE. 2017;12(7):e0181105. doi:10.1371/JOURNAL.PONE.0181105.

[246] Halder T, Talwar S, Jaiswal AK, Banerjee A. Quantitative Evaluation in Estimating Sources Underlying Brain Oscillations Using Current Source Density Methods and Beamformer Approaches. eNeuro. 2019;6(4):0170–19. doi:10.1523/ENEURO.0170-19.2019.

[247] Pietto M, Parra MA, Trujillo N, Flores F, García AM, Bustin J, et al. Behavioral and Electrophysiological Correlates of Memory Binding Deficits in Patients at Different Risk Levels for Alzheimer's Disease. Journal of Alzheimer's disease : JAD. 2016;53(4):1325–1340. doi:10.3233/JAD-160056.

[248] Sheline YI, Raichle ME. Resting state functional connectivity in preclinical Alzheimer's disease. Biological Psychiatry. 2013;74(5):340–347. doi:10.1016/J.BIOPSYCH.2012.11.028.

[249] Wang Z, Moreno Y, Boccaletti S, Perc M. Vaccination and epidemics in networked populations—An introduction. Chaos, Solitons & Fractals. 2017;103(3):177–183. doi:10.1016/j.chaos.2017.06.004.

[250] Pastor-Satorras R, Castellano C, Van Mieghem P, Vespignani A. Epidemic processes in complex networks. Reviews of Modern Physics. 2015;87(3):925. doi:10.1103/RevModPhys.87.925.

[251] Shams B, Khansari M. Using network properties to evaluate targeted immunization algorithms. Network Biology. 2014;4(3):74–94.

[252] Cetinay H, Devriendt K, Van Mieghem P. Nodal vulnerability to targeted attacks in power grids. Applied Network Science. 2018;3(1). doi:10.1007/s41109-018-0089-9.

[253] Mancini M, De Reus MA, Serra L, Bozzali M, Van Den Heuvel MP, Cercignani M, et al. Network attack simulations in Alzheimer's disease: The link between network tolerance and neurodegeneration. Proceedings - International Symposium on Biomedical Imaging. 2016; p. 237–240. doi:10.1109/ISBI.2016.7493253.

[254] Dai Z, Yan C, Li K, Wang Z, Wang J, Cao M, et al. Identifying and Mapping Connectivity Patterns of Brain Network Hubs in Alzheimer's Disease. Cerebral Cortex. 2015;25(10):3723–3742. doi:10.1093/CERCOR/BHU246.

[255] Liu Y, Yu C, Zhang X, Liu J, Duan Y, Alexander-Bloch AF, et al. Impaired long distance functional connectivity and weighted network architecture in Alzheimer's disease. Cerebral Cortex. 2014;24:1422–1435. doi:10.1093/cercor/bhs410.

[256] Albert R, Barabási AL. Statistical mechanics of complex networks. Reviews of Modern Physics. 2002;74(1):47. doi:10.1103/RevModPhys.74.47.

[257] Casillo SM, Luy DD, Goldschmidt E. A History of the Lobes of the Brain. World Neurosurgery. 2020;134:353–360. doi:10.1016/J.WNEU.2019.10.155.

[258] Baker CM, Burks JD, Briggs RG, Milton CK, Conner AK, Glenn CA, et al. A Connectomic Atlas of the Human Cerebrum—Chapter 6: The Temporal Lobe. Operative Neurosurgery. 2018;15. doi:10.1093/ons/opy260.

[259] Squire LR, Stark CEL, Clark RE. The medial temporal lobe. Annual Review of Neuroscience. 2004;27:279–306. doi:10.1146/annurev.neuro.27.070203.144130.

[260] Xu Y, Chun MM. Dissociable neural mechanisms supporting visual short-term memory for objects. Nature. 2006;440(7080):91–95. doi:10.1038/NATURE04262;KWRD.

[261] Staresina BP, Davachi L. Object unitization and associative memory formation are supported by distinct brain regions. The Journal of neuroscience : the official journal of the Society for Neuroscience. 2010;30(29):9890–9897. doi:10.1523/JNEUROSCI.0826-10.2010.

[262] Song JH, Jiang Y. Visual working memory for simple and complex features: An fMRI study. NeuroImage. 2006;30(3):963–972. doi:10.1016/j.neuroimage.2005.10.006.

[263] Ritter P, Schirner M, Mcintosh AR, Jirsa VK. The Virtual Brain Integrates Computational Modeling and Multimodal Neuroimaging. Brain Connectivity. 2013;3(2):121–145. doi:10.1089/BRAIN.2012.0120.

[264] Monteverdi A, Palesi F, Schirner M, Argentino F, Merante M, Redolfi A, et al. Virtual brain simulations reveal network-specific parameters in neurodegenerative dementias. Frontiers in Aging Neuroscience. 2023;15:1204134. doi:10.3389/FNAGI.2023.1204134/BIBTEX.

[265] Zimmermann J, Perry A, Breakspear M, Schirner M, Sachdev P, Wen W, et al. Differentiation of Alzheimer's disease based on local and global parameters in personalized Virtual Brain models. NeuroImage: Clinical. 2018;19:240–251. doi:10.1016/J.NICL.2018.04.017.

[266] Zhu D, Zhang T, Jiang X, Hu X, Chen H, Yang N, et al. Fusing DTI and FMRI Data: A Survey of Methods and Applications. NeuroImage. 2013;102 Pt 1(P1):184. doi:10.1016/J.NEUROIMAGE.2013.09.071.

[267] Nentwich M, Ai L, Madsen J, Telesford QK, Haufe S, Milham MP, et al. Functional connectivity of EEG is subject-specific, associated with phenotype, and different from fMRI. NeuroImage. 2020;218:117001. doi:10.1016/J.NEUROIMAGE.2020.117001.

[268] Sales-Pardo M, Guimerà R, Moreira AA, Nunes Amaral LA. Extracting the hierarchical organization of complex systems. Proceedings of the National Academy of Sciences. 2007;104(39):15224–15229. doi:10.1073/PNAS.0703740104.

[269] Brown JA, Rudie JD, Bandrowski A, Van Horn JD, Bookheimer SY. The UCLA multimodal connectivity database: a web-based platform for brain connectivity matrix sharing and analysis. Frontiers in Neuroinformatics. 2012;0(NOV):28. doi:10.3389/FNINF.2012.00028.

[270] Zachary WW. An Information Flow Model for Conflict and Fission in Small Groups. Journal of Anthropological Research. 1977;33(4):452–473. doi:10.1086/JAR.33.4.3629752.

[271] Nooner KB, Colcombe SJ, Tobe RH, Mennes M, Benedict MM, Moreno AL, et al. The NKI-Rockland sample: A model for accelerating the pace of discovery science in psychiatry. Frontiers in Neuroscience. 2012;0(OCT):152. doi:10.3389/fnins.2012.00152.

[272] Mioshi E, Dawson K, Mitchell J, Arnold R, Hodges JR. The Addenbrooke's Cognitive Examination Revised (ACE-R): a brief cognitive test battery for dementia screening. International Journal of Geriatric Psychiatry. 2006;21(11):1078–1085. doi:10.1002/GPS.1610.

[273] Benedict RHB, Schretlen D, Groninger L, Brandt J. Hopkins Verbal Learning Test – Revised: Normative Data and Analysis of Inter-Form and Test-Retest Reliability. The Clinical Neuropsychologist. 1998;12(1):43–55. doi:10.1076/CLIN.12.1.43.1726.

[274] Borkowski JG, Benton AL, Spreen O. Word fluency and brain damage. Neuropsychologia. 1967;5(2):135–140. doi:10.1016/0028-3932(67)90015-2.

[275] Lafont S, Marin-Lamellet C, Paire-Ficout L, Thomas-Anterion C, Laurent B, Fabrigoule C. The Wechsler Digit Symbol Substitution Test as the Best Indicator of the Risk of Impaired Driving in Alzheimer Disease and Normal Aging. Dementia and Geriatric Cognitive Disorders. 2010;29(2):154–163. doi:10.1159/000264631.

[276] Rey A, Osterrieth PA. Rey-Osterrieth Complex Figure Copying Test. Psychological Assessment. 2011;doi:10.1037/T07717-000.

[277] Mckenna P, Warrington EK. Graded naming test: Manual. NFER-Nelson; 1983.

[278] Grober E, Buschke H, Korey SR. Genuine memory deficits in dementia. Developmental Neuropsychology. 1987;3(1):13–36. doi:10.1080/87565648709540361.

[279] Pearson N. Advanced clinical solutions for WAIS-IV and WMS-IV: Administration and scoring manual. San Antonio: The Psychological Corporation. 2009;7.

[280] Brown EC, Casey A, Fisch RI, Neuringer C. Trail Making Test as a screening device for the detection of brain damage. Journal of Consulting Psychology. 1958;22(6):469–474. doi:10.1037/H0039980.

[281] Yesavage JA, Sheikh JI. 9/Geriatric depression scale (GDS) recent evidence and development of a shorter version. Clinical gerontologist. 1986;5:165–173. doi:10.1300/J018v05n01_09.